

# Kent Academic Repository

## Full text document (pdf)

### Citation for published version

Rakibet, Osman Ozgur (2015) Epidermal and Body-Worn Antennas. Doctor of Philosophy (PhD) thesis, University of Kent,.

### DOI

### Link to record in KAR

<http://kar.kent.ac.uk/53682/>

### Document Version

UNSPECIFIED

#### Copyright & reuse

Content in the Kent Academic Repository is made available for research purposes. Unless otherwise stated all content is protected by copyright and in the absence of an open licence (eg Creative Commons), permissions for further reuse of content should be sought from the publisher, author or other copyright holder.

#### Versions of research

The version in the Kent Academic Repository may differ from the final published version.

Users are advised to check <http://kar.kent.ac.uk> for the status of the paper. **Users should always cite the published version of record.**

#### Enquiries

For any further enquiries regarding the licence status of this document, please contact:

[researchsupport@kent.ac.uk](mailto:researchsupport@kent.ac.uk)

If you believe this document infringes copyright then please contact the KAR admin team with the take-down information provided at <http://kar.kent.ac.uk/contact.html>

# Epidermal and Body-Worn Antennas

A Thesis Submitted to The University of  
Kent

For The Degree of Doctor of Philosophy  
In Electronic Engineering

By  
Osman Özgür Rakibet

December 2015

*Dedicated to my family & Gizem...*

# *Acknowledgements..*

I would like to express my special gratitude to my supervisor Prof. John C. Batchelor for his invaluable advice, support and for pushing me to achieve my best throughout my PhD at University of Kent.

I would like to thank Simon Jakes, Clive Birch and Tony Brazier for all their help on their help on making the RFID tags and good advice towards my measurements. My gratitude also goes to all the staff IT support and technical support to help me throughout my research.

I thank also to Relly Bowman, Nina Lozanska, Susan Lowry, Zoe Wood, all administrative staff and all the secretaries for helping me, formally or informally and in no time whenever I needed.

In addition to this, I would like to thank Prof Mohammed Sobhy for his invaluable help and advice on waveguide measurements, Dr. Ali Ziai for sharing his precious knowledge on RFID tag design and measurement. I would also like to thank my colleagues in the communication group and many more who helped me for my measurements especially, Dumtoo Oyeka, Badredin Turki, Liang Wu, Srijittra Swaisaenyakorn, Gurtac Yemiscioglu and Yusuf Insel. Thanks to those many more that helped out for my measurements, without you I would not have the invaluable data for my thesis.

I thank to my precious friends whom I met while living in Canterbury, and those whom I knew before coming to Canterbury, to those who were close to me and those who were far away from me.

I would also like to thank my parents: Huseyin and Aysen Rakibet, my sister Meryem Rakibet for being supportive, understanding, encouraging me throughout my study. Without your support and belief in me all of this would not have been achieved.

Last but not the least I thank to my fiancée, Gizem Utkan, for her help on my measurements, endless support, encouragement throughout my entire PhD period.

# *Abstract*

The work in this thesis focuses on flexible body-worn Electromagnetic Band-gap structures to remove body interference on the functionality of antennas and with compact UHF sensor tags designed for epidermal attachment and which are used in assisted living applications.

Two passive sensing designs based on UHF RFID technology are presented. The first tag is mounted on the hard palette of the mouth and detects tongue position, while the second is a skin-mounted strain gauge. Both designs are proposed for wheelchair or computer mouse control applications. Measurements show the sensors can communicate over short ranges comparable with the distance expected between a patient's mouth or face and a reader antenna. The mouth sensor is demonstrated to act as a tongue controlled switch, while the epidermal sensor is intended for eyebrow twitch control. Tests indicate both designs have a useful and repeatable sensing function, with more than 3 dB isolation in the switching case and approximately 0.25 dBm per percentage stretch in the strain gauge. Accurate arm and mouth models are used to simulate and validate the measurement results.

Secondly, an investigation of how the system users can be trained with an appropriate repetition scheme to use the tongue control system efficiently are considered. The training method has been tested on 3 users and the improvement on the efficiency of using the system is also presented.

Osman Özgür Rakibet

December 2015

# *Publications and Contributions*

1. O. O. Rakibet, J. C. Batchelor, C. V. Rumens and S. J. Holder, "Epidermal Passive RFID Strain Sensor for Assisted Technologies," *Antennas and Wireless Propagation Letters, IEEE* , vol.13, no., pp.814,817, 2014
2. O. O. Rakibet, J. C. Batchelor, R. Horne and S. W. Kelly "Passive Wireless Tags for Tongue Controlled Assistive Technology Interfaces" *IET Healthcare Technology Letters*, Accepted on December 2015
3. O. O. Rakibet and J. C. Batchelor, "Electromagnetic bandgap (EBG) structures with TiO<sub>2</sub> substrate," *Antennas and Propagation (APCAP), 2012 IEEE Asia-Pacific Conference on* , pp.199,200, 27-29 Aug. 2012
4. O. O. Rakibet, J. C. Batchelor and S. W. Kelly, "Passive stretchable RFID tag," *Antennas and Propagation Conference (LAPC), 2012 Loughborough*, pp.1,4, 12-13 Nov. 2012
5. O. O. Rakibet, J. C. Batchelor and S. W. Kelly, "RFID tags as passive enabling technology," *Antennas and Propagation Conference (LAPC), 2013 Loughborough*, pp.350,353, 11-12 Nov. 2013
6. O. O. Rakibet, D. O. Oyeka and J. C. Batchelor, "Passive RFID switches for assistive technologies," *Antennas and Propagation (EuCAP), 2013 7th European Conference on*, pp.1917,1920, 8-12 April 2013
7. J. C. Batchelor, O. O. Rakibet, C. V. Rumens and S. J. Holder, "Accurate RFID strain gauges for skin mounting," *Antennas and Propagation Society International Symposium (APSURSI), 2014 IEEE* , pp.836,837, 6-11 July 2014

8. C. V. Rumens, O. O. Rakibet, J. C. Batchelor and S. J. Holder "Polydimethylsiloxane Substrates for passive UHF RFID Sensors," Antennas and Propagation Conference (LAPC), 2014 Loughborough , 10-11 Nov. 2014



# CONTENTS

\* \* \*

<b>Acknowledgements</b>	<b>ii</b>
<b>Abstract</b>	<b>iv</b>
<b>Publications and Contributions</b>	<b>v</b>
<b>List of Figures</b>	<b>xii</b>
<b>List of Tables</b>	<b>xvii</b>
<b>1 Introduction</b>	<b>1</b>
1.1 Introduction . . . . .	2
1.1.1 Wireless Sensor Networks . . . . .	2
1.1.2 UHF RFID Technology . . . . .	4
1.1.2.1 RFID History . . . . .	6
1.1.3 UHF RFID Sensors . . . . .	7
1.2 Research Objectives and Contributions . . . . .	8

1.2.1	Objectives . . . . .	9
1.2.2	Contributions . . . . .	9
1.3	Thesis Outline . . . . .	10
<b>References</b>		<b>12</b>
<b>2</b>	<b>UHF RFID System Components and Communications</b>	<b>14</b>
2.1	Introduction . . . . .	15
2.2	Parameters of Antennas . . . . .	16
2.2.1	Radiation Pattern . . . . .	17
2.2.2	Directivity . . . . .	19
2.2.3	Gain and Radiation Efficiency . . . . .	20
2.2.4	EIRP . . . . .	21
2.2.5	Polarization . . . . .	21
2.2.6	RFID Tag Antenna Input Impedance . . . . .	22
2.2.7	Antenna Aperture and Effective Area . . . . .	23
2.2.8	Polarisation Mismatch . . . . .	25
2.2.9	Sensitivity of the Transponder . . . . .	26
2.2.10	Functional Impedance of the Transponder Chip . . . . .	26
2.2.11	Tag Antenna Scattering Aperture . . . . .	27
2.2.12	Tag Power Transmission . . . . .	30
2.2.13	Friis Transmission Formula . . . . .	32
2.2.14	Tag Read Range . . . . .	34
2.3	Conclusion and Summary . . . . .	35
<b>References</b>		<b>36</b>
<b>3</b>	<b>Methodology of UHF RFID Tag Sensor Design</b>	<b>38</b>
3.1	Introduction . . . . .	39
3.2	Tag Performance Assessment . . . . .	40
3.2.1	Transmitted Power . . . . .	40
3.2.2	Backscattered Power . . . . .	41

---

3.2.3	Read Range . . . . .	41
3.3	Sensing . . . . .	42
3.3.1	Turn-on power to activate the chip . . . . .	43
3.3.2	Power Transmission Coefficient . . . . .	45
3.4	UHF RFID Tag Antenna Design Process . . . . .	46
3.4.1	Environmental Constraints . . . . .	48
3.4.2	Impedance Matching Methods for RFID Tags . . . . .	48
3.4.2.1	T-Match . . . . .	48
3.4.2.2	Inductively Coupled Loop Match . . . . .	50
3.4.2.3	Nested Slot . . . . .	51
3.4.2.4	Meandering . . . . .	52
3.4.2.5	Slot Antenna Inductance and Dimensions . . . . .	53
3.4.3	Transponder Chip Types . . . . .	54
3.5	Simulation . . . . .	56
3.5.1	Simulating RFID tag sensors on body tissue . . . . .	58
3.5.2	Stretching Effect Simulations . . . . .	59
3.5.3	Simulation Optimisation . . . . .	59
3.5.3.1	Meshing . . . . .	60
3.6	Measurement Set Up . . . . .	61
3.7	Sensor Tag Prototyping and Optimisation . . . . .	62
3.8	Conclusions . . . . .	64
<b>References</b>		<b>65</b>
<b>4</b>	<b>Dielectric Measurements and Electromagnetic Band-Gap Structures</b>	<b>68</b>
4.1	Introduction . . . . .	69
4.2	EBG Structure Design . . . . .	71
4.3	Low Profile Antennas on EBG Structures . . . . .	73
4.4	Reflection Characterisation . . . . .	73
4.5	400 MHZ EBG Structure . . . . .	75
4.6	Dielectric Constant Measurement . . . . .	78

---

4.6.1	Waveguide Measurement Method . . . . .	80
4.7	Measurement Results . . . . .	83
4.8	Conclusions . . . . .	86
<b>References</b>		<b>88</b>
<b>5</b>	<b>Epidermal Passive RFID Strain Sensor for Assisted Technologies</b>	<b>90</b>
5.1	Introduction . . . . .	91
5.2	Strain Gauge RFID Tag . . . . .	93
5.2.1	Strain Gauge Sensor Concept . . . . .	94
5.2.1.1	Single Port Slot Stretchable Antenna Sensor . . . . .	94
5.2.1.2	Two Port Slot Stretchable Antenna Sensor . . . . .	95
5.2.1.3	Simulation Results . . . . .	99
5.2.2	Elastic PDMS Substrate Formation . . . . .	104
5.2.3	Strain RFID Sensor . . . . .	106
5.2.4	Results and Discussion . . . . .	112
5.3	Conclusion . . . . .	117
<b>References</b>		<b>119</b>
<b>6</b>	<b>Passive RFID Tongue Proximity Sensor</b>	<b>122</b>
6.1	Introduction . . . . .	123
6.2	In Mouth RFID Tag . . . . .	125
6.2.1	Initial In Mouth Tag Design . . . . .	126
6.2.1.1	In Mouth Tag Measurement Setup . . . . .	128
6.2.1.2	Results . . . . .	131
6.2.2	Modified In-Mouth Tag . . . . .	132
6.2.2.1	Results . . . . .	134
6.2.3	Final Conformal Tongue Touch RFID Tag . . . . .	135
6.2.4	Simple Mouth Model . . . . .	136
6.2.5	Accurate Mouth Model . . . . .	140
6.3	User Training Process . . . . .	147

6.4 Conclusion and Future Work . . . . .	160
<b>References</b>	<b>162</b>
<b>7 Summary, Key-Points and Future Work</b>	<b>164</b>

# LIST OF FIGURES

\* \* \*

1.1	Internet of things. . . . .	3
2.1	Conventional RFID System. . . . .	15
2.2	3D radiation pattern of a dipole antenna. . . . .	17
2.3	Far-field regions. . . . .	19
2.4	Polarisation of the antenna and the waves. . . . .	25
2.5	Tag antenna equivalent circuit. . . . .	27
2.6	Equivalent circuit of an RFID tag. . . . .	28
2.7	Geometrical orientation of transmitting and receiving antennas for Friis equation. . . . .	32
3.1	Example of measured read range against frequency for body mounted UHF tag. . . . .	42
3.2	Activation of tag by ramping the transmitted power. . . . .	44
3.3	RFID tag antenna design process flow chart. . . . .	47
3.4	T-Match. . . . .	49
3.5	Inductively coupled loop match. . . . .	51
3.6	The geometry of the nested-slot suspended-patch. . . . .	52

---

3.7	Meander line. . . . .	53
3.8	Strap NXP chip dimensions. . . . .	55
3.9	Higgs chip dimensions . . . . .	55
3.10	Arm phantom rectangular block. . . . .	58
3.11	Mouth model components. . . . .	58
3.12	Stretch effect. . . . .	60
3.13	Voyantic Lite RFID measurement system. . . . .	62
3.14	RFID sensor on various objects. . . . .	63
4.1	EBG structure. . . . .	71
4.2	Simulated unit cell EBG structure. . . . .	74
4.3	Reflection phase vs frequency plot of EBG structure. . . . .	75
4.4	EBG simulation structure. . . . .	77
4.5	Simulated $S_{11}$ parameters of a dipole on free space, on ground plane and on EBG. . . . .	78
4.6	Simulated EBG radiation patterns. . . . .	79
4.7	Waveguide measurements. . . . .	81
4.8	Cable positions. . . . .	84
4.9	Dielectric constant values of different materials at E-band. . . . .	85
5.1	Concept tag positions on the head. . . . .	92
5.2	Reader antenna concept for strain sensor tags. . . . .	92
5.3	Geometry of the one slot stretchable antenna. . . . .	95
5.4	$x$ -axis stretching effect on the structure. . . . .	96
5.5	$y$ -axis stretching effect on the structure. . . . .	96
5.6	Geometry of the two slot stretchable antenna. . . . .	97
5.7	$x$ -axis stretching effect on the two port structure. . . . .	97
5.8	$y$ -axis stretching effect on the two port structure. . . . .	98
5.9	Simultaneous $x$ and $y$ -axis stretching effect on the two port structure. . . . .	98
5.10	Single port slot structure simulation results. . . . .	99
5.11	Two port slot structure $x$ - axis stretch simulation results. . . . .	100

5.12	Two slots zero stretch $S_{11}$ and $S_{21}$ plots. . . . .	100
5.13	Two port slot structure $y$ - axis stretch simulation results. . . . .	101
5.14	Simultaneous two port $x$ and $y$ - axis stretch simulation results. . . . .	101
5.15	Two port slot structure phi calculation results. . . . .	103
5.16	Measured relative permittivity of Barium Titanate-PDMS composites (3GHz) in a waveguide. . . . .	105
5.17	Geometry of the RFID Strain Sensor. . . . .	107
5.18	CST simulation of stretchable PDMS strain sensor on arm. . . . .	108
5.19	Measured read range of a stretchable PDMS strain sensor mounted on an arm. . . . .	108
5.20	$S_{11}$ simulations of on arm stretchable PDMS strain sensor. . . . .	109
5.21	Deformation of conductive Lycra during laser cut. . . . .	109
5.22	PDMS structure. . . . .	111
5.23	Strain measurements on jig. . . . .	112
5.24	Measured transmitted power vs. frequency graph with $x$ -axis stretch. . . . .	114
5.25	Measured transmitted power to activate the chip vs stretch graph. . . . .	114
6.1	Reader antenna concept. . . . .	124
6.2	Homogeneous simple CST mouth model for UHF RFID tag simulations. . . . .	125
6.3	Mouth model components. . . . .	126
6.4	Geometry of the initial in mouth RFID tag on Mylar substrate. . . . .	127
6.5	Simulated surface current at 1000MHz of the initial tag on arm. . . . .	127
6.6	Measured read range of mouth tag on hard palate. . . . .	128
6.7	Simulated $S_{11}$ parameters on arm. . . . .	129
6.8	In mouth polystyrene blocks to separate tongue and tag. . . . .	129
6.9	Measurement Setup. . . . .	130
6.10	Applying dental adhesive to the RFID tag. . . . .	130
6.11	Measured read ranges with different tongue-tag separations by initial RFID tag. . . . .	131



6.12	Geometry of the modified in mouth RFID tag. . . . .	133
6.13	Simulated surface current of the modified tag. . . . .	133
6.14	Measured read ranges with different tongue-tag separations for the modified RFID. . . . .	135
6.15	Geometry of the conformal tongue touch RFID tag. . . . .	136
6.16	Homogeneous simple CST mouth model for UHF RFID tag sim- ulations. . . . .	137
6.17	Simulated performance parameters of mouth model with differ- ent tongue-tag separations. . . . .	139
6.18	Denture adhesive applied to attach the tag to the upper palate. .	140
6.19	Normalised measured backscattered power and simulated prod- uct of impedance match coefficient and tag gain as a function of tongue-tag separation. . . . .	141
6.20	Tag positions in simulated mouth. . . . .	142
6.21	Tag positions in simulated mouth and real mouth. . . . .	142
6.22	Simulated mouth model with different tongue-tag separations. .	143
6.23	Simulated S-Parameters using the accurate mouth model. . . . .	144
6.24	Simulated transmission coefficient vs backscattered measurement results. . . . .	145
6.25	Simulated mouth model with different tongue-tag separations. .	146
6.26	User posture in measurements. . . . .	147
6.27	User 1 Simulated $\tau \times G_{tag}$ product vs measured backscattered power. . . . .	147
6.28	User 2 Simulated $\tau \times G_{tag}$ product vs measured backscattered power. . . . .	148
6.29	User 3 Simulated $\tau \times G_{tag}$ product vs measured backscattered power. . . . .	148
6.30	Averaged Simulated $\tau \times G_{tag}$ product vs measured backscattered power. . . . .	149
6.31	Average error of specific target point for each measurement number.	151
6.32	Average of all measured errors on each measurement number. .	151

---

6.33 Read Range vs Target Read Range. . . . .	152
6.34 Error Magnitude comparison on user performances for 25 target hit performance. . . . .	154
6.35 Target accuracies for 3 users over a random sequence. . . . .	155

# LIST OF TABLES

\* \* \*

1.1	Regulations for passive UHF RFID systems. . . . .	5
3.1	Required transmitted power. . . . .	44
3.2	Power transmission coefficients. . . . .	46
4.1	Dimensions of the EBG components. . . . .	76
4.2	Permittivity and loss tangent values of different substrates. . . . .	86
5.1	Dimensions of single port stretchable slot antenna. . . . .	94
5.2	Strain RFID sensor dimensions. . . . .	107
5.3	Comparison of measured transmitted power achieved on week 0 and week 1. . . . .	115
5.4	Curve fitting to week 0 strain results. . . . .	115
5.5	Week 0 curve fitting to week 1 strain results. . . . .	116
6.1	Dimensions of the initial in mouth RFID tag. . . . .	127
6.2	Measured read ranges differences with different tongue - tag separations by the initial RFID tag at 1000MHz. . . . .	132
6.3	Dimensions of the modified in mouth RFID tag. . . . .	133

---

6.4	Measured read ranges differences with different tongue - tag separations for the modified RFID tag. . . . .	134
6.5	Dimensions of the conformal tongue touch RFID tag. . . . .	135
6.6	In-mouth measurement results. . . . .	140
6.7	Comparison of entire measurements to last 13 measurements. . .	156
6.8	Confusion matrices of 3 users and average hit rates for an ordered entire 7 sequence of targets. . . . .	157
6.9	Confusion matrices of 3 users and average hit rates for an ordered sequence of targets from 5 to 7. . . . .	158
6.10	Confusion matrices of 3 users and average hit rates of entire 25 random targets. . . . .	159
6.11	Confusion matrices of 3 users and average hit rates of random targets from 13 to 25. . . . .	160

# CHAPTER 1

## INTRODUCTION

\* \* \*

In this chapter a brief introduction to the history of Radio Frequency Identification (RFID), RFID sensors, the Internet of Things and the future trends in RFID sensor technology are presented. The thesis outlines and contributions are also presented. In the final section, the scope of this research and a brief introduction of the remaining chapters are provided.

## 1.1 Introduction

With the huge interest on the networked intelligent physical objects, various concepts which links the physical world with the virtual world have appeared [1–5]. Internet of Things (IoT) is currently the most popular paradigm, a futuristic vision in which the Internet embeds itself into everyday objects in a transparent and an unobtrusive manner [2]. As a result of this huge interest, sensing and computing capable objects have appeared by bringing the intelligence to the smart objects, allowing them to sense, interpret, and act on their environment, intercommunicate and change information with each other and with people. Therefore, the human becomes part of the feedback loop of a computational entity in which the computer and human are inextricably intertwined [1, 4]. Such predicted pervasive computing is personalized and accommodated to the needs of each individual, it recedes into the background of our daily life. This disappearance of the technology was already predicted in 1991 by Mark Weiser as a fundamental consequence of the seamless integration of computational intelligence into the world as shown in Figure 1.1 [6].

### 1.1.1 Wireless Sensor Networks

A sensor network is an infrastructure comprised of sensing (measuring), computing, and communication elements that gives an administrator the ability to instrument, observe, and react to events and phenomena in a specified environment. The administrator typically is a civil, governmental, commercial, or industrial entity.

Wireless Sensor Networks' (WSN) recent technological advances in low power integrated circuits and wireless communications have made available efficient, low cost, low power miniaturized devices for use in remote sensing applications. These factors allowed the diffusion of a large number of intelligent sensors,

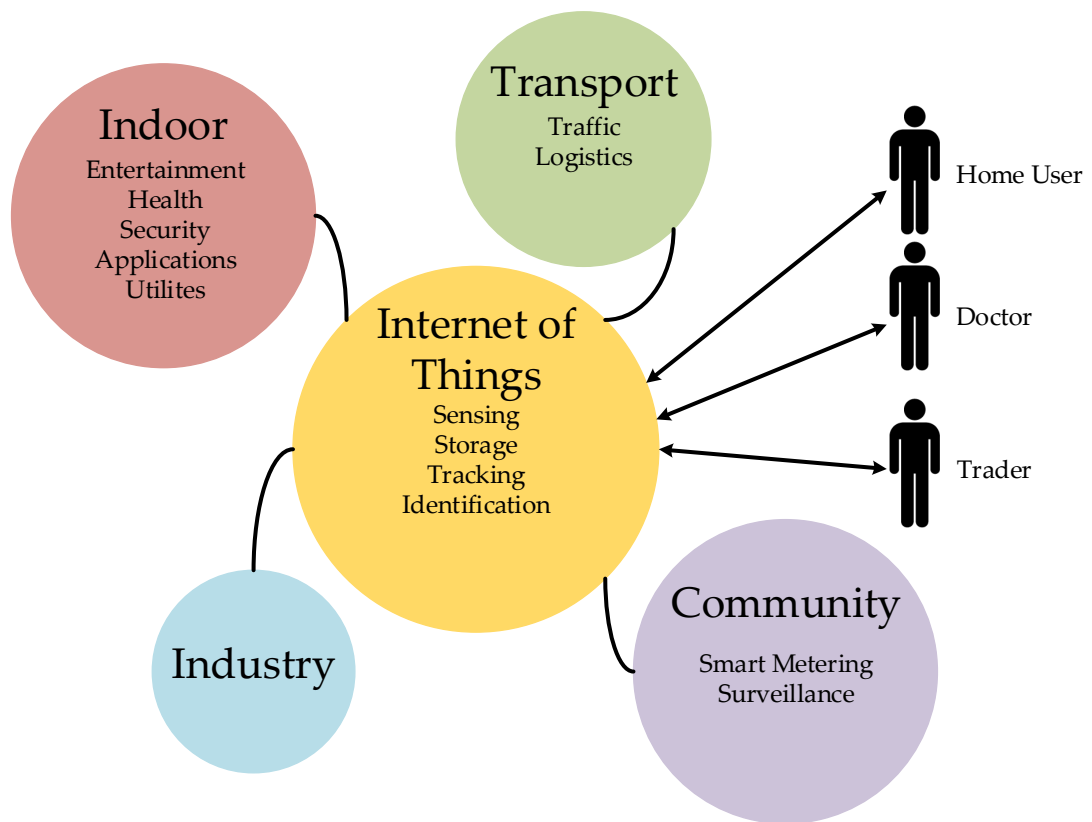


Figure 1.1: Internet of things.

enabling the collection, processing, analysis and dissemination of valuable information, gathered in a variety of environments. Autonomous sensors can potentially be deployed everywhere, though there are usually constraints on the power supply of such devices, so the communication technology must be carefully selected [7].

The environment can be the physical world or a biological system. Network sensor systems are seen by observers as an important technology that will experience major deployment in the next few years for a plethora of applications, not the least being national security. Typical applications include, but are not limited to, data collection, monitoring, surveillance, and medical telemetry. In addition to sensing, one is often also interested in control and activation.

## 1.1.2 UHF RFID Technology

Recent years have seen an explosion of interest in RFID. The reasons behind this interest can be listed as the availability of very low-cost passive RFID tags and functionality without battery. Additionally, the wider availability of robust internet infrastructures that can provide networked services to complement RFID and thus provide complete system functionality. These developments have allowed large-scale commercial applications in:

- supply chain
- ticketing
- asset tracking
- maintenance
- retail
- personal identification
- pharmaceuticals
- health-care
- banking
- transport industry
- homeland security
- sensing

As a result of an interest in these applications, RFID has become a popular wireless platform today. IDTechEx, a market research firm, estimates that more than 3.7 billion RFID tags have been deployed after 2007 with an accelerating



trend in the following years. This increase in the popularity of RFID technology, decreased the costs, and has revived interest in the use of RFID in pervasive computing research due to the unique opportunities it offers for low-cost large-scale experiments of novel systems and applications [8].

The telecommunication protocol used by the passive RFID systems is standardized under the ISO 18000-6 standard [9]. The tags are standardized under the EPC global UHF Class 1 Generation 2 standard [10].

The radio spectrum is divided into geographical sub-bands with regulated equivalent isotropically radiated power (EIRP) limits listed in Table 1.1. It is defined as the product of the accepted power by the transmitting antenna  $P_t$  and its maximum gain  $G_t$  within the regulated frequency band. This assures the maximum radiated power density for any transmitting antenna. The attainable read range from the passive UHF RFID tag is strongly dependent on the transmitted power used for the power supply to the tag transponder chip. Nonetheless, with the advances in low-power and low-voltage integrated CMOS technologies, the reading sensitivity of commercial tag transponder chips has dropped to tens of micro watts.

Table 1.1: Regulations for passive UHF RFID systems [10]

Region	Frequency Band (MHz)	EIRP (W)
Europe	865.6-867.6	3.28
United States	902-928	4
Japan	952-956.4	4
China	840.5-844.5, 920.5-924.5	3.28
Australia	920-926	4
	918-926	1

### 1.1.2.1 RFID History

A form of RFID was first implemented in World War II with German aeroplanes identifying themselves when they received indication that they were being illuminated by their radar, by rolling in order to change the backscattered signal. This was quickly followed by the United States and Britain using an active beacon on the plane to identify friendly aircraft in 1937-1938 [11] [11].

The RFID technology development accelerated by advances in radar theory during World War II. This is evident in one of the early works exploring RFID by Harry Stockman published in 1948.

RFID capability was further expanded in the 1950s following developments in radio and radar technology. In the 1960s, the electromagnetic theory related to RFID is studied [12].

At the same time, investment being made in companies developing RFID technology. Therefore, electronic article surveillance (EAS) system was invented after this interest of companies into the RFID technology. EAS was used to counter the theft of merchandise in the late 1960s. The momentum gained by development of EAS started off the expansion of RFID in the 1970s where developers, investors, companies, academic institutions and government laboratories actively worked on RFID with notable advances achieved, mainly in animal tracking, vehicle tracking, and factory automation.

One important development was the Los Alamos work that was presented by Alfred Koelle "Short- Range Radio-Telemetry for Electronic Identification Using Modulated Backscatter" [13]. This development signalled the beginning of practical, completely passive tags with an operational range of tens of metres.

Research on RFID transponder chip technology was also improved by using low voltage, low power CMOS logic circuit technology which resulted in size reduction and performance improvement. After that, individual programmable

tags on a large scale using EEPROM non-volatile memory was produced. However the full implementation of RFID technology did not began until the 1980s, the widespread use of personal computers allowed convenient and efficient collection and management of data from RFID systems with different countries showing interest in different applications.

During the 1990s new technological developments in Microelectronics expanded the functionality and there was wide scale deployment of RFID in other sectors such as deployment of the RFID in toll collections, railway cars, access control and many other varieties of applications.

The Auto-ID centre at Massachusetts Institute of Technology was formed in 1999, where it has been aimed to track and identify every object in a supply chain [11].

### **1.1.3 UHF RFID Sensors**

The main part of the thesis is committed to the detailed analysis of RFID passive sensors and sensing methods for body related variations and control device input creation by these sensors. Power related measurements which depend on the set up, environmental factors and tag antenna and RFID transponder chip impedance related measurements are proposed which with appropriate measurement methods can be related to the variation of the input impedance. Minimum turn on power which is described as the required minimum transmit power to activate the tag and the backscattered power collected by the reader can be listed as the power-related parameters.

It is stated by [14, 15], that the Analog Identifier (AID) which is a non-dimensional and set-up independent parameter and the phase of the backscattered signal whose variations are highly dependent on the change of antenna impedance and chip modulation [14, 15] are the impedance-related parameters.

The basic methodology for sensing methods which can be achieved by RFID sensor tags will then be described with the analysing methods along with the theoretical approach to observe the this phenomenon.

This thesis investigates RFID sensing opportunities to be used in assisted living applications through of a wide range of possible aspects, which combines wireless communication, electronics, sensors and electromagnetics. From the perspective of Internet of Things, passive communication in the UHF band, 860-960 MHz, is covered which provide enough read-ranges to implement a network of sensors for monitoring the required parameters.

## **1.2 Research Objectives and Contributions**

The main purpose of this research is to provide passive UHF RFID tag sensors to be used in assisted living technologies. Being a wireless and battery free communication system brings the advantages of passive communications to be used in body worn and epidermal applications. The effect of skin stretch on the epidermal applications in terms of geometrical alteration can be used to detect skin stretch amount. Also, the dielectric vicinity affect on the tag functionality as a result of detuning can be used to find the tongue proximity in the mouth when the tag is placed onto the hard palate in the mouth. Therefore, the possibility of deriving an input device as a mouse or to control a powered wheelchair by using these parameters is investigated in this project.

Additionally, in a separate study in order to minimize the close vicinity body effect on body worn antenna propagation, mushroom-like Electromagnetic Band-Gap (EBG) structures and size reduction methods are also investigated.

### 1.2.1 Objectives

The aims of this thesis are:

1. Use of EBG structures to eliminate body effect and size-reduction of EBG structures for a better fit to the body by using high dielectric constant substrates such as  $\text{TiO}_2$  powder to design flexible applications with a sufficient bandwidth.
2. Simulating stretchable epidermal antenna applications, using  $\text{BaTiO}_3$  loaded Polydimethylsiloxane (PDMS) as a flexible and stretchable substrate and attaching the stretchable conducting fabric as a conductor for flexible and stretchable UHF RFID tag sensors.
3. Simulating in mouth UHF RFID tag sensor attached to the hard palate with an accurate mouth model. The investigation of tag antenna parameters such as read range, backscattered power, transmitted power, tag gain and the transmission coefficient relationship with the tongue proximity. Additionally, the training of the users to use the sensor efficiently is also a point of interest.

### 1.2.2 Contributions

The contributions of this thesis are:

1. Investigation of potentially thin, elastic, flexible wearable EBG structures for on-body wireless applications based on  $\text{BaTiO}_3$  loaded Polydimethylsiloxane (PDMS) structures.
2. Creation of a passive wireless epidermal strain gauge sensor for application as a muscle twitch activated human-device interface.

3. Simulation and physical validation of the muscle twitch sensing tag.
4. Creation of a novel hard palette mounted passive tongue position sensor for application as a human-device interface.
5. Electromagnetic simulation and physical validation of the tongue-tag interaction and radio channel for the tag-tongue sensor.
6. Evaluation of a user training scheme to demonstrate how rapidly and accurately the tongue-tag sensor can be operated.

### 1.3 Thesis Outline

**Chapter 1** has introduced the history of RFID technology, UHF band RFID technology, UHF RFID sensors and the use of body-worn technologies in assisted living applications. Internet of Things in UHF RFID sensing have been highlighted and the motivation for including it in this research is elaborated.

In **Chapter 2** basic antenna parameters are listed and explained briefly with the physics and their effect on radiation propagation on passive UHF RFID systems. In the final section of the chapter Friis Equations are also presented in detail.

In **Chapter 3** the tag antenna design methodology, tag performance indicators, efficient design and optimisation of passive tags and measurement methods are presented. The derivation of external agent parameter for sensing which is derived by antenna impedance and RFID transponder chip impedance matching quality, tag impedance matching methods and simulation methods along with the body phantoms are also presented.

Use of EBG structures in eliminating harsh electromagnetic environments such as body effect, EBG structure design methodology, components of an EBG

structure, *LC* lumped element formation and the theoretical derived equations to highlight the individual effects on the performance are presented in **Chapter 4**. In addition to these, the effect of dielectric constant on the thickness reduction of EBG structures, waveguide method theory for dielectric constant measurement along with the system reliability tests by using different substrates, "TiO<sub>2</sub> effect on the EBG structures", EBG simulations with TiO<sub>2</sub> substrate are also presented.

**Chapter 5** introduces the epidermal strain gauge sensor tags for skin stretch detection. Stretchable slot antennas with a single and double ports are simulated along with the stretch effect to illustrate the geometric transformation on the circular shaped antenna structures due to stretch. Electrical properties and the effect of BaTiO<sub>3</sub> loading on the PDMS making are investigated. Designing, simulating and the performance assessment processes of the UHF RFID strain gauge sensor on PDMS substrate by using a controllable jig is presented in this chapter.

**Chapter 6** introduces the tongue controlled RFID tag sensors to be attached on the hard palate for tongue proximity detection in the mouth. The preliminary tag sensor design, alterations to increase the comfortable fit and the tag functionality along with the simple homogenous and accurate mouth models' simulations. The tag sensor performance assessment on three users, overall performance and the required training in efficient use of tag sensor are presented in this chapter.

**Chapter 7** concludes the key subjects of all the works presented in this thesis. It provides a list of useful conclusions for each chapter and specific RFID tag sensor applications allowing future researchers and designers of RFID sensor applications to appreciate how sensing for different antenna locations may influence overall performance. It also includes the range of relevant future work that would enhance the research.

## References

- [1] S. Mann, "Wearable computing: Toward Humanistic Intelligence," *Intelligent Systems, IEEE Transactions on*, vol. 16, no. 3, pp. 10–15, May 2001.
- [2] E. Welbourne, L. Battle, G. Cole, K. Gould, K. Rector, S. Raymer, M. Balazinska, and G. Borriello, "Building the internet of things using RFID: The RFID ecosystem experience," *Internet Computing, IEEE*, vol. 13, no. 3, pp. 48–55, May 2009.
- [3] G. Kortuem, F. Kawsar, D. Fitton, and V. Sundramoorthy, "Smart objects as building blocks for the Internet of things," *Internet Computing, IEEE*, vol. 14, no. 1, pp. 44–51, Jan 2010.
- [4] D. Sampaio, L. Reis, and R. Rodrigues, "A survey on ambient intelligence projects," in *Information Systems and Technologies (CISTI), 2012 7th Iberian Conference on*, June 2012, pp. 1–6.
- [5] D. Zhang, Z. Wang, B. Guo, and Z. Yu, "Social and community intelligence: Technologies and trends," *Software, IEEE*, vol. 29, no. 4, pp. 88–92, July 2012.
- [6] M. Weiser, "The computer for the 21st century," *Pervasive Computing, IEEE*, vol. 1, no. 1, pp. 19–25, Jan 2002.
- [7] P. Hall and Y. Hao, *Antennas and Propagation for Body-Centric Wireless Communications, Second Edition*. Artech House, 2012.
- [8] G. Roussos and V. Kostakos, "RFID in pervasive computing: State-of-the-art and outlook," *Pervasive and Mobile Computing*, vol. 5, no. 1, pp. 110 – 131, 2009.
- [9] "International organization for standardization, iso/iec 18000-6," 2015, Accessed: 24.03.2014. [Online]. Available: <http://www.iso.org/>



- 
- [10] "EPC global standards," Accessed: 15.01.2015. [Online]. Available: <http://www.gs1.org/gsm/kc/epcglobal>
- [11] B. Violino, "The history of RFID technology," *RFID Journal*, 2005. [Online]. Available: <http://www.rfidjournal.com/articles/view?1338>
- [12] R. F. Harrington, "Theory of loaded scatterers," *Electrical Engineers, Proceedings of the Institution of*, vol. 111, no. 4, pp. 617–623, April 1964.
- [13] A. R. Koelle, S. W. Depp, and R. Freyman, "Short-range radio-telemetry for electronic identification, using modulated RF backscatter," *Proceedings of the IEEE*, vol. 63, no. 8, pp. 1260–1261, Aug 1975.
- [14] C. Occhiuzzi, S. Caizzone, and G. Marrocco, "Passive UHF RFID antennas for sensing applications: Principles, methods, and classifications," *Antennas and Propagation Magazine, IEEE*, vol. 55, no. 6, pp. 14–34, Dec 2013.
- [15] G. Marrocco, "RFID grids: Part I; Electromagnetic theory," *Antennas and Propagation, IEEE Transactions on*, vol. 59, no. 3, pp. 1019–1026, March 2011.

# CHAPTER 2

## UHF RFID SYSTEM COMPONENTS AND COMMUNICATIONS

\* \* \*

This chapter addresses the fundamental antenna design requirements of general UHF RFID sensor tags for ambient monitoring, focusing on communication and sensing performance parameters. The operation of RFID tag antennas from the field point of view and the circuit point of view will be defined and discussed. Some of the antenna parameters which can be used to extract sensing information by the tag performance are also summarised.

## 2.1 Introduction

An RFID system is a wireless radio communication technology to detect and identify tagged objects or people. It usually consists of three main components: the tag or the transponder, a reader antenna and a host which is often a PC or a workstation that runs the database and other software. The tag consists of an antenna and a transponder chip which has a unique identification code. The readers are composed of an antenna connected to an RF electronic module which establishes the link between the tag and the host as shown in Figure 2.1 [1–3].

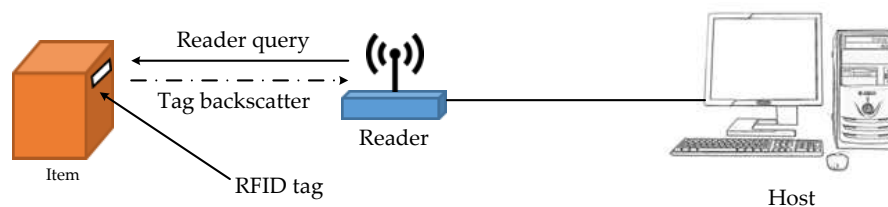


Figure 2.1: Conventional RFID System.

RFID tags are classified as active, passive and semi-active. Tags which contain an on-board power source are active tags where the power to transmit the data to the reader by the tag is generated by this source.

Semi-active tags contain a battery in order to operate the circuitry of the microchip but they also need to draw power from the magnetic field created by the reader in order to communicate with the reader via radio waves.

Passive RFID tags do not have an on-board power source, instead they use the power emitted from the reader to power up the transponder chip and transmit stored data in the chip back to the reader. Passive tags are long life and low cost which are their main advantages.

Different resonant antenna designs can be used for passive UHF tags such as dipole, folded dipole, meandered dipole, loop antenna, slot antenna and

patch antennas [4–8]. UHF RFID tags can be used for several purposes, such as tracking, identifying, anti-counterfeiting and sensing. After deciding the purpose of the tag, the tag antenna design is based on other factors such as the performance requirement and expected environmental factors.

Currently, most conventional RFID tag antennas are either constructed of etched or punched thin metal sheet or printed conducting ink on dielectric substrates.

## 2.2 Parameters of Antennas

Antennas are defined as structures which radiate or receive electromagnetic waves. This occurs by conversion of electrons energy to photons and vice versa. In other words it can be explained as a transition structure between free-space and a guiding device.

Regardless the type of the antenna, the basic principle is the same for all. Radiation is produced by accelerating or decelerating the charges and can be expressed [9, 10]:

$$\dot{I}L = Q\dot{v}[Ams^{-1}]. \quad (2.1)$$

where,  $\dot{I}$  is a time-changing current ( $As^{-1}$ ),  $L$  is the length of a current element (m),  $Q$  is the charge (C), and  $\dot{v}$  is the time change of velocity which equals the acceleration of the charge ( $m s^{-2}$ ).

In the following sections, relevant antenna parameters are outlined.

### 2.2.1 Radiation Pattern

The radiation pattern is defined as a mathematical function or a graphical representation of the radiation properties of the antenna as a function of the spherical coordinates,  $\theta$  and  $\phi$ . Field patterns can be presented in three-dimensional spherical coordinates or by separating the three-dimensional components by cutting through the main lobe axis to examine the azimuth and elevation axis individually.

As shown in Figure 2.2, the representation of the three-dimensional radiation pattern is presented including the directions of the E-field and H-field components.

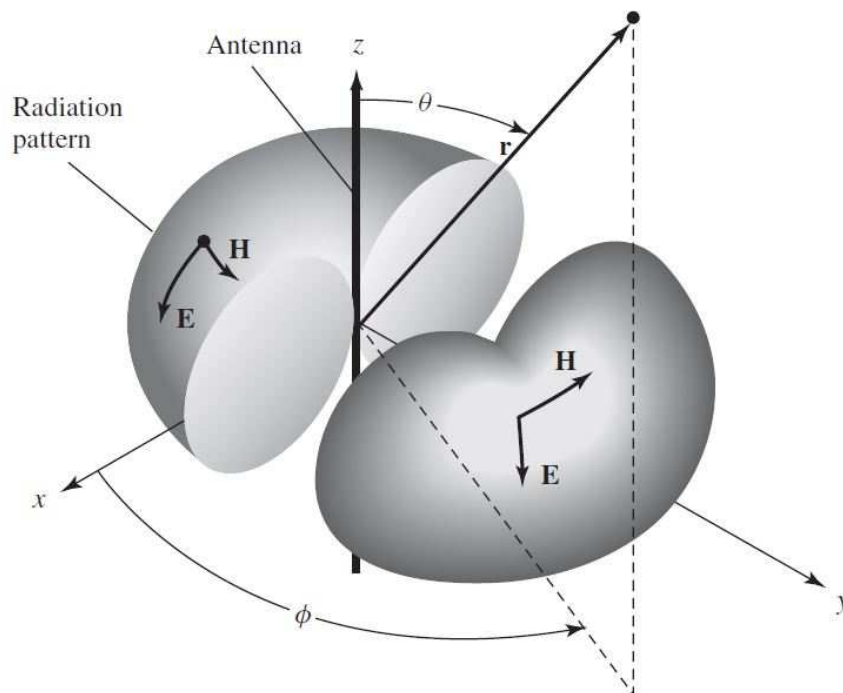


Figure 2.2: 3D radiation pattern of a dipole antenna [11].

The radiation pattern region can be divided into three sections; far-field, reactive near-field and radiating near field (Fresnel region). In the far-field region the shape of the waves does not change with the distance where the

radiated signals dominate with E-field and H-field orthogonal to each other and to the field direction of propagation, i.e. as plane waves. The far-field region's boundaries can be expressed as  $R > (2D)^2/\lambda$  where  $D$  is the maximum overall dimension of the antenna,  $\lambda$  is the operational wavelength and  $R$  is the distance from the antenna to the point of interest.  $R \gg D$  and  $R \gg \lambda$  conditions must be satisfied in this region as shown in Figure 2.3. By looking at these conditions, it can be concluded that the radiated power rays in a given direction from any part of the antenna are approximately parallel. Therefore, this ensures the fields in the far-field region behave like plane waves.

The radiating near-field occurs between near and far-fields where the radiating fields start to predominate over the reactive fields. The shape of the radiation may vary notably with distance in this range. The region boundaries can be expressed as:

$$0.62\sqrt{\frac{D^3}{\lambda}} < R < \frac{2D^2}{\lambda}. \quad (2.2)$$

The reactive near field is the region which is in the closest vicinity of the antenna. It is where reactive fields are dominant (there is a  $90^0$  phase shift between the E-field and the H-field). Additionally, for a very short dipole, or equivalent radiator, the outer boundary is commonly taken to exist at a distance  $\lambda/2\pi$  from the antenna surface [11, 12].

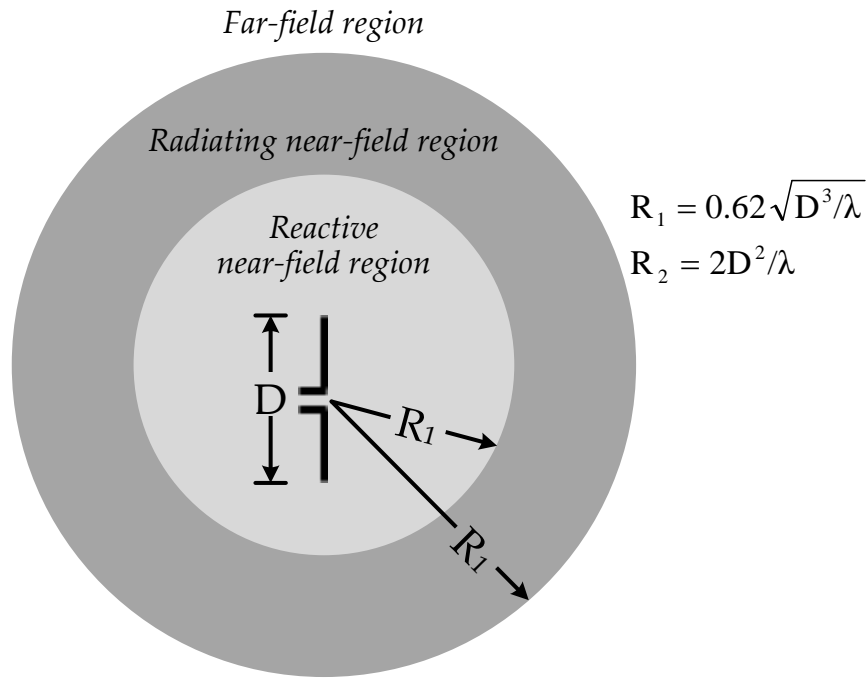


Figure 2.3: Far-field regions [11].

### 2.2.2 Directivity

Directivity is stated as the most important quantitative information for an antenna from the field point of view [13]. It is defined as a measure of the concentration of radiated power in a particular direction. Mathematically it can be shown as the ratio of radiation intensity in a given direction from the antenna to the radiation intensity averaged over all directions as shown below:

$$D = \frac{U(\theta, \phi)}{U(\theta, \phi)_{av}} = \frac{4\pi U(\theta, \phi)}{P_t} = \frac{4\pi U(\theta, \phi)}{\oint_{\Omega} U d\Omega}. \quad (2.3)$$

where  $P_t$  is the total radiated power (Watts) and  $U$  is the radiation intensity in W/unit solid angle. The relationship between directivity and the radiation intensity can be derived from the link to the averaged radiated power density  $S_{av}$  ( $W/m^2$ ) by distance square:

$$U = r^2 S_{av}. \quad (2.4)$$

### 2.2.3 Gain and Radiation Efficiency

Obtaining the total input power to an antenna is straightforward in practice while the total radiated power of an antenna is hard to measure. In order to simplify and get over this issue, the *gain* of the antenna is introduced. The gain is derived by the ratio of the radiation intensity in a given direction from the antenna to the total input power accepted by the antenna divided by  $4\pi$ . The direction of maximum radiation is implied unless the direction is not specified. The derived gain equation is:

$$G = \frac{4\pi U}{P_{in}}. \quad (2.5)$$

where  $U$  is again the radiation intensity in W/unit solid angle and  $P_{in}$  is the total input power accepted by the antenna in Watts. The input power and the accepted input power accepted by the antenna may differ in the case of a feed line mismatch. This can be related to the voltage reflection coefficient  $\Gamma$  at the antenna input and the transmission coefficient  $\tau$  where these parameters will be discussed later in the chapter. Therefore, for a  $\Gamma$  value tending to 0 the matching efficiency will approach 100%. In order to show the link between the gain and the directivity, Equations 2.3 and 2.5 are compared:

$$G = \frac{P_t}{P_{in}} D = \eta_e D. \quad (2.6)$$

where,  $\eta_e$  is the radiation efficiency factor of the antenna and the ratio of the radiated power to the input power accepted by the antenna. For an ideal, lossless antenna, the gain is equal to the directivity.



By this efficiency factor, the conductor loss and the dielectric loss are taken into account while the impedance mismatch between the feed line and the antenna is not [13].

#### 2.2.4 EIRP

Effective isotropic radiated power or EIRP is described as the amount of radiated power required by an isotropic antenna to produce the maximum power density in the direction of a given antenna beam. EIRP is expressed mathematically:

$$EIRP = P_t G. \quad (2.7)$$

where,  $P_t$  is the radiated power. The pathloss between the transmitting and receiving antennas can be easily achieved by the ratio between the transmitted to the received EIRP. Another closely related term is the effective radiated power, ERP, which is also widely used in the industry. The radiated power is calculated by using a half-wavelength dipole rather than an isotropic antenna as the reference, thus:

$$ERP(dBW) = EIRP(dBW) - 2.15dBi. \quad (2.8)$$

#### 2.2.5 Polarization

The polarization of an antenna is the indication of the polarization of its radiating wave. Polarization types are linear, circular and elliptical. The alignment of the radiating current in the antenna generates the polarization. For a linear polarization, the current should travel along one axis; for a circular polarization, two orthogonal currents with 90-degree phase offset should be created on the antenna. In practice, mixed polarizations may be found in many

antennas since an antenna has to meet many requirements. Trade-offs may have to be made and as a result a pure linearly polarized or circularly polarized antenna may not be possible or necessary.

### 2.2.6 RFID Tag Antenna Input Impedance

The impedance which is presented by the antenna at its terminals, in other words the ratio of the voltage to current at the antenna terminals defines the antenna input impedance ( $Z_a$ ). The mathematical expression of impedance is shown as:

$$Z_a = \frac{V_{in}}{I_{in}} = R_A + jX_A. \quad (2.9)$$

where,  $V_{in}$  and  $I_{in}$  are the input voltage and current at the terminals. The input impedance is a complex number, where the real part consists of two components:

$$R_A = R_r + R_L. \quad (2.10)$$

where,  $R_r$  is the radiation resistance and  $R_L$  is the loss resistance of the antenna. The total radiated power ( $P_t$ ) with the radiation resistance is shown as:

$$R_r = \frac{2P_t}{I_{in}^2}. \quad (2.11)$$

The input impedance describes the antenna input behaviour as a circuit element. It is important to match this input impedance to a given source impedance, which in the case of RFID applications is the chip impedance of the transponder chip. In order to be able to deliver the maximum power from the RFID transponder chip to the antenna, the chip impedance and the antenna input impedance must be a complex conjugate pair:

$$Z_{antenna} = Z_{chip}^* \quad (2.12)$$

Separated into real and imaginary parts, the following conditions are achieved:

$$R_{antenna} = R_{chip} \quad (2.13)$$

$$X_{antenna} = -X_{chip} \quad (2.14)$$

### 2.2.7 Antenna Aperture and Effective Area

There can be a number of equivalent areas associated with an antenna. These areas can be used in order to describe the power capturing characteristics of an antenna when influenced by a wave. One of these equivalent areas is named as the *effective area (aperture)*, which is "the ratio of the available power at the terminals of a receiving antenna to the power flux density of a plane wave incident on the antenna from that direction, the wave being polarization-matched to the antenna. If the direction is not specified, the direction of maximum radiation efficiency is implied." It can be expressed mathematically as:

$$A_e = \frac{P_t}{W_i} = \frac{|I_T|^2 R_T / 2}{W_i} \quad (2.15)$$

where,  $A_e$  is the effective area (effective aperture) in  $m^2$ ,  $P_t$  is the delivered power to the load in Watts and  $W_i$  is the power density of the incident wave in  $(W/m^2)$ .

The product of the incident power density with the area which is the effective aperture gives the power delivered to load. This can be shown as:

$$A_e = \frac{|V_T|^2}{2W_i} = \left( \frac{R_T}{(R_r + R_L + R_T)^2 + (X_A + X_T)^2} \right). \quad (2.16)$$

The following equation can be used to derive the link between the  $A_e$  to antenna physical aperture  $A_p$  by the aperture efficiency:

$$\eta_{ap} = \frac{A_e}{A_p}. \quad (2.17)$$

and the  $A_e$  can also be found as:

$$A_e = \frac{\lambda^2}{4\pi} D. \quad (2.18)$$

Estimating the received power is also possible as long as the power density  $S$  is known:

$$P_r = SA_e. \quad (2.19)$$

When the maximum power transfer (conjugate matching) occurs,  $R_r + R_L = R_T$  and  $X_A = -X_T$ , the effective area reduces to the maximum effective aperture shown as:

$$A_{em} = \frac{|V_T|^2}{8W_i} \left( \frac{R_T}{(R_r + R_L)^2} \right) = \frac{|V_T|^2}{8W_i} \left( \frac{1}{(R_r + R_L)} \right). \quad (2.20)$$

It is also possible to derive the relationship between the *maximum effective area* (MEA) and the *maximum directivity* ( $D_0$ ) of an antenna by using Equation 2.21:

$$A_{em} = \frac{\lambda^2}{4\pi} D_0. \quad (2.21)$$

This equation assumes that there are no conduction-dielectric losses, the antenna is matched and there is no reflection and polarization losses. Equation can be rewritten by including these parameters in order to include the effects of these parameters on the maximum effective area.

### 2.2.8 Polarisation Mismatch

Polarization loss is one of the factors which affects the read range of RFID tags. It is described as the polarization difference between the incoming wave and the receiving antenna. The electric field of the incoming wave is shown mathematically as  $E_i = \hat{\rho}_w E_i$  where  $\hat{\rho}_w$  is the unit vector of the wave. The polarization of the electric field of the receiving antenna is shown as,  $E_a = \hat{\rho}_a E_a$ , where  $\hat{\rho}_a$  is the polarization vector as shown in Figure 2.4.

The *polarization loss factor* (PLF) is defined as [11]:

$$PLF = |\hat{\rho}_w \cdot \hat{\rho}_a|^2 = |\cos \psi_p|^2. \quad (2.22)$$

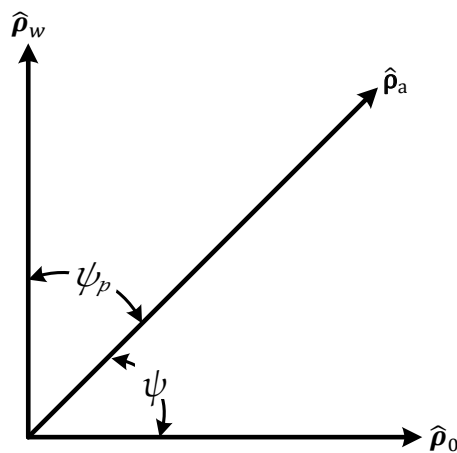


Figure 2.4: Polarisation of the antenna and the waves.

In order to obtain the received power by the antenna when it is not perfectly polarized, the product of PLF and the received power is a convenient method.

In cases where the polarization of the tag is not known, the PLF is assumed as 0.5 or -3 dB as the reader antenna is circularly polarized in most RFID systems.

### 2.2.9 Sensitivity of the Transponder

In order to activate the transponder chip by supplying sufficient energy for the operation of the circuit, a minimum received field strength  $E$  is necessary. The minimum field strength, (interrogation field strength  $E_{min}$ ) is derived [1] by the minimum required RF input power  $P_{e-min}$  and the antenna gain,  $G$ , as:

$$E_{min} = \sqrt{\frac{4\pi \cdot Z_0 \cdot P_{e-min}}{\lambda_0^2 \cdot G}}. \quad (2.23)$$

where,  $Z_0$  is the free space impedance.

The reader and the tag antennas are assumed as perfectly polarized in Equation 2.23. Therefore, any depolarization would increase  $E_{min}$ .

### 2.2.10 Functional Impedance of the Transponder Chip

The input impedance of the transponder chip is shown by a simple equivalent circuit in Figure 2.5 by a parallel circuit of load resistance  $R_L$ , chip input capacitance  $C_c$  and a modulation impedance  $Z_{mod}$ . The modulation impedance  $Z_{mod}$  of the microchip is used to encode the low and high digital states.

The RFID transponder chip impedance is expressed as:

$$Z_{chip} = jX_{chip} + R_{chip} = \frac{1}{j\omega C_c + \frac{1}{R_L} + \frac{1}{Z_{mod}}}. \quad (2.24)$$

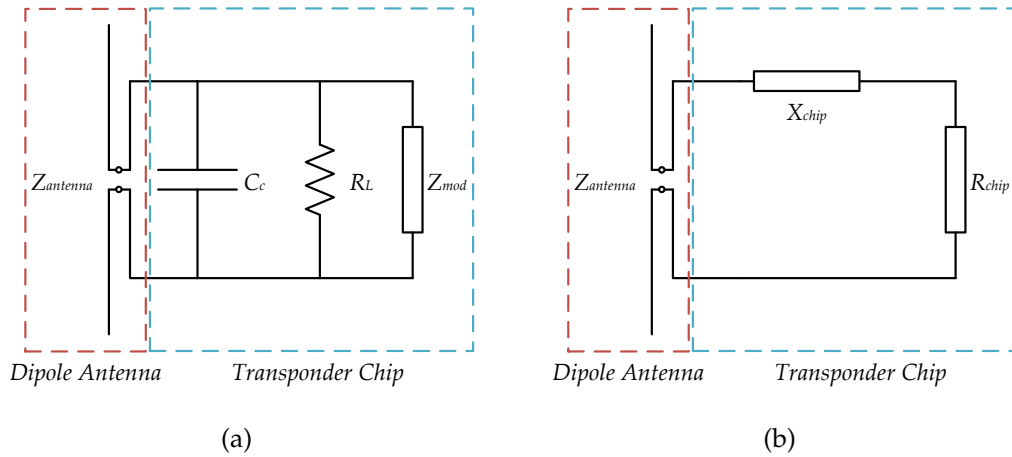


Figure 2.5: (a) Equivalent circuit of main circuit components and (b) Simplified equivalent circuit.

and thus, the following is true when the imaginary and real parts are separated:

$$R_{chip} = \text{Re} \left( \frac{1}{j\omega C_c + \frac{1}{R_L} + \frac{1}{Z_{mod}}} \right). \quad (2.25)$$

$$X_{chip} = \text{Im} \left( \frac{1}{j\omega C_c + \frac{1}{R_L} + \frac{1}{Z_{mod}}} \right). \quad (2.26)$$

### 2.2.11 Tag Antenna Scattering Aperture

A tag antenna collects power from the incident wave and delivers part of it to the termination, namely the microchip with load impedance  $Z_T$ . The remaining power is re-radiated by the tag antenna. The equivalent circuit of the tag antenna and chip is shown in Figure 2.6 to show the scattering mechanism of the antenna where the real part of the antenna impedance is split into two parts: the radiation resistance,  $R_r$ , and the ohmic loss resistance,  $R_L$ . The voltage source represents an open circuit RF voltage induced in the receiving antenna, and produces a current  $I$  through the antenna impedance  $Z_a$  and the series terminating impedance  $Z_T$  [3].

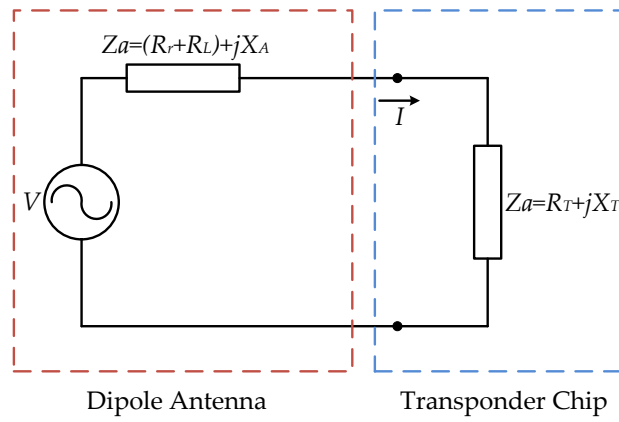


Figure 2.6: Equivalent circuit of an RFID tag.

The current  $I$  is determined by dividing the voltage  $V$  by the series connection of the individual impedances:

$$I = \frac{V}{Z_a + Z_T} = \frac{V}{(R_r + R_L + R_T) + j(X_A + X_T)}. \quad (2.27)$$

where,  $I$  and  $V$  are the RMS values.

The power delivered by the antenna to the microchip is:

$$P_{tag-chip} = |I|^2 R_T = \frac{|V|^2 R_T}{(R_r + R_L + R_T)^2 + j(X_A + X_T)^2}. \quad (2.28)$$

The effective aperture  $A_e$  of the antenna is calculated by dividing the received power  $P_{tag-chip}$  to the incident wave density which can be derived from Equation 2.19:

$$A_e = \frac{P_{tag-chip}}{S} = \frac{|V|^2 R_T}{S[(R_r + R_L + R_T)^2 + j(X_A + X_T)^2]}. \quad (2.29)$$

The maximum power transfer (conjugate matching) occurs, when  $R_r + R_L = R_T$  and  $X_A = -X_T$ , leading to the maximum effective aperture:



$$A_{e-max} = \frac{V^2}{4SR_T}. \quad (2.30)$$

The current also flows through the antenna impedance,  $Z_A$ . The real part of the impedance,  $R_A$  has two parts:  $R_A = R_L + R_r$ , the ohmic loss resistance  $R_L$  and the radiation resistance  $R_r$ . Therefore, the power dissipated as heat in the antenna is given by:

$$P_L = |I|^2 R_L. \quad (2.31)$$

The remainder is 'dissipated' in the radiation resistance. In other words, it is re-radiated into space by the antenna. This re-radiated power can be written as:

$$P_s = |I|^2 R_r = \frac{|V|^2 R_r}{(R_r + R_L + R_T)^2 + j(X_A + X_T)^2}. \quad (2.32)$$

The scattering aperture of the antenna,  $A_S$ , can be defined as the ratio of the re-radiated power to the power density of the incident wave:

$$\sigma_{ant} = A_S = \frac{P_s}{S} = \frac{|V|^2 R_r}{S[(R_r + R_L + R_T)^2 + j(X_A + X_T)^2]}. \quad (2.33)$$

If the antenna is operating under a maximum power transfer condition and lossless, ( $R_L = 0$ ,  $R_r = R_T$ , and  $X_A = X_T$ ) then the tag scattering aperture is:

$$\sigma_{ant} = A_S = \frac{V^2}{4SR_r}. \quad (2.34)$$

Therefore, in the case of conjugate impedance matching,  $\sigma_{ant} = A_S = A_{emax}$ . This suggests that only half of the total power drawn from the incident wave is supplied to the terminating resistor  $R_T$ . The other half is re-radiated by the

antenna. When the antenna is resonant short circuited [11], with  $R_T = 0$ , and  $X_T = X_A$ . It can be found as:

$$\sigma_{ant-max} = A_{S-max} = \frac{V^2}{SR_r} = 4A_{e-max}. \quad (2.35)$$

As a result, for the resonant short-circuit condition, the tag antenna scattering aperture is 4 times as great as its maximum effective aperture. For the case when the antenna is open circuited, i.e.  $Z_{T \rightarrow \infty}$ ; the aperture size is straightforward to obtain:

$$\sigma_{ant-min} = A_{S-min} = 0|_{z \rightarrow \infty}. \quad (2.36)$$

The scattering aperture of the tag antenna can thus take any desired value in the range 0-4  $A_{e-max}$  at varying values of the terminating impedance  $Z_T$ . In particular, the antenna-mode-RCS is ideally 4 times (or 6 dB) larger for the resonant short circuit relative to the conjugate matched case. This property is utilized for the data transmission from tag to reader in backscattering RFID systems.

### 2.2.12 Tag Power Transmission

The power transmission can be expressed as the percentage of the power which is delivered to the chip rectifier by the antenna. This factor can be listed as one of the most crucial factors which affects the tag read range. It can be shown mathematically as:

$$P_{chip} = \tau P_{r(tag)}. \quad (2.37)$$

where  $\tau$  is the power transmission coefficient and depends on the impedance match between the microchip and the tag antenna. Chip complex impedance is given as  $Z_{chip} = R_{chip} + jX_{chip}$ , which also includes the parasitic effect of packaging and processing. The power delivered to the chip is shown in [14] as:

$$P_{chip} = (1 - |\Gamma|^2)P_{r(tag)}. \quad (2.38)$$

where  $\Gamma$  is the reflection coefficient between the antenna and the chip input impedances;  $R_a$  and  $R_{IC}$  represent the antenna and the chip input impedances; and  $X_a$  and  $X_{IC}$  are the antenna and the chip input reactance, respectively. A conjugate match ( $Z_{IC} = Z_a^*$ ) is required to establish the maximum power transfer from the tag antenna to the chip. Therefore, the  $\Gamma$  value plays a significant role on achievable read range as it represents the match quality and must be kept close to 0 for better read range. A tag where the power transmission coefficient  $\tau$  is a function of some external parameter allows the tag to function as a sensor where the reader is able to determine a corresponding change in backscattered power. This can be achieved by mismatching the tag transponder chip.

$$0 \leq \tau \leq 1 \quad \text{and} \quad \Gamma = \frac{Z_{IC} - Z_a^*}{Z_{IC} + Z_a^*}, \quad 0 < |\Gamma| < 1. \quad (2.39)$$

The power transmission coefficient is given as [10]:

$$\tau = 1 - |\Gamma|^2 = \frac{4R_a R_{IC}}{(R_a + R_{IC})^2 + (X_a + X_{IC})^2}. \quad (2.40)$$

### 2.2.13 Friis Transmission Formula

The aperture concept can also be used in order to derive the Friis transmission formula to link the transmitted and received powers between two antennas where they are separated by a distance  $r$  as shown in Figure 2.7. As mentioned earlier, the distance between the antennas must be large enough to be considered in the antenna far field region.

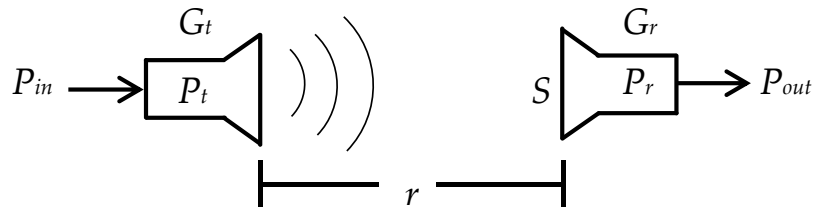


Figure 2.7: Geometrical orientation of transmitting and receiving antennas for Friis equation.

The radiation power density from an antenna with gain  $G_t$  is shown as:

$$S = \frac{P_{in} G_t}{4\pi r^2} \cdot \frac{\lambda^2}{4\pi} D_r. \quad (2.41)$$

The received power can also be retrieved by arranging Equations 2.18 and 2.19 as:

$$P_r = \frac{P_{in} G_t}{4\pi r^2} \cdot \frac{\lambda^2}{4\pi} D_r. \quad (2.42)$$

The receiving antenna efficiency factor  $\eta_{er}$  must be taken into account to calculate the output power from the receiving antenna ( $P_{out}$ ). The product of  $P_r$  with the efficiency factor will give the  $P_{out}$ . Combining Equations 2.6 and 2.42 [3, 15]:

$$P_{out} = P_r \eta_{er} = \frac{P_{in} G_t}{4\pi r^2} \cdot \frac{\lambda^2}{4\pi} D_r \eta_{er} = \left( \frac{\lambda}{4\pi r} \right)^2 G_t G_r \cdot P_{in}. \quad (2.43)$$

In order to link the input power of the transmitting antenna to the output power of the receiving antenna, the Friis transmission formula is used. The term  $(\lambda/4\pi r)^2$  is called the free space loss factor which results from the spherical spreading of the radiated energy.

Adapting this scenario into a RFID tag communication system is possible by replacing the receiver antenna with the RFID tag. Therefore, modifying the equations and replacing the receiver antenna parameters with the RFID tag antenna parameters will give an expression for the RFID communications system. Rewriting Equation 2.43 with the RFID tag parameters gives:

$$P_{r(tag)} = \left( \frac{\lambda}{4\pi r} \right)^2 G_{tag} G_{reader} \cdot P_{t(reader)}. \quad (2.44)$$

It is also possible to draw the reverse-link diagram for a directional antenna by using the Equation 2.44; the mathematical statement of the transmitted power by the reader  $P_{TX,reader}$ :

$$P_{TX,reader} = \left( \frac{\lambda}{4\pi r} \right)^4 G_{tag}^2 G_{reader}^2 \cdot P_{t(reader)}. \quad (2.45)$$

The power transmission coefficient of the tag antenna, the polarization mismatch between the reader and the tag significantly affect the received and transmitted power [14]. It is assumed in Equations 2.44 and 2.45 that the antennas are perfectly matched and there is no mismatch between the reader and the tag antennas.

### 2.2.14 Tag Read Range

Tag read range is one of the most important parameters which indicates the tag performance. It is usually defined as the maximum distance at which the tag can be read. It is easy to measure and calculate and depends on a number of factors such as the tag sensitivity and the reader antenna system parameters, the reader transmitted EIRP, reader sensitivity and path loss. By using the Friis equation, expressions for range can be derived that are useful for performance estimates. The forward-link read range is given by:

$$R_{forward} = \left( \frac{\lambda}{4\pi} \right) \sqrt{\frac{G_{tag} G_{reader} \cdot P_{t(reader)}}{P_{min.tag}}}. \quad (2.46)$$

where  $P_{min.tag}$  is the minimum power, that the tag requires the minimum signal power to establish the demodulation.

The reverse-link-limited range is given by:

$$R_{reverse} = \left( \frac{\lambda}{4\pi} \right) \sqrt[4]{\frac{G_{tag}^2 G_{reader}^2 \cdot P_{t(reader)} \cdot k}{P_{min.reader}}}. \quad (2.47)$$

where  $P_{min.reader}$  is the minimum signal power.

The exact value for  $k$  is found by the relationship between the radiation resistance of the antenna  $R_r$ , the input impedance of the transponder chip,  $Z_{chip}$ , and the relative effective aperture.

When the tag is activated, in order to receive the reflected signal which reaches the reader without any error, the signal must be sufficiently strong. Therefore, the sensitivity of a receiver indicating the required minimum field strength at the receiver input must be known. The reader is a duplex transmitter and a backscatter system. When the RFID tag is activated, significant amount of

interference is occurred which reduces the sensitivity of the receiver in the reader.

## 2.3 Conclusion and Summary

In this chapter, the basic theory of antennas, the control of current distribution which determines the radiation pattern and impedance are presented. A detailed discussion on antenna near fields and far fields has been conducted. The important parameters of an antenna and the RFID tag antenna design from the field point of view and the circuit point of view have been defined and discussed. The Friis transmission formula and tag antenna aperture have also been addressed.

In order to design RFID tags for sensing purposes, the parameters listed above are also of interest to assess the amount of distortion or change in order to extract and compare the different scenarios.

If an RFID tag is to be modified to become a sensor, then both the electromagnetic and the circuit point of view have to be considered to design a tag which could efficiently collect and transfer power to the microchip and backscatter chip stored information to the reader.

Designing tags to function in harsh electromagnetic environments is highly challenging as the detuning and efficiency reduction drastically affect both the circuit and electromagnetic properties of the antenna. In this thesis, body worn RFID sensor tags are studied and the body vicinity effects are also considered in the design processes.

## References

- [1] K. Finkenzeller, *RFID Handbook*. John Wiley & Sons Ltd, 2010, pp. 1–9.
- [2] V. D. Hunt, A. Puglia, and M. Puglia, *Introduction*. John Wiley & Sons, Inc., 2006, pp. 1–4.
- [3] X. Qing and Z. N. Chen, *RFID Tag Antennas*. John Wiley & Sons Ltd, 2007, pp. 59–111.
- [4] B. Yang and Q. Feng, “A folded dipole antenna for RFID tag,” in *Microwave and Millimeter Wave Technology, 2008. ICMMT 2008. International Conference on*, vol. 3, April 2008, pp. 1047–1049.
- [5] L. Ukkonen, D. Engels, L. Sydanheimo, and M. Kivikoski, “Planar wire-type inverted-F RFID tag antenna mountable on metallic objects,” in *Antennas and Propagation Society International Symposium, IEEE*, vol. 1, June 2004, pp. 101–104.
- [6] L. Ukkonen, L. Sydanheimo, and M. Kivikoski, “Patch antenna with EBG ground plane and two-layer substrate for passive RFID of metallic objects,” in *Antennas and Propagation Society International Symposium, IEEE*, vol. 1, June 2004, pp. 93–96.
- [7] L. Ukkonen, L. Sydanheirno, and M. Kivikoski, “A novel tag design using inverted-F antenna for radio frequency identification of metallic objects,” in *Advances in Wired and Wireless Communication, IEEE/Sarnoff Symposium on*, Apr 2004, pp. 91–94.
- [8] S. Padhi, N. Karmakar, C. Law, and S. Aditya, “A dual polarized aperture coupled microstrip patch antenna with high isolation for RFID applications,” in *Antennas and Propagation Society International Symposium, IEEE*, vol. 2, July 2001, pp. 2–5.



- 
- [9] J. D. Kraus and R. J. Marhefka, *Antenna for all applications*. McGraw - Hill, 2002.
- [10] "IEEE standard for definitions of terms for antennas," *IEEE Std 145-2013 (Revision of IEEE Std 145-1993) - Redline*, pp. 1–92, March 2014.
- [11] C. A. Balanis, *Fundamental Parameters and Definitions for Antennas*. John Wiley & Sons Ltd., 2007, pp. 1–56.
- [12] —, *Antenna theory: Analysis and Design*. Wiley-Interscience, 2005.
- [13] Y. Huang and K. Boyle, *Antenna Basics*. John Wiley & Sons Ltd, 2008, pp. 107–127.
- [14] G. Marrocco and F. Amato, "Self-sensing passive RFID: From theory to tag design and experimentation," in *Microwave Conference, 2009. EuMC 2009. European*, Sept 2009, pp. 1–4.
- [15] D. M. Dobkin, "Radio basics for UHF RFID," in *The RF in RFID*. Burlington: Newnes, 2008, pp. 51 – 101.

# CHAPTER 3

## METHODOLOGY OF UHF RFID TAG SENSOR DESIGN

\* \* \*

This chapter addresses a guide to design accurate and efficient passive UHF RFID tags which are proposed for sensing purposes for assisted living technologies. Sensor tag antenna impedance matching methods are discussed as this is the parameter used to detect a change. The simulation methods and optimization are discussed. Tag sensor prototyping and tag sensor performance measurement methods are also presented.

### 3.1 Introduction

One of the main difficulties in UHF RFID tag design is to achieve an efficient functionality when attached to the body which is due to the high loss and permittivity of tissue. This strongly influences the antenna impedance matching which is very challenging to match to because of limiting factors such as dimension restrictions.

In many applications, the sensitivity of the tags to environmental changes is usually considered as a negative effect and counted as one of the major disadvantages of UHF RFIDs. However, this effect can be transformed into an advantage in some cases and used for sensing purposes. Factors such as humidity [1–3], the proximity of dielectric materials such as body tissue [4–7] and metal [8, 9] has a known effect on tag functionality so it is possible to use RFID tags as sensors by their reaction to these factors. Thus, a strategy to develop tags which are able to communicate robustly with the reader and sense the environment variation is a challenging but timely research area. RFID tag design methodology and the ways to use it for sensing purposes are discussed in this chapter.

Most sensor tags are fabricated as printed dipoles to be used for omnidirectional communications. In this work, the design goal is to achieve microchip conjugate impedance matching while attached onto the body and to miniaturize the antenna shape too. Matching tag antenna impedance with chip complex impedance has been discussed in numerous publications, for example [10–12]. This work is aimed at producing a design methodology to efficiently design tag antennas which are used for sensing purposes when attached to the body and the effect on the function by various body movements which will be explained in Chapter 5 and 6 in detail.

RFID sensor tag design from scratch to the final stage is explained in detail for design, simulation and measurement stages in this chapter.

## 3.2 Tag Performance Assessment

As mentioned in Chapter 2, tag read range is evaluated by the Friis Equation. Extrapolating the performance indicators such as required transmitted power, backscattered power and read range are the key indicators.

### 3.2.1 Transmitted Power

Transmitted power is the first step of the reader-tag communications. It is the emitted power by the reader required to activate the tag at distance  $r$ . The derivation of the equations are presented in Chapter 2. Backscattered power is given by:

$$P_{out} = \left( \frac{\lambda_0}{4\pi r} \right)^2 G_t(\theta, \phi) \cdot G_r(\theta, \phi) \cdot \tau \cdot \rho(\theta, \phi) \cdot P_{in}. \quad (3.1)$$

where  $\lambda_0$  is the free-space wavelength of the carrier tone emitted by the reader;  $\theta$  and  $\phi$  are the angles of a spherical coordinate system centred at the tag;  $P_{in}$  is the power entering the reader's antenna;  $G_r(\theta, \phi)$  is the gain of the reader antenna;  $\rho$  is the polarization factor accounting for the mutual orientation of the reader-tag;  $G_t(\theta, \phi)$  is the gain of the tag and  $\tau$  is the power transmission coefficient between the tag's antenna and transponder chip.

Transmitted power can also be used to establish the tag sensing state, then either variables in the transmission path such as polarization and reflections must

be assumed to be stable and consistent or must be calibrated to achieve consistent results, so the use of transmitted power and turn-on power relationship with the impedance matching are studied in this chapter.

### 3.2.2 Backscattered Power

The radar equation defines the backward link; the power backscattered by the tag and collected by the reader, assuming perfect impedance matching ( $\tau = 1$ ), is equal to:

$$P_{r(tag)} = \frac{1}{4\pi} \left( \frac{\lambda_0}{4\pi r^2} \right)^2 G_r^2 \cdot \rho(\theta, \phi) \cdot P_{in} \cdot \sigma(\theta, \phi). \quad (3.2)$$

where  $\sigma(\theta, \phi)$  is the tag's radar cross-section, related to the modulation impedance  $Z_{mod}$  of the microchip to encode the low and high digital state:

$$\sigma(\theta, \phi) = \frac{\lambda_0^2}{4\pi} \cdot G_t^2(\theta, \phi) \cdot \left( \frac{2R_A}{|Z_{mod} + Z_A|} \right)^2. \quad (3.3)$$

It is assumed to correspond to the binary modulating state having  $Z_{mod} = Z_C$ .

### 3.2.3 Read Range

Maximum read range is considered as the primary tag performance indicator in most cases, the tag maximum read range is considered as the tag performance indicator that best determines the tag applicability in the specific application environment as shown in Figure 6.6. The maximum read range is highly situation dependent as materials in close vicinity of the tag will affect the tag antenna radiation characteristics and the backscattered power from the tag will interact with obstacles between the reader and tag antennas. From the maximum read range point of view, comparison of tags is hence only convenient

when a known stable environment is defined. When defined as free-space, the Friis transmission equation may be used to estimate the maximum tag read range as:

$$d_{max}(\theta, \phi) = \frac{\lambda_0}{4\pi} \sqrt{\frac{EIRP \cdot G_t(\theta, \phi) \cdot \tau \cdot \rho(\theta, \phi)}{P_{chip}}}. \quad (3.4)$$

where  $EIRP$  is the equivalent isotropic radiated power by the reader and  $P_{chip}$  is the power required to activate the transponder chip.

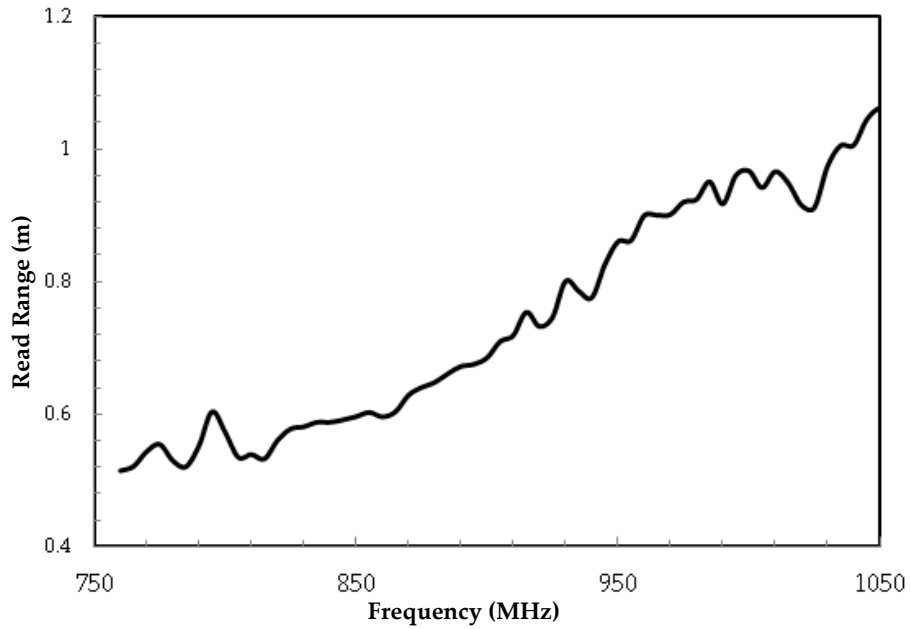


Figure 3.1: Example of measured read range against frequency for body mounted UHF tag.

### 3.3 Sensing

As mentioned in Section 3.1, external environment changes are observed and usually considered as a negative effect in UHF RFIDs where the antenna detunes and is sensitive to some factor in the environment. However, exploiting this sensitivity, passive UHF RFID tags can be used as sensors in this work. They

provide potentially lightweight and wireless sensing resources that are easily integrated or attached to the body.

When the tag is exposed to some physical or geometrical external factor (such as stretch) symbolized by  $[\Psi]$ , this reflects as a modification of the antenna input impedance  $Z_A[\Psi]$  and gain,  $G_T[\Psi]$  and accordingly of the amplitude and phase of the received backscattered signal. In RFID sensing technology, the change of external factor  $[\Psi]$  is indicated by using the required transmit and the received powers.

### 3.3.1 Turn-on power to activate the chip

The turn-on power  $P_{turn-on}$  is the required minimum power to activate the RFID tag. It is listed as the first parameter which can be obtained by the forward link.  $P_{turn-on}$  is obtained by rearrangement of Equation 3.3 as a function of the external parameter of interest  $[\Psi]$ :

$$P_{turn-on}(\theta, \phi)[\Psi] = \left( \frac{4\pi r}{\lambda_0} \right)^2 \frac{P_{chip}}{G_r(\theta, \phi) \cdot \rho[\Psi] \cdot G_t(\theta, \phi) \cdot \tau[\Psi]}. \quad (3.5)$$

It is possible to use the turn-on power value to communicate a sensed value. Therefore, a decrease or an increase in the turn-on power can be related to a sensed parameter. So monitoring this parameter leads to a method to distinguish between the different states of the tag sensor transfer response.

The Voyantic Tagformance Lite equipment was used for the measurements. This system ramps transmit power and records the value when a tag under test communication is established (turn-on power) as shown in Figure 3.2.

Table 3.1 is provided to show how the measured data can be used for sensing purposes. By these results it is observed that the tag can be treated like a switch indicating the current state depending on the time between  $t_0$  and  $t_1$  that the

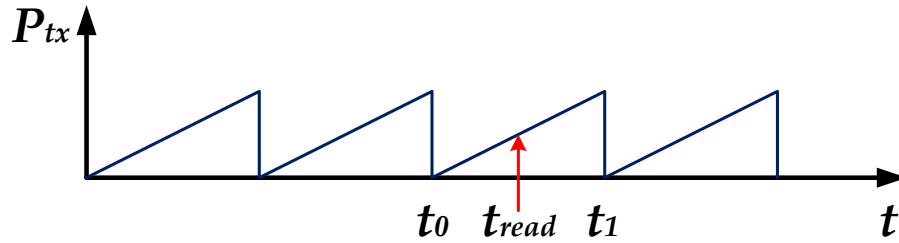


Figure 3.2: Activation of tag by ramping the transmitted power.

tag reads. The functions identified in the Table 3.1 are 'switch on' when the tag reads for low transmitter power, 'switch off' where the tag will not read even at maximum reader power and 'sensor' where the tag reads with a response proportional to the reader transmit power.

Table 3.1: Required transmitted power.

Time of Read	Switch State	Function
$t_0$	Closed	Switch on
$t_0 < t < t_1$	Variable	Sensor
Approaching $t_1$	Open	Switch off
No read	Open	Switch off

When the backward link is also considered,  $P_{turn-on}$  and backscattered power can be combined to evaluate a quantity defined in [13, 14] as the Analog Identifier (AID):

$$AID[\Psi] = \frac{P_{chip}}{\sqrt{P_{turn-on}[\Psi] \cdot P_{r(tag)}[\Psi]}} = \frac{2R_C}{|Z_C + Z_A[\Psi]|}. \quad (3.6)$$

The AID only depends on the antenna's impedance and produces sensed results which are independent of the received signal phase and transmission channel. So it is useful in observing and assessing the effect of setup changes (position and orientation) in successive measurements.



### 3.3.2 Power Transmission Coefficient

The power transmission coefficient  $\tau$  is another parameter that can describe the sensed value. As mentioned earlier, the power transmission can be expressed as the percentage of the power which is delivered to the chip rectifier by the antenna. This factor has a crucial effect on the tag read range and the tag performance. The power transmission coefficient is given by:

$$\tau = 1 - |\Gamma|^2 = \frac{4R_a R_{IC}}{(R_a + R_{IC})^2 + (X_a + X_{IC})^2}. \quad (3.7)$$

where  $\Gamma$  is the reflection coefficient between the antenna and the chip input impedances;  $R_a$  and  $R_{IC}$  represent the antenna and the chip input impedances; and  $X_a$  and  $X_{IC}$  are the antenna and the chip input reactance, respectively. A conjugate match ( $Z_{IC} = Z_a^*$ ) is required to establish the maximum power transfer from the tag antenna to the chip. Therefore,  $\Gamma$  value plays a significant role on achievable read range as it represents the match quality and must be kept close to 0 for better read range. A tag where the power transmission coefficient  $\tau$  is a function of some external parameter allows the tag to function as a sensor where the reader is able to determine a corresponding change in backscattered power. This can be achieved by mismatching the tag transponder chip.

The relationship between the tag performance and the power transmission coefficient may also be used as a means to observe the different states of the tag. The magnitude of the change in the  $\tau$  indicates a change in the tag performance and can be related to states of the tag as shown in Table 3.2.

So a change in  $\tau$  can be ascertained at the reader, either by the required EIRP in the forward link to activate the tag, or by the backscattered power in the reverse link.

Table 3.2: Power transmission coefficients.

Power Transmission Coefficient ( $\tau$ )	Required reader EIRP	Modulated Backscattered Power
$\tau \rightarrow 1$	Minimum	Maximum
$0 < \tau < 1$	Medium	Medium
$\tau \rightarrow 0$	Maximum	Minimum
$\tau = 0$	-	No read

### 3.4 UHF RFID Tag Antenna Design Process

The available power from the reader antenna and the power transmission coefficient from the tag antenna to the transponder chip are the two principal constraints limiting RFID tag operation. Therefore, efficient power transfer is the key in the tag design. Efficient power transfer, is determined by the tag antenna and RFID transponder chip impedance matching, where the transponder chip impedance is frequency and power dependant. As read range is the most important parameter indicating the tag performance, generally the main aim in the initial step is the maximum achievable read range specification in the RFID tag design process.

Maximum attainable gain and bandwidth are crucially affected by the antenna size and the frequency [15] therefore, compromises have to be made to obtain optimum tag performance to satisfy design requirements. Often a tunable antenna design is preferable to provide tolerance for tag fabrication variations and for optimizing antenna performance on different materials in different frequency bands.

The RFID tag antenna design process can be explained by the flow chart shown in Figure 3.3. System requirements and the application type can be combined and listed as tag requirements including the materials for the tag

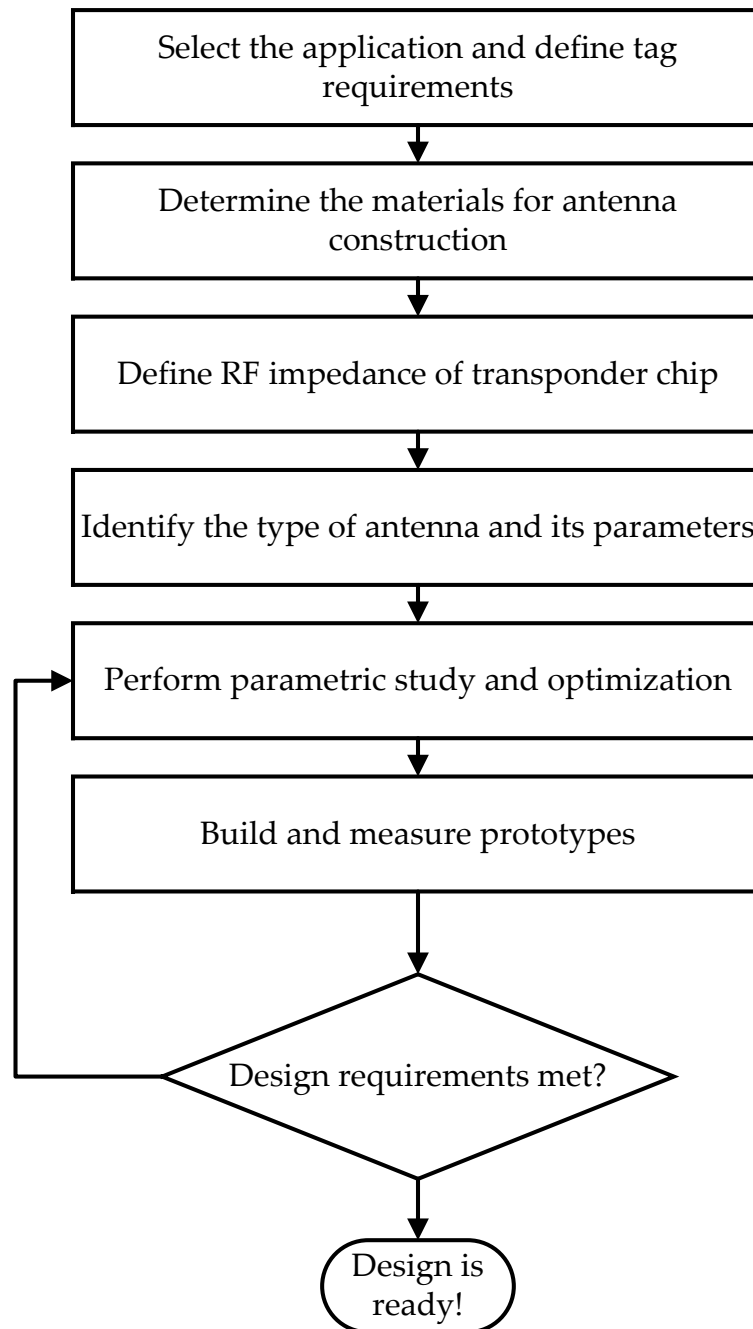


Figure 3.3: RFID tag antenna design process [16].

antenna construction. Generally, the antenna should be low profile on the object and materials that is being tagged [17].

The impedance of the selected RFID transponder chip in a chosen RF package

(strap chip, etc.) to which the antenna will be matched can be measured with a network analyser or taken from a datasheet. Antenna parametric study and optimization is performed until the design requirements are met in simulation [16].

### 3.4.1 Environmental Constraints

RFID tag antennas detune or do not function in harsh electromagnetic environments such as on high permittivity substrates or metallic surfaces. This is also true for tags which are located in the body vicinity. The body tissue environmental constraints have to be considered and modelled accurately to overcome this significant effect on the tag performance.

### 3.4.2 Impedance Matching Methods for RFID Tags

As mentioned in Chapter 2, conjugate impedance matching between the tag antenna and the transponder chip has to be established. In other words, the transponder chip's capacitive inductance must be cancelled out by the tag antenna's impedance. It is possible to match the impedances of the components with no external matching network needed, even though special tuning is necessary in most cases. The tuning is possible by altering the antenna input resistance and reactance by modifying the tag geometrical parameters. In this section, impedance matching methods including tuning techniques are outlined.

#### 3.4.2.1 T-Match

In order to change the input impedance of a planar dipole of length  $l$ , a centered short-circuit stub can be introduced as shown in Figure 3.4. The antenna source is connected to a second dipole of length  $a \leq l$ , placed at a close distance,  $b$ ,

from the first and larger dipole. The distribution of electric current occurs along the two main radiators according to the size of their transverse sections. The impedance at the source point is given by [12, 18]:

$$Z_{in} = \frac{2Z_t(1 + \alpha)^2 Z_A}{2Z_t + (1 + \alpha)^2 Z_A} \quad (3.8)$$

where  $Z_t = jZ_0 \tan(ka/2)$  is the input impedance of the short circuit stub which the T-matched conductor and part of the dipole forms as outlined in Figure 3.4;  $Z_0 \cong 276 \log_{10} b / \sqrt{r_e r'_e}$  is the characteristic impedance of the two conductor transmission line with spacing  $b$ .  $Z_A$  is the dipole impedance taken at its centre in the absence of the T-matched connection;  $r_e = 0.25w$  and  $r'_e = 0.25w'$  are the equivalent radii of the planar dipole and of the matching stub, and  $\alpha = \ln(b/r'_e) \ln(b/r_e)$  is the current division factor between the two conductors.

$a$ ,  $b$ ,  $w$  and  $w'$  are the parameters which can be modified and adjusted to achieve the chip input impedance match.

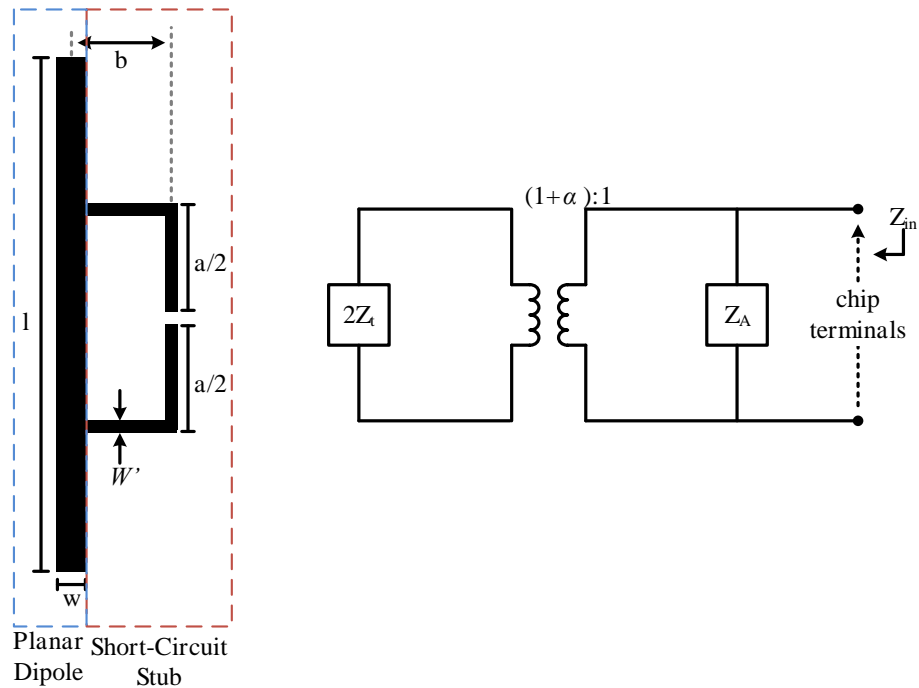


Figure 3.4: T-Match [12].

As stated in [12, 18] the T-match is used as an impedance transformer. Although the resulting input impedance at the T-match port for half-wavelength dipoles are inductive, the resulting total input impedance can be both capacitive and inductive for the smaller dipoles. In addition to this, modifying the parameter dimensions may lead to high values of input impedance and it becomes difficult to match the impedance to real microchip transmitters. Therefore, a single T-match layout could not be the best method to match the high impedance to microchip transmitters, unless the main radiator shape is modified.

### 3.4.2.2 Inductively Coupled Loop Match

An inductively coupled small loop is used to feed a radiating dipole by placing it in close proximity to the radiating body where this adds an equivalent inductance in the antenna. The distance between the loop and the radiating element controls the strength of the coupling and the reactance. The transponder chip is directly connected to the loop terminals. The geometry and the equivalent circuit of the inductively coupled loop is shown in Figure 3.5.

The inductive coupling can be considered as a transformer and the resulting input impedance on the loop's terminals is shown as:

$$Z_{in} = Z_{loop} + \frac{(2\pi f M)^2}{Z_A} \quad (3.9)$$

where, the antenna impedance is  $Z_A$  and the loop's input impedance is  $Z_{loop} = j2\pi f L_{loop}$ . The loop inductance,  $Z_{loop}$ , determines the total input impedance regardless of whether the dipole is at resonance or not. The antenna resistance,  $R_A$ , is solely related to the transformer mutual inductance,  $M$ :

$$R_{in}(f_0) = \frac{(2\pi f M)^2}{R_A(f_0)} \quad (3.10)$$

and the reactance is given by:

$$X_{in} = 2\pi f_0 L_{loop}. \quad (3.11)$$

The radiating body is assumed as infinitely long. The link between the loop's size and the separation from the dipole is shown in terms of the mutual coupling,  $M$ , and the loop's inductance mathematically in [19].

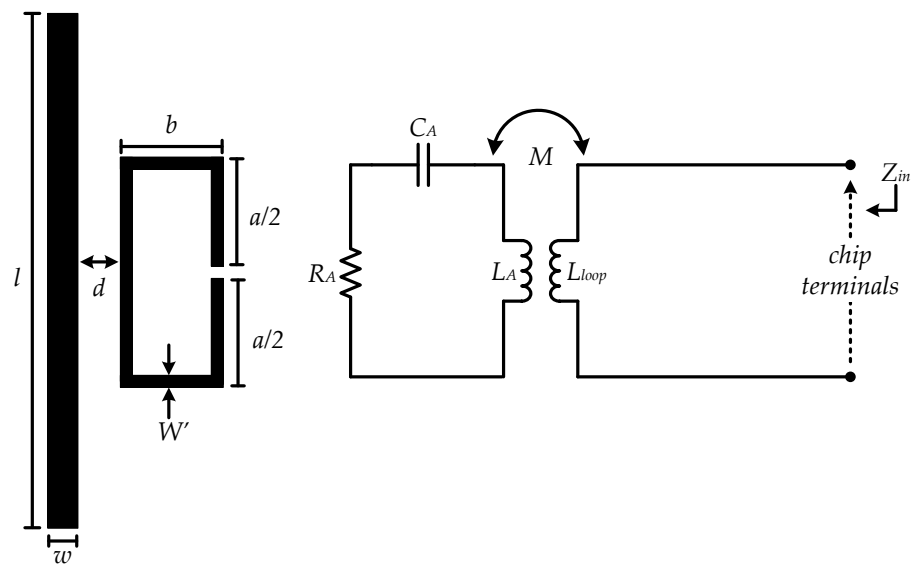


Figure 3.5: Inductively Coupled [12].

### 3.4.2.3 Nested Slot

This technique is useful for tags fabricated from large planar dipoles or suspended patches [12]. This feeding strategy has the capability of complex impedance matching, even when the tag is attached onto a high-permittivity substrate such as body tissue [4–7]. The maximum gain of the antenna is achieved mainly by the patch length  $l$ , and the impedance tuning can be determined by the slot aspect ratio, dimensions  $a$  and  $b$  as shown in Figure 3.6 where black section represent metal in the figure.

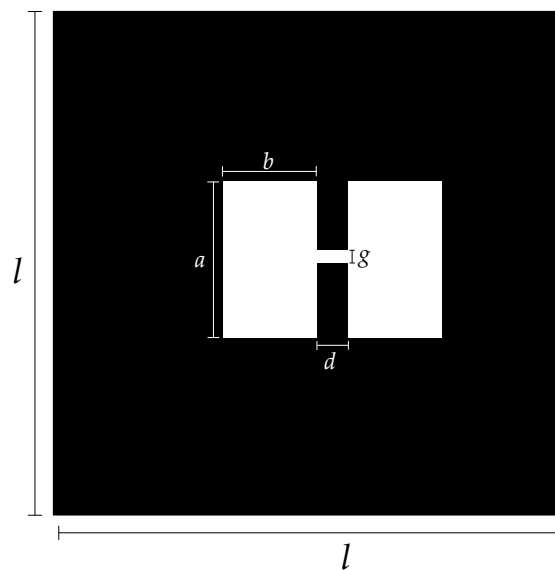


Figure 3.6: The geometry of the nested-slot suspended-patch [12].

#### 3.4.2.4 Meandering

UHF RFID tags may have to be attached to small objects in which case the dipole has to be reduced in length to fit a constrained area while not degrading radiation efficiency. Two methods to achieve this are meandering and inverted-F configurations. Both configurations require a single or multiple folding of the radiating body in order to accommodate the length required for achieving resonance at a particular frequency. The dipole antenna arms are folded along a meandered path as proposed by [12, 20, 21]. The wire configuration produced has distributed capacitive and inductive reactance that affect the overall antenna's input impedance. The transmission-line currents do not contribute to the radiated power, but instead produce losses. Resonances are achieved at lower frequencies when compared to straight dipoles of the same tag length. In addition, the bandwidth is reduced along with efficiency. The shape of the meandered dipole can be periodic or individually optimized to match the chip impedance. The total length of the meander-line antenna increases along with the reactance, and the height of the meandered segment



controls the resistance.

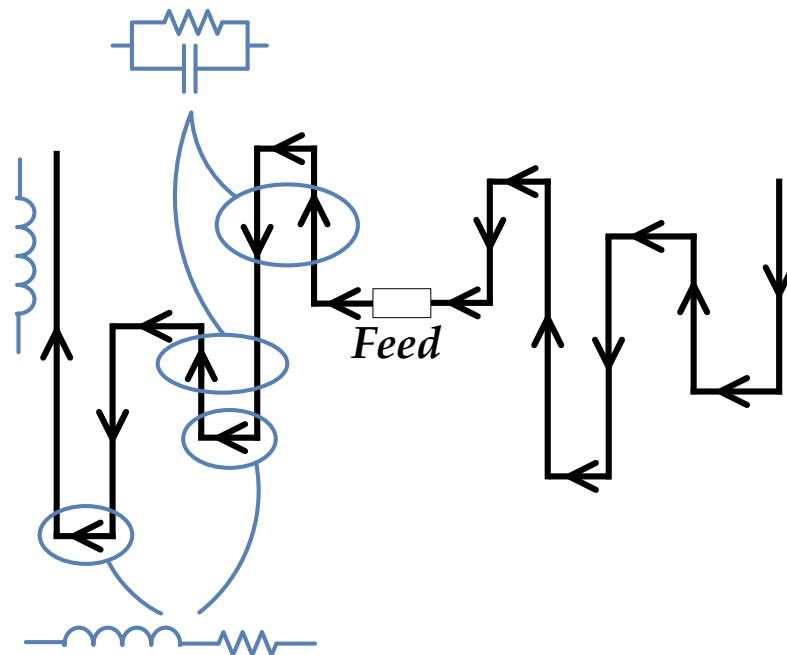


Figure 3.7: Meander line.

### 3.4.2.5 Slot Antenna Inductance and Dimensions

As slot antenna theory is important in this work, the dimensions of the slot are considered in this section. The conductive patch length affects the current distribution and it should be long enough to avoid disturbing the high density of the currents around the slot-line. It also affects the antenna gain which has higher values when the patch is resonant. Therefore the conductive patch resonant length at a required frequency is calculated using a first order approximation for a half wave patch length given by [22]:

$$L = \frac{c}{2f_r \sqrt{\epsilon_r}}. \quad (3.12)$$

where  $c$  is the speed of light in vacuum and  $f_r$  is the resonant frequency of the antenna. The patch width is chosen to be wide enough not to curtail the surface currents and is at least 3 times the slot width.

### 3.4.3 Transponder Chip Types

The RFID transponder chips are manufactured in different formats such as "strap" (shown in Figure 3.8) with the dimensions  $LA$  and  $LB$  shown in Figure 3.9. The strap format transponder chip is one of the most popular for prototyping. The attachment to the tag antenna is straight forward where the IC is connected to two mounting pads with a thin substrate. Therefore, by using a conductive glue or adhesive tape the strap is attached to the antenna by galvanic or contact connection.

Another widely used transponder chip format is the sawn die [23, 24] where flip chip technology is used to directly connect the chip to the antenna using conductive glue.

The packaged transponder chip is commonly used for RFID tags substrate or cover with thickness comparable to the chip package, usually a few millimetres. This format differs from others by having solid connections pads which can be soldered to the antenna terminals directly for more robust connections. Therefore, packaged transponder chips may be preferred for harsh environmental applications.

Minimum operating power, chip impedance and the transponder chip characteristics are usually given by the manufacturer, though additional impedance measurements may be necessary for verifying the impedance values for the desired operating frequency.

By considering the requirement of maximum power transfer in low cost RFID tag design and manufacturing practicality, the most suitable choice for an RFID

transponder chip is a planar inductive antenna with a reactance that is able to tune out the capacitance of the label IC and also provide an adequate match for its real impedance, without the need for any external matching circuit.

There is not a great range of alternative transponder chip impedances available and therefore, altering the antenna impedance for a better matching quality is more practical.

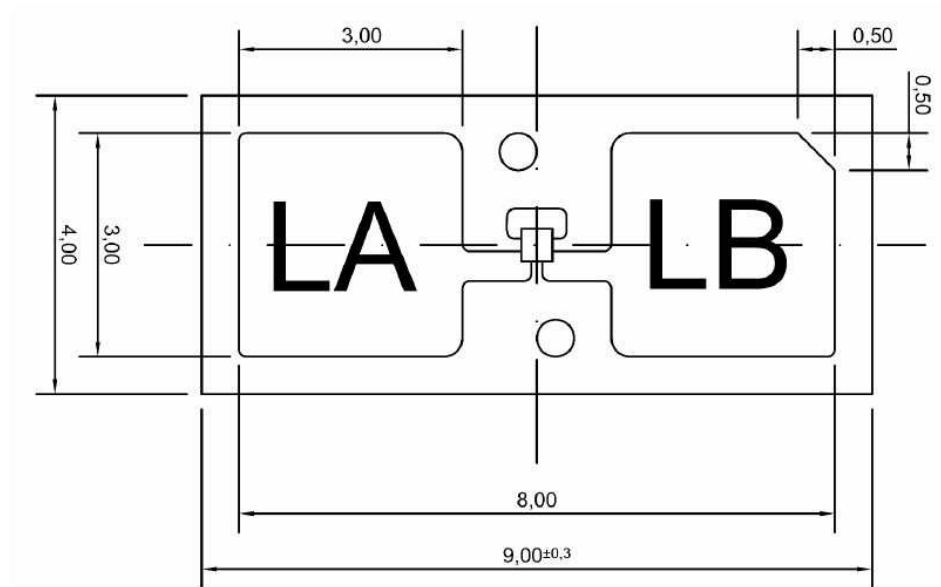


Figure 3.8: Strap NXP chip dimensions [23].

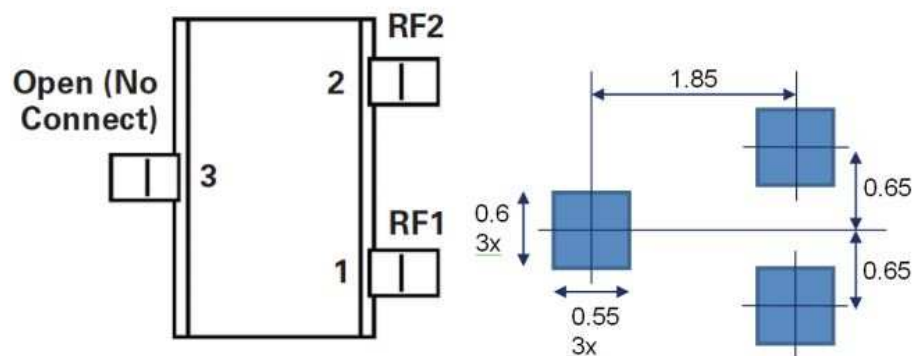


Figure 3.9: Higgs chip dimensions [24].

### 3.5 Simulation

The RFID tags which have been developed for sensing purposes on the skin or body have been simulated by using CST Microwave Studio. In this work, the time domain solver is used where Maxwell's equations are modified to central-difference equations, discretized, and implemented in the software. The electric field is solved at a given instant in time, then the magnetic field is solved at the next instant in time, and the process is repeated until a steady state is achieved. A study of computational electromagnetic is beyond the scope of this work, though further references in computational electromagnetic could be found in the referenced sources.

A fully automatic meshing procedure is applied to all the components which have been modelled. CST uses Perfect Boundary Approximation (PBA<sup>TM</sup> method) and the Thin Sheet Technique (TST<sup>TM</sup>) extension in order to increase the accuracy of the simulations. PBA is defined in [25] as a conformal method, which allows arbitrarily shaped objects to be sampled rather coarsely on the mesh. This reduces the mesh and thus also the required memory size and solution time without compromising accuracy. The TST<sup>TM</sup> extends the capabilities of PBA by enabling independent treatment of two dielectric parts of a cell, separated by a metallic sheet. The structures such as arbitrarily shaped housings or thin inclined shields can be modeled with a minimum of effort.

CST has 4 types of solver methods to run simulations: (i) transient solver, (ii) frequency domain solver, (iii) eigen-mode solver and (iv) modal analysis solver. Each are respectively better suited to particular applications.

The transient solver is the most flexible tool for microwave applications and can obtain the entire proposed frequency range behaviour of the simulated device from only one calculation run. This technique is the most suitable one for UHF RFID tag design and used to simulate the tag response in this work.

The transient solver becomes less efficient for low frequency problems where the structure is much smaller than the shortest wavelength. In these cases it can be advantageous to solve the problem by using the frequency domain solver. This approach is at its most efficient when only a few frequency points are of interest. The other solvers such as the eigen-mode solver, is more efficient for designing filters.

After deciding the theoretical dimensions and the appropriate material for the tag and the substrates, the body tissue is also considered in order to give the real life implementation of the tag and its functionality and tissue phantoms are discussed in Section 3.5.1 owing to the fact that full wave modulators are only capable of calculating problems that have finite extent, the boundary conditions need to be specified for the problem. Since tag antennas are designed to function in the far-field, "open add space" or "perfectly matched layer (PML)" with added extra space as defined in CST are used throughout this work to provide conditions appearing as open space, while being computationally efficient. These operate in a manner similar to free space where waves can effectively pass the boundary with minimal reflections.

The ports of the tag must also be modelled. This is done by placing a discrete port with a lumped element across the feed terminals of the tag antenna. The port resistance is assigned to the value of the RFID transponder chip impedance real part, while the lumped component reactance represents the chip imaginary impedance at the centre frequency.

Lower and upper frequency borders are set before starting the simulation. The recommended upper and lower frequency boundaries are 30% on either side of the frequency range of interest [25].

After all these steps, the simulation can be performed. When the simulation is done, the results are presented with a variety of different post processing options to calculate and visualise the tag performance.

### 3.5.1 Simulating RFID tag sensors on body tissue

In order to achieve reliable simulation results, the tag environment has to be modelled in detail. Body phantoms or equivalent blocks of tissue can be used demonstrate the specific areas of the body. An example of a sample tissue phantom is shown Figure 3.10 where the arm is modelled for use in strain gauge RFID sensor tag simulations as a rectangular block including bone (yellow), muscle (violet), fat (pink) and skin (beige). This model will be applied in Chapter 5

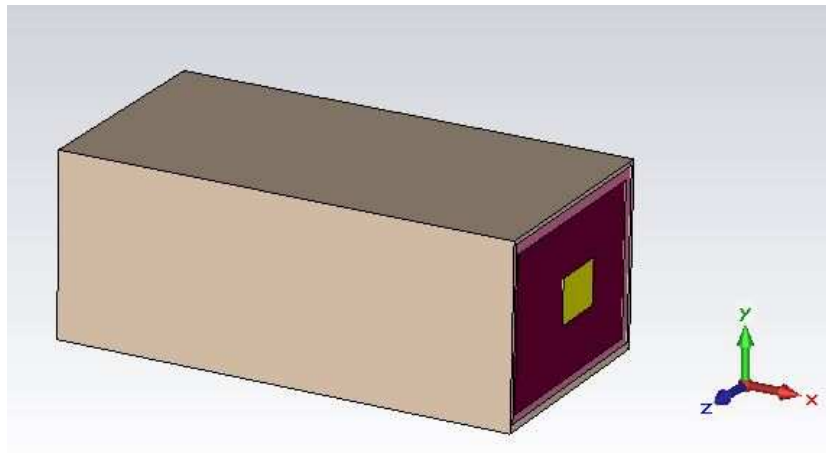


Figure 3.10: Arm phantom rectangular block.

The mouth is also modelled in detail including the tongue, teeth and gums as shown in Figure 6.3 for a complete mouth model. The electrical properties of the tissues are explained in detail for relevant tag designs in Chapters 5 and 6.

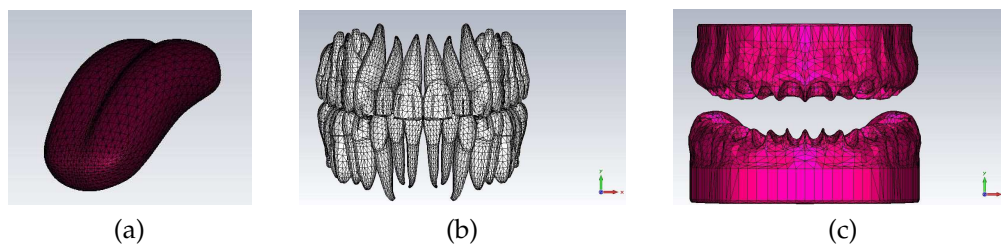


Figure 3.11: Mouth model components (a) tongue, (b) teeth and (c) gums.

### 3.5.2 Stretching Effect Simulations

In stretchable RFID tag sensor design, which is explained in detail in Chapter 5, the stretch effect is supplied by a straight forward method.

In order to give an  $x$ -axis stretch effect to a circular shaped substrate, the shape is converted into an elliptical shape by increasing the horizontal dimensions with a simultaneous decrease in the vertical dimensions with the same proportion.

For demonstrating the  $y$ -axis stretch effect on a circular shaped substrate, the shape is converted into an elliptical shape again with an increase in the vertical dimensions with a simultaneous decrease in the horizontal dimensions with the same proportion as shown in Figure 3.12.

By using this method, in order to achieve a systematic stretching effect, the parameter sweep function is used to simulate the structure from the un-stretched state to the maximum stretch state both in  $x$  and  $y$  axis in CST.

### 3.5.3 Simulation Optimisation

Simulation optimization is carried out to have consistent and reliable simulation results. There are features to take into account carefully during the simulations which need to be revised until acceptable results are achieved in terms of antenna resonant frequency, bandwidth, matching quality and far-field simulation.

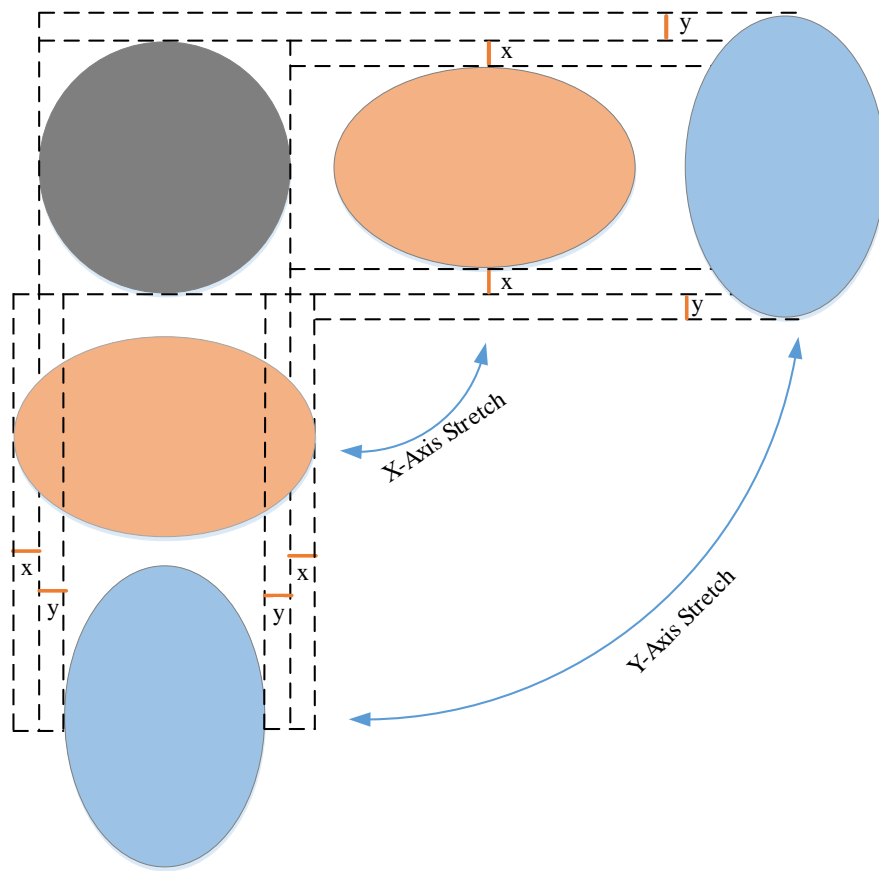


Figure 3.12: Stretch effect.

### 3.5.3.1 Meshing

The simulation mesh optimization is performed by increasing the minimum number of mesh lines in each coordinate direction based on the highest frequency of evaluation, until the change in resonant frequency and/or bandwidth is negligible. The optimised simulation setting is used to sweep the antenna parameter value to investigate each parameter effect on the tag performance and to fine tune the antenna to achieve the required characteristics such as a good power transfer coefficient over the required bandwidth.



## 3.6 Measurement Set Up

Voyantic Tagformance Lite equipment was used for measurements in this work. This system consists of a PC, RF module and a reader antenna. The tag antenna under test is placed 35 cm away from the reader in order to minimize the effect of multiple reflections and possible interference as shown in Figure 3.13.

In practice, to attain measurable read range results, that are comparable with simulation for an isolated tag, an artificial free-space environment may be used. It is advantageous to measure the tag maximum read range with fixed distance  $d$  between the reader and tag antennas.

The channel is characterized by utilizing the system calibration tag to measure the link loss factor  $L_{iso}$ , which is defined from the reader output port to the input of a hypothetical polarization-matched isotropic antenna located at a distance  $d$  away from the reader antenna. This loss factor is also included in the read range measurements by the software. The maximum distance at which a tag can be detected by the reader (read range) is a practical tag communication performance indicator. The Voyantic System is able to extrapolate read range,  $R$ , by measuring calibrated powers over the much smaller distance  $d$ .

The Voyantic System is able to extrapolate read range by measuring calibrated powers over the much smaller distance,  $d$ , by using the Friis read range equation.

The Voyantic Tagformance Lite, system can measure various parameters such as Transmitted Power and Backscattered Power for individual tags and offer population analysis of multiple tags as well.

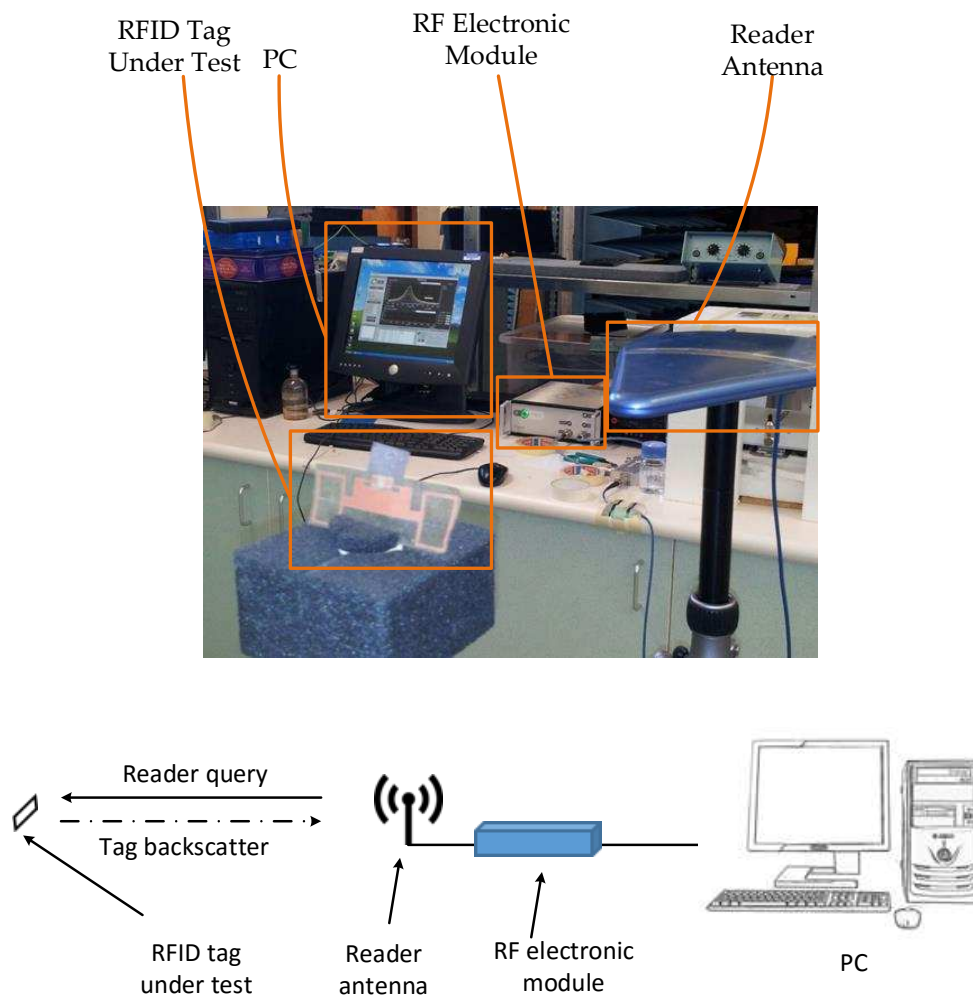


Figure 3.13: Voyantic Lite RFID measurement system.

### 3.7 Sensor Tag Prototyping and Optimisation

Following the simulation and tuning, the antenna pattern is etched in the copper cladding of a  $100\ \mu\text{m}$  thick Mylar sheet. This enables a tag antenna design to be physically validated in free space or attached to other substrates, before a tag with integrated sensing functionality is first fabricated.

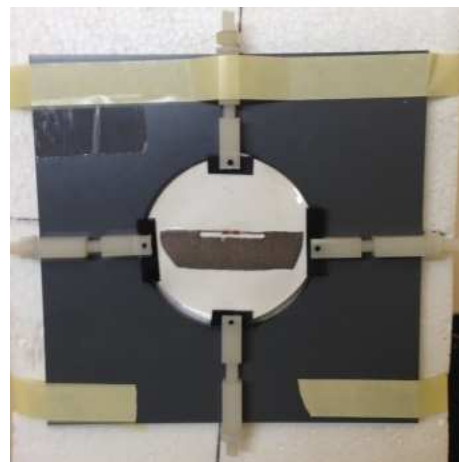
When prototyping strain gauge tags, a stretchable conductive fabric, which is used as the radiating conductive material is cut by a laser cutting method, as etching was not convenient for this type of material. This antenna design is presented in detail in Chapter 5.



(a)



(b)



(c)

Figure 3.14: RFID Sensor on (a) Air, (b) In mouth, (c) In a controllable

The prototype tag read range was measured in a lab environment with the Voyantic Tagformance measurement system. The propagation channel is eliminated by the system, after which the measured read range become largely independent of the environment.

The tag read range was measured and repeated five times and the measured read range was averaged by the average function in Voyantic Tagformance Lite software and compared then with the simulations.

As shown in Figure 3.14, the RFID tag sensor prototypes are tested at various places such as in (a) air, (b) mounted on body (in mouth) or (c) in a controllable jig, to detect changes in the required areas.

## **3.8 Conclusions**

In this chapter, methods for UHF RFID tag antenna design based on impedance matching methods are explained. Important factors which affect tag performance and the derivation of RFID tags into the sensors by monitoring these parameters are explained. Details of the simulation methods on UHF RFID sensor tags, modelling and optimisation methods are also discussed.

The actual sensor tag prototyping methods and additional manufacturing methods are introduced.

## References

- [1] L. Yang, R. Zhang, D. Staiculescu, C. Wong, and M. Tentzeris, "A novel conformal RFID-enabled module utilizing inkjet-printed antennas and carbon nanotubes for gas-detection applications," *Antennas and Wireless Propagation Letters, IEEE*, vol. 8, pp. 653–656, 2009.
- [2] T. Le, T. Thai, V. Lakafosis, M. Tentzeris, Z. Lin, Y. Fang, K. Sandhage, and C. Wong, "Graphene enhanced wireless sensors," in *Sensors, 2012 IEEE*, Oct 2012, pp. 1–4.
- [3] C. Occhiuzzi, A. Rida, G. Marrocco, and M. Tentzeris, "RFID passive gas sensor integrating carbon nanotubes," *Microwave Theory and Techniques, IEEE Transactions on*, vol. 59, no. 10, pp. 2674–2684, Oct 2011.
- [4] T. Kellomaki and L. Ukkonen, "Design approaches for bodyworn RFID tags," in *Applied Sciences in Biomedical and Communication Technologies (ISABEL), 2010 3rd International Symposium on*, Nov 2010, pp. 1–5.
- [5] S. Milici, S. Amendola, A. Bianco, and G. Marrocco, "Epidermal RFID passive sensor for body temperature measurements," in *RFID Technology and Applications Conference (RFID-TA), 2014 IEEE*, Sept 2014, pp. 140–144.
- [6] D. Oyeka, M. Ziai, J. Batchelor, V. Sanchez-Romaguera, S. Yeates, S. Wunsch, and U. Schubert, "Inkjet printed epidermal RFID tags," in *Antennas and Propagation (EuCAP), 2014 8th European Conference on*, April 2014, pp. 1403–1406.
- [7] S. Manzari, S. Pettinari, and G. Marrocco, "Miniaturized and tunable wearable RFID tag for body-centric applications," in *RFID-Technologies and Applications (RFID-TA), 2012 IEEE International Conference on*, Nov 2012, pp. 239–243.

- 
- [8] T. Bjorninen, L. Sydanheimo, L. Ukkonen, and Y. Rahmat-Samii, "Advances in antenna designs for UHF RFID tags mountable on conductive items," *Antennas and Propagation Magazine, IEEE*, vol. 56, no. 1, pp. 79–103, Feb 2014.
- [9] M. Ziai and J. Batchelor, "Curved RFID tags for metallic gas cylinders," *Electronics Letters*, vol. 45, no. 17, pp. 867–869, Aug 2009.
- [10] L. Ukkonen, M. Schaffrath, L. Sydanheimo, and M. Kivikoski, "Analysis of integrated slot-type tag antennas for passive UHF RFID," in *Antennas and Propagation Society International Symposium 2006, IEEE*, July 2006, pp. 1343–1346.
- [11] J.-S. Kim, W. Choi, G.-Y. Choi, and J.-S. Cha, "Ceramic patch antenna using inductive coupled feed for UHF RFID tag mountable on metallic objects," in *Microwave Conference, 2008. APMC 2008. Asia-Pacific*, Dec 2008, pp. 1–4.
- [12] G. Marrocco, "The art of UHF RFID antenna design: impedance-matching and size-reduction techniques," *Antennas and Propagation Magazine, IEEE*, vol. 50, no. 1, pp. 66–79, Feb 2008.
- [13] C. Occhiuzzi, S. Caizzzone, and G. Marrocco, "Passive UHF RFID antennas for sensing applications: Principles, methods, and classifications," *Antennas and Propagation Magazine, IEEE*, vol. 55, no. 6, pp. 14–34, Dec 2013.
- [14] G. Marrocco, "RFID grids: Part I; Electromagnetic Theory," *Antennas and Propagation, IEEE Transactions on*, vol. 59, no. 3, pp. 1019–1026, March 2011.
- [15] R. F. Harrington, "Effect of antenna size on gain, bandwidth, and efficiency," *Journal of Research of the National Bureau of Standards, Section D: Radio Propagation*, vol. 64D, 1960.
- [16] K. Rao, P. Nikitin, and S. Lam, "Antenna design for UHF RFID tags: a review and a practical application," *Antennas and Propagation, IEEE Transactions on*, vol. 53, no. 12, pp. 3870–3876, Dec 2005.

- [17] G. Zamora, S. Zuffanelli, F. Paredes, F. Martin, and J. Bonache, "Design and synthesis methodology for UHF-RFID tags based on the T-Match network," *Microwave Theory and Techniques, IEEE Transactions on*, vol. 61, no. 12, pp. 4090–4098, Dec 2013.
- [18] C. A. Balanis, *Antenna theory: Analysis and design*. Wiley-Interscience, 2005.
- [19] L. Youbok, "Antenna circuit design for rfid applications," *Microchip Technology Inc*, pp. 1–50, 2003.
- [20] G. Marrocco, "Gain-optimized self-resonant meander line antennas for RFID applications," *Antennas and Wireless Propagation Letters, IEEE*, vol. 2, no. 1, pp. 302–305, 2003.
- [21] M. Keskilampi and M. Kivikoski, "Using text as a meander line for RFID transponder antennas," *Antennas and Wireless Propagation Letters, IEEE*, vol. 3, no. 1, pp. 372–374, Dec 2004.
- [22] W. Stutzman and G. Thiele, *Antenna Theory and Design*. Wiley, 2012.
- [23] "NXP," 2014, Accessed: 10.03.2014. [Online]. Available: <http://www.nxp.com/>
- [24] "Higgs," 2014, Accessed: 10.03.2014. [Online]. Available: <http://www.alientechnology.com/ic/higgs-3/>
- [25] "Computer Simulation Technology," 2014, Accessed: 10.03.2014. [Online]. Available: <http://www.cst.com/>

# CHAPTER 4

## DIELECTRIC MEASUREMENTS AND ELECTROMAGNETIC BAND-GAP STRUCTURES

\* \* \*

Body-worn antennas suffer from near body effects when they are attached very close to the body. A compact, lightweight and thin electromagnetic band-gap (EBG) structure, between the antenna and the body may be necessary to eliminate the body effect and to make the antenna more efficient. High dielectric constant ( $\epsilon_r$ ) substrates have an impact on thickness reduction in EBG structures. In this chapter a mushroom-like EBG structure is presented along with the waveguide electrical properties measurement method to assess high



permittivity substrate characteristics of Titanium Dioxide,  $\text{TiO}_2$ , and its effect on the size reduction of EBG structures.

## 4.1 Introduction

Substrate relative dielectric constant ( $\epsilon_r$ ) is one of the key factors which influences antenna performance. Therefore, detailed assessment of material dielectric constant and loss tangent ( $\tan \delta$ ) by reliable methods will lead to improved microwave antenna design.

The thickness of mounting structures plays an important role in body-worn antenna systems in terms of ease of wear, compactness and conformal fit to the body. Multiple ways have been reported, for instance to obtain [1, 2] size-reduction and compact electromagnetic band-gap (EBG) structures for body worn applications. In EBG structure design, when placed onto a body, the use of a high permittivity substrate such as  $\text{TiO}_2$  is another way to bring about decrease in the thickness of the structure. As it is available in powder form,  $\text{TiO}_2$  is investigated as a suitable substrate for flexible material which result in smaller EBG patches at 400 MHz. Therefore,  $\text{TiO}_2$  dielectric constant measurements achieved by a waveguide measurement method are used in this project to verify the electrical characteristics of substrates for worn EBGs.

In [3], an EBG is defined as "*artificial periodic (or sometimes non-periodic) objects that prevent/assist the propagation of electromagnetic waves in a specified band of frequency for all incident angles and all polarization states*". Therefore, for body worn applications, the affect of body vicinity on the antenna propagation can be minimized and the propagating signal can be assisted by an EBG structure when placed between the body and the antenna, therefore allowing the antennas to work efficiently when very close to the body surface.

The interaction between electromagnetic fields and materials is separable into the electric field effect and the magnetic field effect. A material's bound and free electrons are displaced by the electric field while the atomic moments are oriented by the magnetic field [4]. The resulting effects on electric and magnetic flux densities within the material are well known, meaning that material characteristics are important in microwave engineering and antenna design. This chapter combines the assessment of material characteristics such as dielectric constant ( $\epsilon_r$ ) with the loss tangent ( $\tan \delta$ ) and the important role of these characteristics on the potential thickness reduction of the EBG structure along with the disadvantages of the thin high dielectric constant substrates which results in narrow bandwidth behaviour.

In order to check the reliability and the consistency of the waveguide dielectric constant measurement method, measurements were repeated with well characterized materials such as PTFE and wax (paraffin). As  $\text{TiO}_2$  is a fine powder it is a good exercise to assess the effect of materials on the system reliability materials.

Many studies of body centric communications have been at wireless local area network (WLAN) bands and higher. Here, the considered bands are those used by the police and emergency services, for instance 400 MHz in Europe [5]. At these bands EBGs become very thick and unwieldy if their electrical thickness is to support a sufficiently wide band-gap. The aim of the work is to achieve a reduction in the thickness of the structure by using high permittivity substrates, such as  $\text{TiO}_2$  for convenience of wear and conformal fit to the body while placed between the antenna and the body.

## 4.2 EBG Structure Design

As mentioned in the introduction section of the chapter, electromagnetic band gap structures are designed to prevent the propagation of electromagnetic waves in a specified band for all incident angles and all polarization states. The EBG structure discussed here is designed for body-worn applications.

A parametric study of the mushroom-like EBG structure discussed here is presented in [6]. The parameters which influence the behaviour of the EBG and the resonant frequency can be listed as, patch width,  $w$ , patch length,  $l$ , the spacing between patches,  $s$ , substrate thickness,  $h$  and the substrate permittivity,  $\epsilon_r$  and via connections radius,  $r$ . This section focuses on the effect of substrate permittivity  $\epsilon_r$  and thickness on the EBG response.

EBG structures consist of a ground plane, dielectric substrate, metallic patches and vias to connect patches to the ground plane. The whole structure can be expressed by its equivalent lumped LC elements as shown in Figure 4.1.

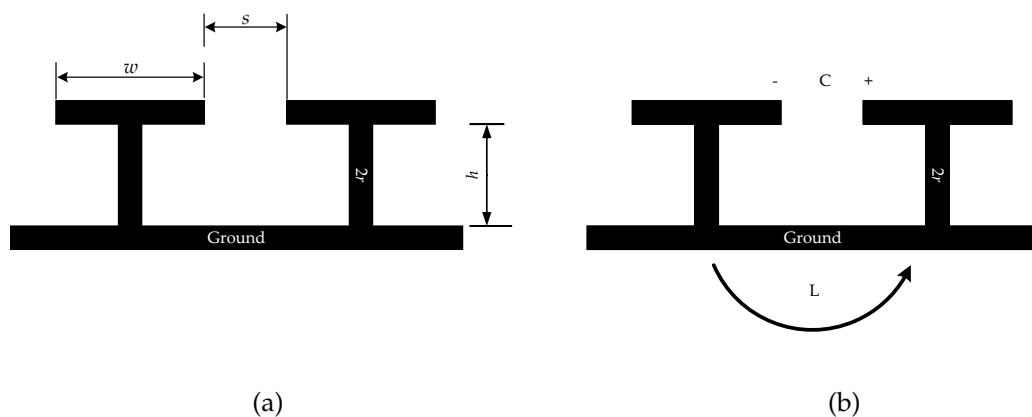


Figure 4.1: EBG structure (a) dimensions, (b) equivalent lumped LC model

In order to assess the importance of individual parameters on the resonant frequency of the structure, one dimension has been varied while the others remained unchanged. For instance, increasing the patch width,  $w$ , leads to

a larger capacitance,  $C$ , so that the resonant frequency and the bandwidth decreases.

Making the spacing between the patches,  $s$ , larger, decreases the capacitance,  $C$ . Thus, this results in an opposite trend to the previous scenario, and both the resonant frequency and the bandwidth increases.

Varying only the thickness of the EBG structure,  $h$ , results in an inversely proportional relationship between the bandwidth and the resonant frequency. Increasing the thickness will increase the inductance,  $L$ , therefore resonant frequency will decrease but the bandwidth will increase.

The relative permittivity  $\epsilon_r$  of the substrate is one of the effective parameters used to control the frequency behaviour of an EBG. The highest resonant frequency with the widest bandwidth is achieved when the substrate is air and it is clear that the capacitance associated with the higher permittivity lowers the resonant frequency and narrows the bandwidth at the same time [3, 7].

To achieve compactness, smaller and thinner EBG structures can be designed by choosing substrates with high dielectric constant ( $\epsilon_r$ ) values such as  $\text{TiO}_2$ .  $\text{TiO}_2$  is a substrate which in solid (bulk) form has a dielectric constant ( $\epsilon_r$ ) around 95 in UHF band [8].

In order to set the parameters to make the EBG structure resonate at a specific frequency, the required capacitance, inductance can be calculated with Equations 4.1, 4.2, 4.3 and the bandwidth by Equation 4.4 [3, 6, 7].

As shown in Equation 4.2, dielectric constant ( $\epsilon_r$ ) plays a significant role in the thickness parameter of an EBG.

Resonant frequency,

$$\omega_0 = \frac{1}{\sqrt{LC}}. \quad (4.1)$$

Capacitance,

$$C = \frac{w\epsilon_r(1 + \epsilon_r)}{\pi} \cosh^{-1} \frac{w + s}{s}. \quad (4.2)$$

Inductance,

$$L = \mu_0 \cdot h. \quad (4.3)$$

Bandwidth,

$$\frac{1}{\eta} \sqrt{\frac{L}{C}}. \quad (4.4)$$

### 4.3 Low Profile Antennas on EBG Structures

In wireless communications, to use antennas which have a low profile configuration is desirable. The challenge in low profile wire antenna design is the coupling effect of a nearby ground plane or surfaces such as body. This can be minimized by placing an EBG structure near to the antenna such as dipole.

### 4.4 Reflection Characterisation

In contrast to a perfect electric conductor, a magnetic conductor shows no phase shift on reflection. Reflection properties of the structure can be obtained by computing the phase of the reflection coefficient. A high impedance surface (HIS) acts as an artificial magnetic conductor, which exhibits zero reflection phase at one frequency. The resonant frequency at which zero reflection phase occurs, and the bandwidth (reflection phase is within  $\pm 90^\circ$ ) depends on the angle of incidence of the incident wave and also on the polarization of the wave (TE or TM). In this work the simulation tool CST microwave studio is used for reflection phase computation. The simulation model consists of a unit cell of the

structure, enclosed by an air box. To find the variation in the resonant frequency and bandwidth, with the variation in the incident angle, the simulation setup shown in Figure 4.2 was used.

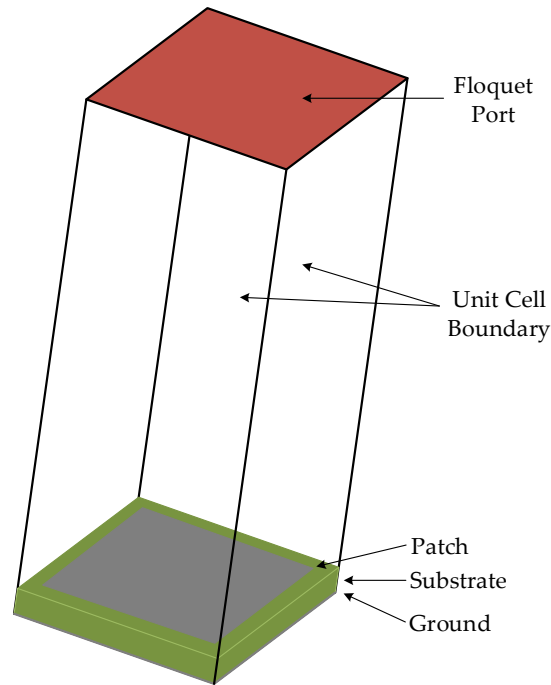


Figure 4.2: Simulated unit cell EBG structure.

A plane wave is incident on the unit cell from the (phase reference) excitation plane presented with a floquet port, as shown in Figure 4.2 which is at a distance of  $0.5\lambda$  from the unit cell. To avoid the effect of higher-order harmonics near the structure, the excitation plane must be at a distance greater than or equal to  $0.5\lambda$  from the top surface of the structure. Unit cell boundaries are used on the four side walls. The top is with open boundary, and the bottom is with electric boundary. The phase extracting plane and reflecting surface are at different locations. To restore the reflection phase exactly on the EBG structure, an ideal perfect electrical conductor (PEC) surface is used as a reference. The scattered fields from the PEC surface are also calculated. The PEC surface is located at the same height as the EBG top surface while the phase extracting plane location kept the same. The reflected phase from the HIS structure is normalized to

the reflected phase from the PEC surface using Equation 4.5. Therefore, the propagation phase from the distance between the reflecting surface and phase extracting plane is canceled out.

$$\text{Reflection Phase} = \theta_{EBG} - \theta_{PEC} + \pi \quad (4.5)$$

In Equation 4.5,  $\pi$  is added because the PEC surface has a reflection phase of  $\pi$  radians. Reflection phase plots extracted through this model with structural dimensions are given in Table 4.1. The reflection phase of an EBG crosses zero at one frequency as shown in Figure 4.3. The useful bandwidth of an EBG is in general defined as  $+90^\circ$  to  $-90^\circ$  on either side of the central frequency [9].

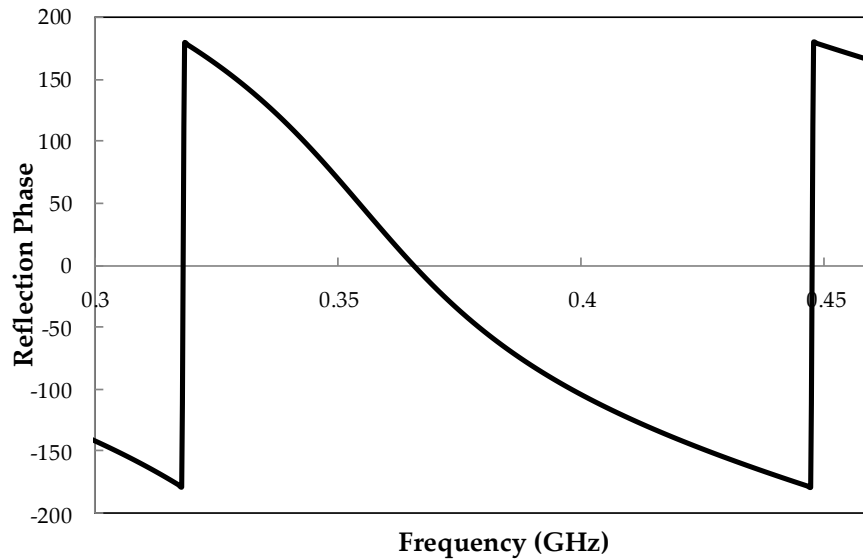


Figure 4.3: Reflection phase vs frequency plot of EBG structure.

## 4.5 400 MHz EBG Structure

A 400 MHz EBG structure was designed and simulated using CST Microwave Studio and a 400 MHz dipole antenna (simulated as a Mylar sheet antenna with a 37.5 cm length) was placed above the EBG structure with a 2

mm separation as shown in Figures 4.4(a) and (b). The EBG resonant frequency has been set to 400 MHz. The parameters and the dimensions are listed in Table 4.1 and the permittivity value was taken from [8].

Table 4.1: Dimensions of the EBG components.

Parameters	Symbol	Length
Patch Width	$w$	40 mm
Patch Length	$l$	40 mm
Substrate Thickness	$h$	3.1 mm
Antenna-EBG Separation	$d$	2 mm
Patch Separation Distance	$s$	4 mm

Substrate (relative permittivity),  $\epsilon_r = 95$

Via connections are omitted from this design because of the position of the dipole antenna above the surface means that field components parallel to the vias are not expected to be significant within the substrate [10].

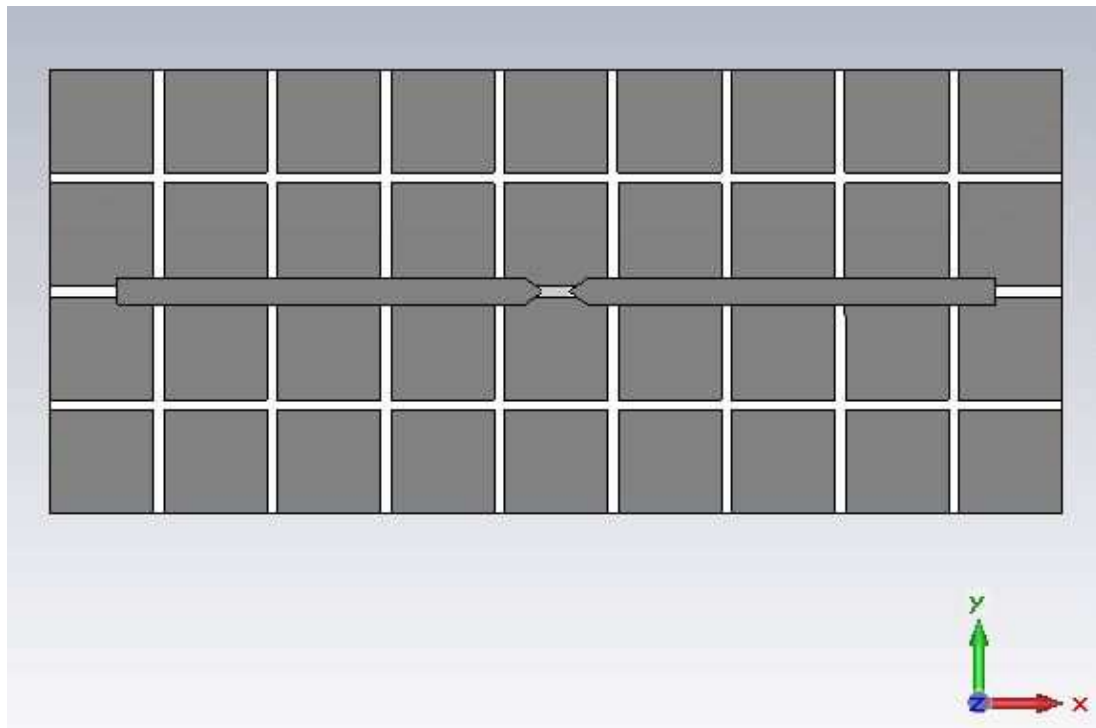
The simulated S-parameters of a (i) dipole in free space, (ii) above a conducting plane and (iii) above  $4 \times 9$  EBG structure are shown in Figure 4.5. The resonant frequency of the EBG structure is calculated by the Equation 4.1 to be 400 MHz.

When the dipole is positioned 2 mm above the ground plane, the return loss is very low. This is because of the conducting surface reflection coefficient has  $180^\circ$  reflection phase and the image current has an opposite direction to that of the original dipole. The reverse image current cancels the radiation of the dipole, resulting in a very poor return loss, Figure 4.5.

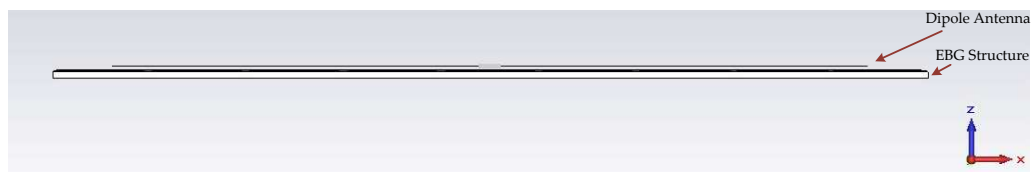
The -10 dB bandwidth of the dipole over the EBG was simulated to be 1.25% at 360 MHz. The bandwidth will always be narrow if a high permittivity substrate is used.

The 2D radiation pattern was also simulated and shown in Figure 4.6(a). The simulation has a good agreement with the expected results where the signal





(a)



(b)

Figure 4.4: EBG simulation structure (a) top-view (b) side-view

propagation in the  $-z$  direction is rejected by the EBG structure and the signal propagation takes place only in  $+z$  direction. The simulated antenna directivity is recorded as 4.14 dBi at the  $+z$  direction.

The volumetric radiation pattern radiation pattern of the dipole-EBG structure is illustrated in Figure 4.6(b) showing the strongest radiation in  $+z$  direction.

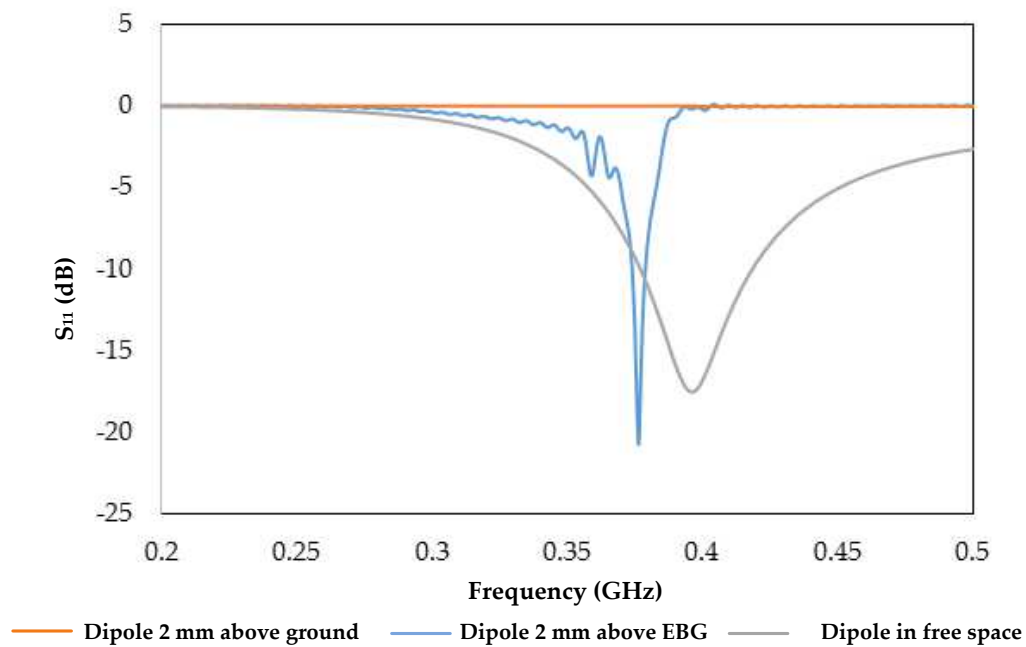
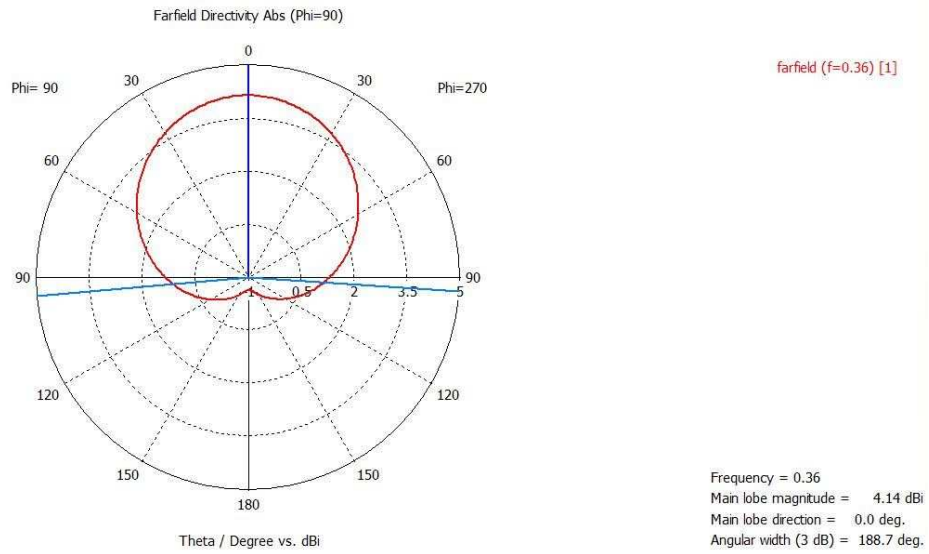


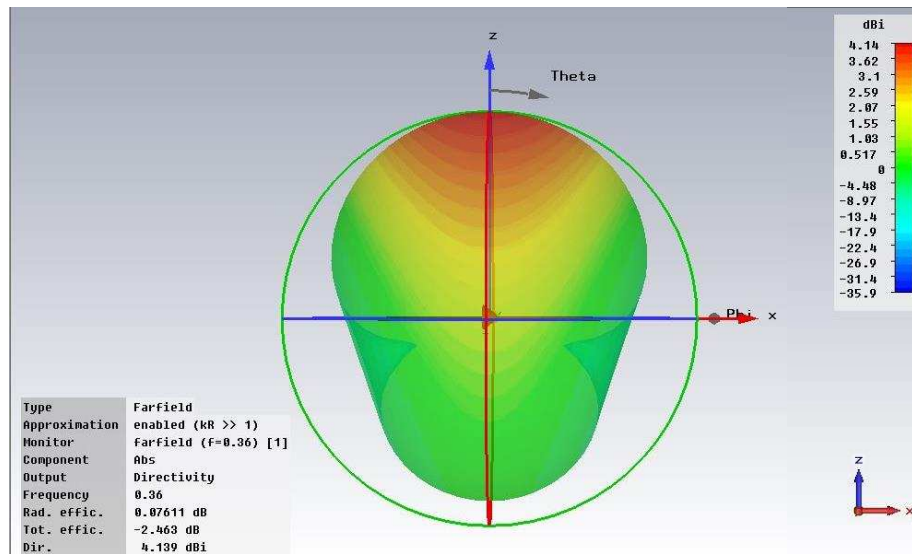
Figure 4.5: Simulated  $S_{11}$  parameters of a dipole on free space, on ground plane and on EBG.

## 4.6 Dielectric Constant Measurement

There are various ways to measure the dielectric properties of a material, such as the reflection, transmission, resonator and resonant-perturbation methods. These are classified as resonant and non-resonant. The material permittivity and permeability are extracted from the loaded resonant frequency and quality factor of a dielectric resonator in resonant methods. This method is suitable for low loss dielectric materials and has higher accuracy and sensitivity compared to non-resonant methods but the results are only available over a narrow band. Reflection and transmission methods are non-resonant. In the reflection method, the reflection from the sample is the key factor to extract the electrical characteristics. In the transmission/reflection method, transmission through the sample is also essential to derive the material properties. Various types of transmission lines can be used for the non-resonant method. In this research an E-band hollow waveguide transmission/reflection is used to perform the



(a)



(b)

Figure 4.6: Simulated EBG radiation patterns (a) Polar, (b) Volumetric (3D)

broadband, non-resonant method [4] This band is somewhat higher than the 400 MHz band of interest, but it will be seen that the extrapolation makes it possible to assess permittivity at high frequencies below the waveguide band. E-band measurement was used as 400 MHz waveguide was not available.

### 4.6.1 Waveguide Measurement Method

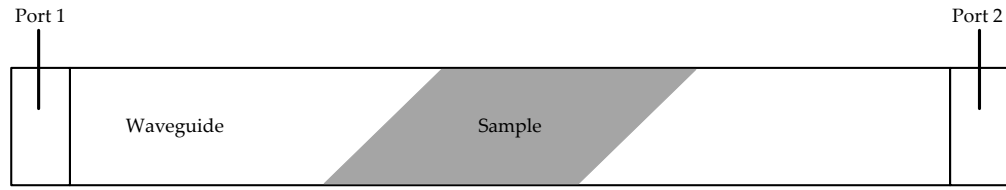
As mentioned, in order to determine the properties of the TiO<sub>2</sub> substrate at microwave frequencies, the waveguide transmission/reflection method was used. The substrate was shaped as shown in Figure 4.7 to create a physical symmetric interface between the ports. In order to support the TiO<sub>2</sub> powder sample under measurement, polystyrene foam pieces are used and accurately placed in the waveguide.

The faces of the sample were sloped as shown in Figure 4.7 to offer a more gradual transition at the sample interface and prevent large reflections occurring in the waveguide.

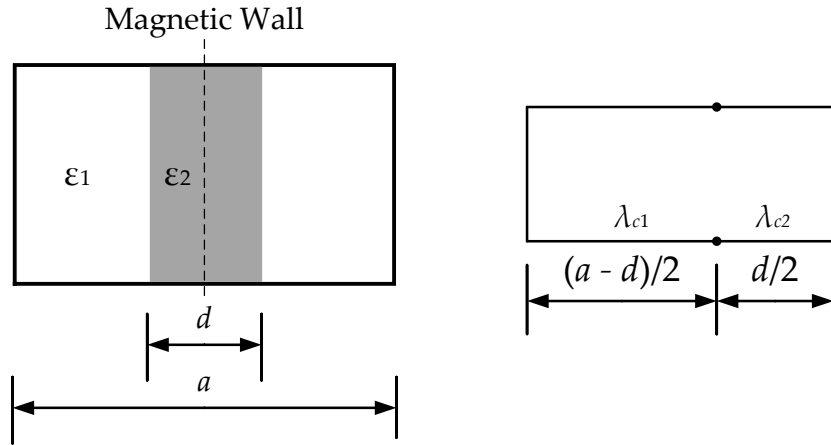
Very high permittivity substrates may have phase wrap problems over long electrical lengths and this has to be taken into account during the measurements by ensuring the sample is not several wavelengths long.

Measurements were carried out in three steps. First with the sample supported by the polystyrene foam, second with only the supporting polystyrene foam where the sample is replaced with a polystyrene block with the same dimensions and last as an empty waveguide. The obtained scattering parameters are used to determine the dielectric constant ( $\epsilon_r$ ) and the loss tangent ( $\tan \delta$ ). An advantage of this method, since it is based on comparison, is that any mismatch or inaccuracies in the measurements are removed by subtraction. Additionally, unlike the resonance method, the measurement can be performed over a wider band of frequencies between the cut-off frequencies of the TE<sub>10</sub> and TE<sub>01</sub> modes [11].

The cross section of the waveguide is shown in Figure 4.7(b), where  $a$  corresponds to the width of the waveguide, and  $\lambda_g$  is the wavelength of the propagation mode in the longitudinal direction. Therefore,  $\lambda_g$  represents the cut-off wavelength of the transverse guides.



(a)



(b)

Figure 4.7: Sample placed in a waveguide (a)side view, (b)equivalent network

At the interface in the transverse direction,

$$Y_1 = -jY_{01} \cot\left(\frac{\beta_1(d-a)}{2}\right) \quad \text{and} \quad Y_2 = -jY_{02} \cot\left(\frac{\beta_2 d}{2}\right). \quad (4.6)$$

where;

$$\beta_{1,2} = \frac{2\pi}{\lambda_1} \sqrt{1 - (\lambda_{1,2}/\lambda_g)^2} \quad , \quad \lambda_{1,2} = \lambda_0 / \sqrt{\epsilon_{1,2}}. \quad (4.7)$$

and  $\lambda_g$  is the cut-off wavelength of the guide with the dielectric.

The characteristic admittances  $Y_{01}$  and  $Y_{02}$  are given by:

$$Y_{01,02} = \frac{1}{\eta_{1,2}} \sqrt{1 - (\lambda_{1,2}/\lambda_g)^2}. \quad (4.8)$$

where,  $\eta_{1,2} = \sqrt{\mu_0/\epsilon_{1,2}}$ .

For propagation to be sustained, resonance must be achieved where  $Y_1 + Y_2 = 0$ . Substituting 4.7 and 4.8 into 4.6 obtains:

$$\frac{\sqrt{k^2\epsilon_r - \beta^2} \tan\left(d\sqrt{k^2\epsilon_r - \beta^2}/2\right)}{\sqrt{k^2 - \beta^2} \cot\left(a - d\sqrt{k^2 - \beta^2}/2\right)} = \quad (4.9)$$

where  $k$  is the propagation constant in medium 1,  $\beta = 2\pi/\lambda_g$  is the propagation constant in the guide with the dielectric and  $\epsilon_r = \epsilon_2/\epsilon_1$ . If either or both dielectric media are lossy, then  $\epsilon_1$  and/or  $\epsilon_2$  are complex and  $\beta$  in 4.9 is replaced by  $\gamma = \alpha + j\beta$ .

After placing the sample in an E-band waveguide, the amplitude and the phase of  $S_{21}$  with and without the sample are measured. The measured phases of  $S_{21}$  with and without the sample are  $\varphi_1$  and  $\varphi_2$ , respectively, where  $\varphi_1 > \varphi_2$  because of the dielectric. If the same lengths of waveguide and all the other components are used with and without the sample, then the difference between the two phase shifts will give us the extra phase due to the sample.

Thus  $\varphi_1 = \theta_1 + \theta_e$  and  $\varphi_2 = \theta_2 + \theta_e$ , where  $\theta_e$  is the phase shift because of the measurement components,  $\theta_1$  is the phase shift because of the dielectric sample and  $\theta_2$  is the phase shift of the length of waveguide where the sample was placed, but after it has been removed. The angles  $\theta_1$  and  $\theta_2$  are related to the guided wavelengths by  $\theta_1 = 2\pi l/\lambda_g$  and  $\theta_2 = 2\pi l/\lambda_{g0}$  and where  $\lambda_g$  and  $\lambda_{g0}$  are the guide wavelengths with and without the sample [11, 12].

## 4.7 Measurement Results

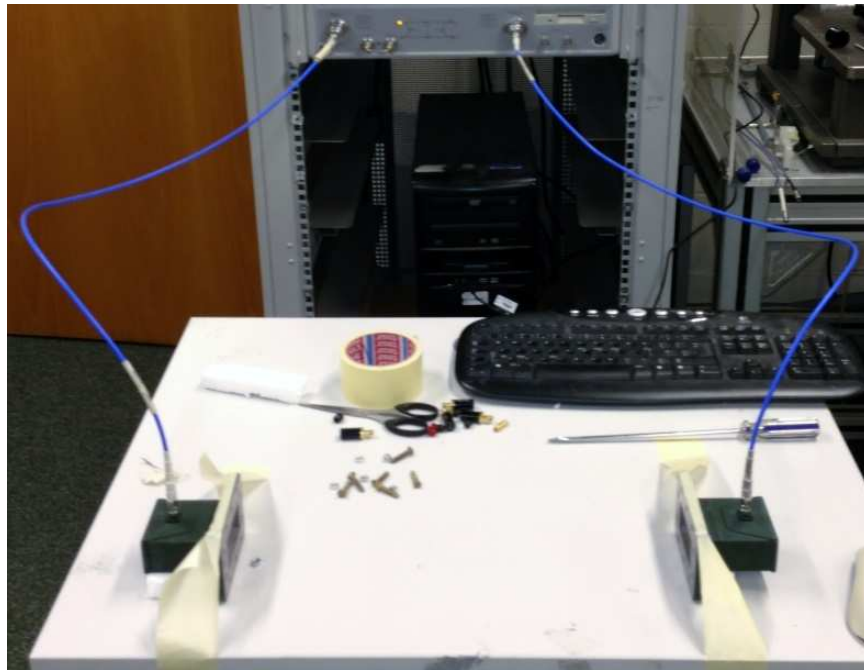
In this section, the waveguide measurement apparatus and the achieved measurement results with different materials are presented. As shown in Figure 4.8, the waveguide ports are connected to a network analyser to achieve scattering parameters in amplitude and phase. In order to eliminate the inaccuracies which may occur from cable displacement during sample insertion and removal, the cables are fixed and held in the same position until the measurements are completed.

The position of sample is adjusted in the centre of the waveguide.

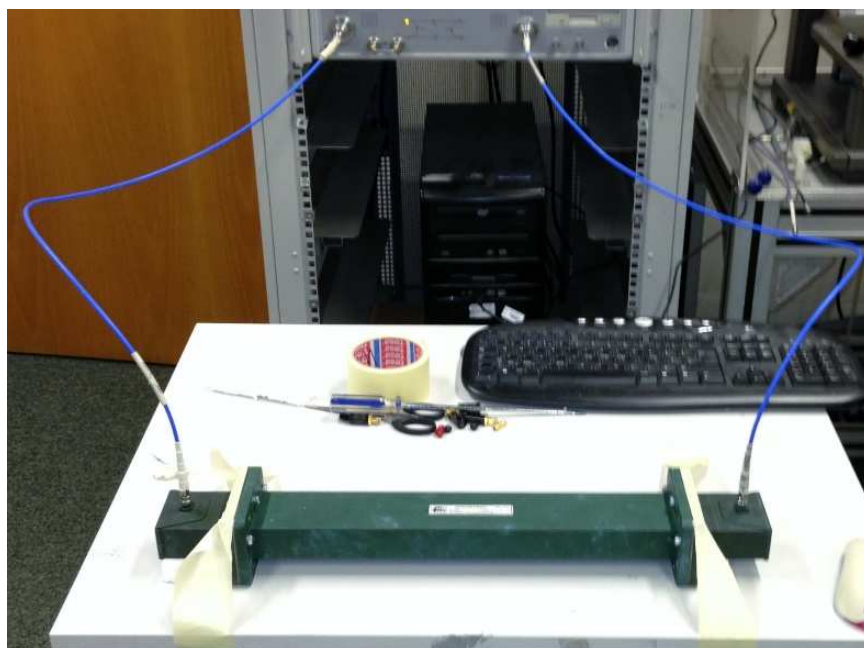
The measurement range was from 3.3 GHz to 4.9 GHz which corresponds to the waveguide operating frequency.

TiO<sub>2</sub> sample blocks were prepared with a support of polystyrene blocks on the sides and placed in the waveguide. By using a wooden block with an identical cross sectional dimensions of the sample block, powder is compressed until it becomes a solid block. There was no special compressing method used at this stage, all the compression is done by hand power.

In addition to the TiO<sub>2</sub> samples, Polydimethylsiloxane (PDMS) substrates were also assessed. PDMS substrate is a silicon based organic polymer, which can stretch and flex. During the the preparation period, loading it with the BaTiO<sub>3</sub> molecules increases its dielectric constant value depending on the loaded BaTiO<sub>3</sub> amount. In this project, PDMS samples are made by School of Physical Sciences at University of Kent to be used as a flexible and stretchable substrates and the electrical behaviour measurements are carried out by the waveguide method. The sample making process is explained in detail in Chapter 5. The dielectric constant values are extracted from the scattering parameter measurements. PTFE, wax, Polydimethylsiloxane (PDMS) with different Barium



(a)



(b)

Figure 4.8: Cable positions (a) without waveguide, (b) with waveguide

loading samples and  $\text{TiO}_2$  samples were measured. The results presented in Figure 4.9 show relative permittivity values of the different materials

After extracting the dielectric constant value from the measurements, loss



tangent ( $\tan \delta$ ) is also calculated. The measurement results for  $\tan \delta$  are presented in Table 4.2. The loss tangent values have also shown a good agreement with the expected results for wax and PTFE samples. The measurement results

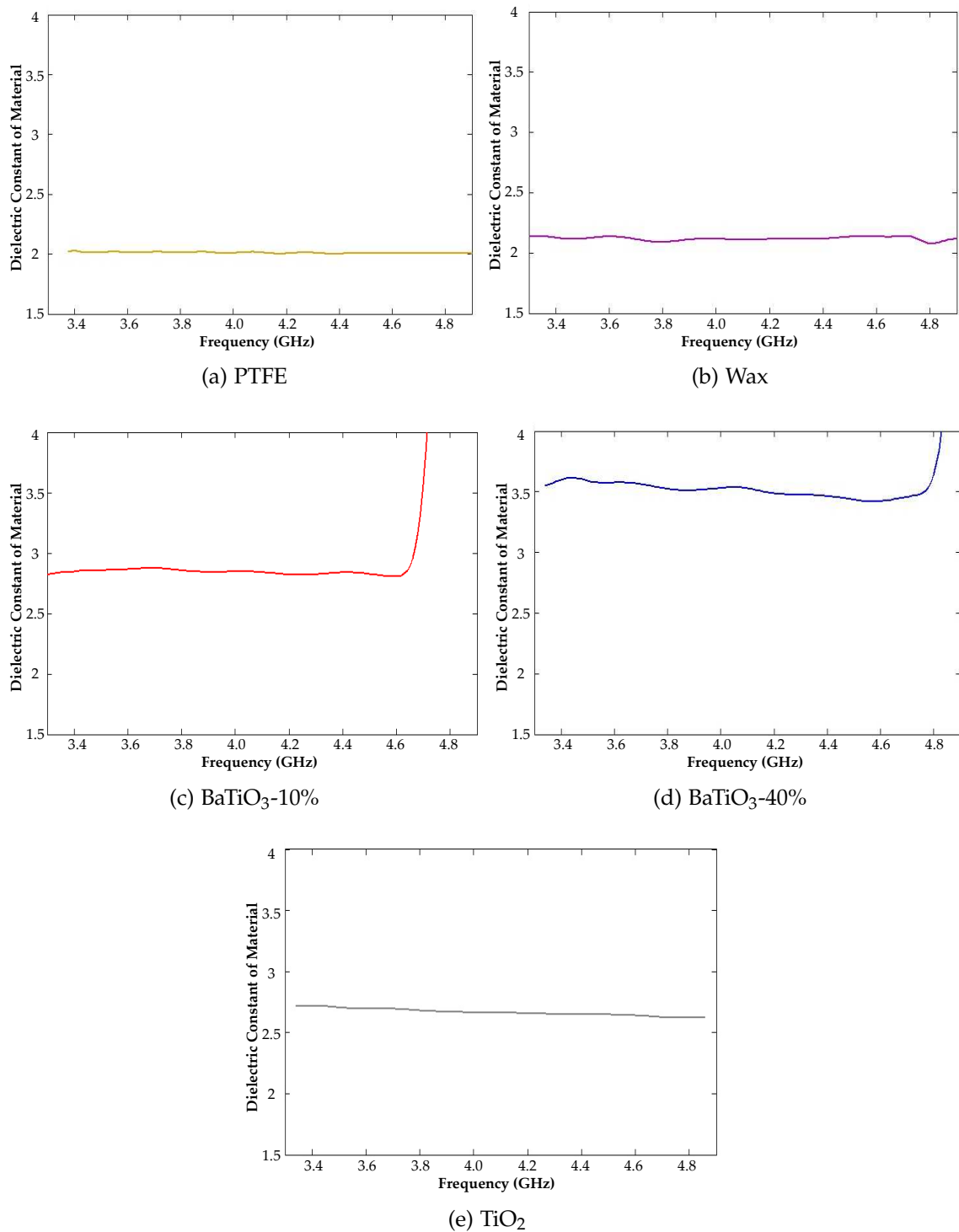


Figure 4.9: Dielectric constant values of different materials at E-band.

did not indicate any reliable  $\tan \delta$  value for  $\text{TiO}_2$ , an this issue needs to be investigated carefully to overcome this issue.

Table 4.2: Permittivity and loss tangent values of different substrates.

Material	Relative Permittivity ( $\epsilon_r$ )		Loss Tangent ( $\tan \delta$ )	
	Measured	Expected	Measured	Expected
Wax	2.1	2.1	$4 \times 10^{-4}$	$1.2 \times 10^{-4}$
PTFE	2.0	2.1	$5 \times 10^{-4}$	$2 \times 10^{-4}$
PDMS-BaTiO <sub>3</sub> 10%	2.9	3.0	$1.5 \times 10^{-3}$	-
PDMS-BaTiO <sub>3</sub> 40%	3.4	3.4	$3 \times 10^{-3}$	-
TiO <sub>2</sub>	2.5 - 2.7	95	-	$51 \times 10^{-3}$

## 4.8 Conclusions

Materials with high permittivities, such as  $\text{TiO}_2$ , are investigated to enhance the compactness of an EBG structure. The reliability of the waveguide dielectric constant measurement method for solid samples of different substrates were used in this chapter has been verified with measurement results in comparison with the published values for PTFE, wax and PDMS.

As  $\text{TiO}_2$  is a fine powder substrate, an additional compressing process was necessary to transform it into the solid. The powder  $\text{TiO}_2$  was compressed without any special technique. Therefore, the results indicate that the compression used was not sufficient and that special high compression equipment is needed to form a proper  $\text{TiO}_2$  solid by applying tonnes of pressure to it. The trapped air between the powder-particles significantly reduces the  $\epsilon_r$  and makes the compounded material frequency dependant with a dispersive behaviour. Only after applying sufficient pressure to the powder will lose its powder properties and it would cease to be a flexible substrate.

BaTiO<sub>3</sub> loaded PDMS substrate characteristics were measured. The physical and electrical characteristics indicated a potential use in the flexible and stretchable substrate and can be used in flexible EBG structure designs in the future.

The simulation of the structure with the expected value for high dielectric constant substrate (shown in Figure 4.2), TiO<sub>2</sub>, has exhibited that thinner structures could have designed compared to substrates with low dielectric constant. After calculating the suitable dimensions of EBG parameters, the structure has been simulated with a dipole antenna placed above it with a small separation. The simulation results have indicated a good match to the expected resonant frequency.

One of the challenges of using high permittivity substrates with thinner dimensions is that narrower bandwidths result. Simulated reflection phase and S-parameters have indicated a narrow bandwidth which would not be sufficient enough.

As a result of not achieving the expected dielectric constant results from the TiO<sub>2</sub> powder, prototyping of the EBG structure did not take place.

## References

- [1] S. Tse, B. Izquierdo, J. Batchelor, and R. Langley, "Convolute elements for electromagnetic band gap structures," in *Antennas and Propagation Society International Symposium, 2004. IEEE*, vol. 1, June 2004, pp. 819–822.
- [2] S. Zhu and R. Langley, "Dual-band wearable textile antenna on an EBG substrate," *Antennas and Propagation, IEEE Transactions on*, vol. 57, no. 4, pp. 926–935, April 2009.
- [3] F. Yang and Y. Rahmat-Samii, *Electromagnetic Band Gap Structures in Antenna Engineering*. Cambridge University Press, 2008.
- [4] L. Chen, C. Ong, C. Neo, V. Varadan, and V. Varadan, *Microwave Electronics: Measurement and Materials Characterization*. Wiley, 2004.
- [5] B. Sanz-Izquierdo, E. Parker, J. Batchelor, and J. Miller, "Body armour with integral high impedance surface," in *Antennas and Propagation (EUCAP), Proceedings of the 5th European Conference on*, April 2011, pp. 1061–1064.
- [6] M. Md Tan, T. Rahman, S. Rahim, M. Ali, and M. Jamlos, "Antenna array enhancement using mushroom-like electromagnetic band gap (EBG)," in *Antennas and Propagation (EuCAP), 2010 Proceedings of the Fourth European Conference on*, April 2010, pp. 1–5.
- [7] N. Engheta and R. Ziolkowski, *Metamaterials: Physics and Engineering Explorations*. Wiley, 2006.
- [8] L. Solymar and D. Walsh, *Electrical Properties of Materials*. OUP Oxford, 2009.
- [9] D. Sievenpiper, L. Zhang, R. Broas, N. Alexopolous, and E. Yablonovitch, "High-impedance electromagnetic surfaces with a forbidden frequency

- band," *Microwave Theory and Techniques, IEEE Transactions on*, vol. 47, no. 11, pp. 2059–2074, Nov 1999.
- [10] O. Luukkonen, A. Yakovlev, C. Simovski, and S. Tretyakov, "Comparative study of surface waves on high-impedance surfaces with and without vias," in *Antennas and Propagation Society International Symposium, 2008. AP-S 2008. IEEE*, July 2008, pp. 1–4.
- [11] B. Sanz-Izquierdo, J. Batchelor, and M. Sobhy, "Button antenna on textiles for wireless local area network on body applications," *Microwaves, Antennas Propagation, IET*, vol. 4, no. 11, pp. 1980–1987, November 2010.
- [12] N. Marcuvitz, *Waveguide Handbook*. P. Peregrinus, 1951.

# CHAPTER 5

## EPIDERMAL PASSIVE RFID STRAIN SENSOR FOR ASSISTED TECHNOLOGIES

\* \* \*

An epidermal passive wireless strain sensor using RFID tags is presented. The tag is intended to detect eyebrow or neck skin stretch where paraplegic patients have the capability to tweak facial muscles. The tag design is designed on Barium Titanate loaded PDMS material and assessed to demonstrate strain gauge sensitivity and repeatability as a function of skin stretch.

## 5.1 Introduction

RFID is becoming a pervasive technology used in a wide range of applications, such as logistics or inventory management. Furthermore, in addition to distributed sensor networks [1–3], mobile healthcare [4], homeland and personal security, it also has potential use for assisted living and rehabilitation systems for disabled people. In applications such as powered wheelchair control for rehabilitation and assisted living, the navigation and control systems needs to be effective in real-time and offer users reassuring robust support, especially in collision avoidance. It is important that assistive technology systems incorporate a degree of intelligence, and must be sufficiently dynamic to recognize and accommodate for patients providing inputs of varying accuracy. Robotic assistance employed in the healthcare arena must therefore emphasize positive support rather than adopting an intrusive or over-supportive role [5], especially in rehabilitation scenarios where patients should be encouraged to gain increased independence as they learn to manage a condition as their needs change with time. This issue is the subject of SYSIASS, a European Commission funded project where autonomous powered wheelchair technology is supported by sensors to prevent collisions with door frames, static objects, and people.

UHF RFID is proposed in this chapter as an enabling technology for skin strain sensors to detect muscle twitches in the face and neck for severely incapacitated wheel chair users.

An epidermal tag design is developed here from an RFID tattoo transfer [6, 7] and is investigated for stretch detection on skin for the first time. The strain sensor can be attached above the eyebrows or around neck as shown in Figure 5.1 and 5.2, where many paraplegic patients have movement capability. The skin stretch associated with facial muscle tweak leads to tag geometry distortion and this is detected as a function of backscattered power. When combined with

a proximal wheelchair mounted read antenna, this provides an opportunity to monitor the amount and direction of the movement and therefore control a wheelchair with respect to skin stretch.

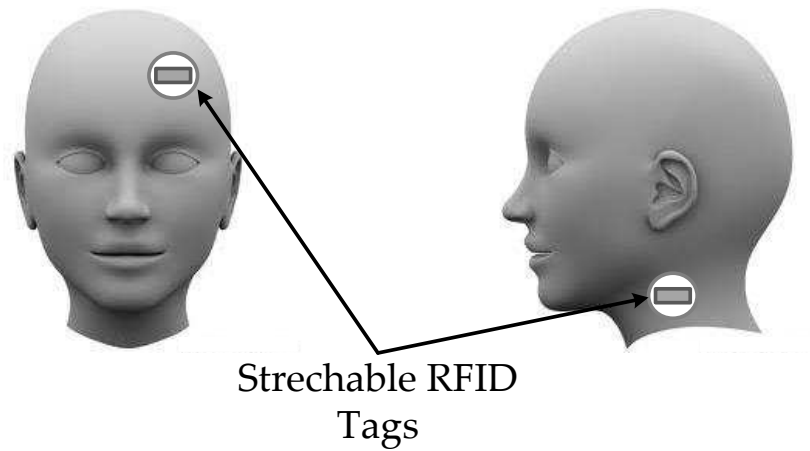


Figure 5.1: Concept tag positions on the head.

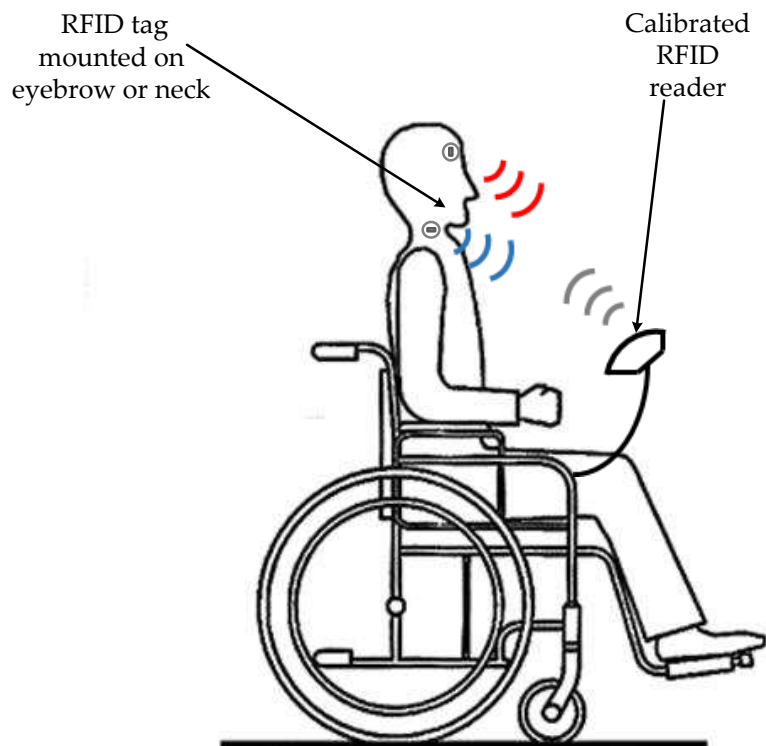


Figure 5.2: Reader antenna concept for strain sensor tags.



## 5.2 Strain Gauge RFID Tag

Owing to the high permittivity and high loss tangent of skin and muscle tissues [7], the design of efficient RFID tags on, or close to, skin is highly challenging. In addition to this, the dielectric properties of tissue vary according to location on the body and also between individuals. Very low profile skin mounted UHF RFID tags have poor radiation efficiency and it is important to obtain as high a value of impedance matching coefficient as possible if read ranges of more than a few cm are to be achieved. The new tag design arising from the tattoo tag.

The passive UHF RFID tattoo tags in [7, 8] were designed for inkjet printing onto transfer paper and to withstand ordinary skin flexing. However, the conducting ink would be cracked by significant stretch and such tags would not therefore be suitable for strain gauge design.

To address this challenge, a design is described using elastic conducting fabric on a substrate of Polydimethylsiloxane (PDMS) loaded with Barium Titanate ( $\text{BaTiO}_3$ ). This material was selected to obtain a low-profile elastic structure with a permittivity value significantly above free space. The loading of the PDMS with  $\text{BaTiO}_3$ , can be adjusted to control the fundamental  $\epsilon_r$  value. In addition it has low chemical reactivity, it is non-toxic, making it well suited for epidermal application [9]. Loaded PDMS structures were described in [10] to create flexible tags, but here the aim is to create a tag where the entire structure including the conductor can stretch.

## 5.2.1 Strain Gauge Sensor Concept

In this section, the preliminary CST design of the strain gauge sensor is presented with the potential geometrical deformation due to strains on the  $x$  and  $y$  axis.

The sensor is chosen to be a circular shape in order to enable equal deformation due to strain in  $x$  and  $y$  dimensions where  $z$  is normal to the skin surface. The preliminary design is a basic slot antenna with a  $50\Omega$  feed. The simulation results consist of the impedance match quality at the resonant frequency which shows a relationship with the amount of stretch.

### 5.2.1.1 Single Port Slot Stretchable Antenna Sensor

The simulated antenna in this research is a basic slot antenna designed for the wireless Local Area Network (LAN) band when not stretched. As shown in Figure 5.3, the single port slot antenna design consists of a ground plane, a silicone substrate and a rectangular slot on the top plate with the dimensions shown in Table 5.1. The resonant frequency of 2.45 GHz is obtained for a permittivity of 3.2 and 0.025 for the loss tangent of silicone [11].

Figures 5.4 and 5.5 illustrate how the slot dimensions are distorted with stretching, namely the slot length will increase for a longitudinal strain, while the slot width will decrease. The dimensions of the disc shaped structure change relative to the stretching either on  $x$  or  $y$  Axis.

Table 5.1: Dimensions of single port stretchable slot antenna.

Radius x-axis (mm)	Radius y-axis (mm)	Substrate Thickness (mm)	Slot Width (mm)	Slot Length (mm)
18	18	0.485	2.4	10.3

A stretch along the  $x$ -axis, transforms the patch into an elliptical structure with the major axis aligned horizontally and the slot becomes longer and thinner, where the change in dimensions of the slot is directly proportional to the stretching factor as shown in Figure 5.4. The substrate gets thinner (in the  $z$ -axis), while becoming longer in the  $x$ -axis and narrower on the  $y$ -axis. Therefore the volume of the substrate is kept the same.

A stretch in the  $y$ -axis converts the patch into an elliptical structure with the major axis in the vertical direction. The slot becomes shorter and wider, Figure 5.5. Again, the change in dimensions of the slot is directly proportional to the stretching factor. The substrate gets thinner and narrower in the  $x$ -axis and longer in the  $y$ -axis; and the volume of the substrate again remains constant.

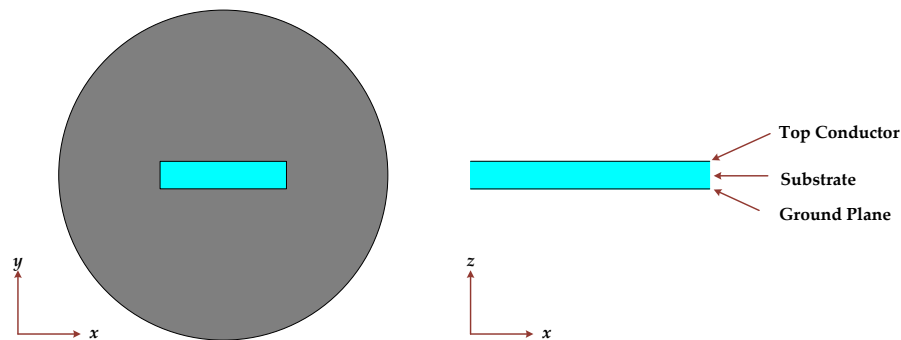


Figure 5.3: Geometry of the one slot stretchable antenna.

### 5.2.1.2 Two Port Slot Stretchable Antenna Sensor

To make the structure sensitive to strain in more than one axis, two slotted structure was designed. As shown in Figure 5.6, in this case, an additional slot is placed onto the  $y$ -axis compared to the single port antenna in order to distinguish the stretching direction. The slots are intended to behave with independent responses according to the vector direction of strain aligned with each slot.

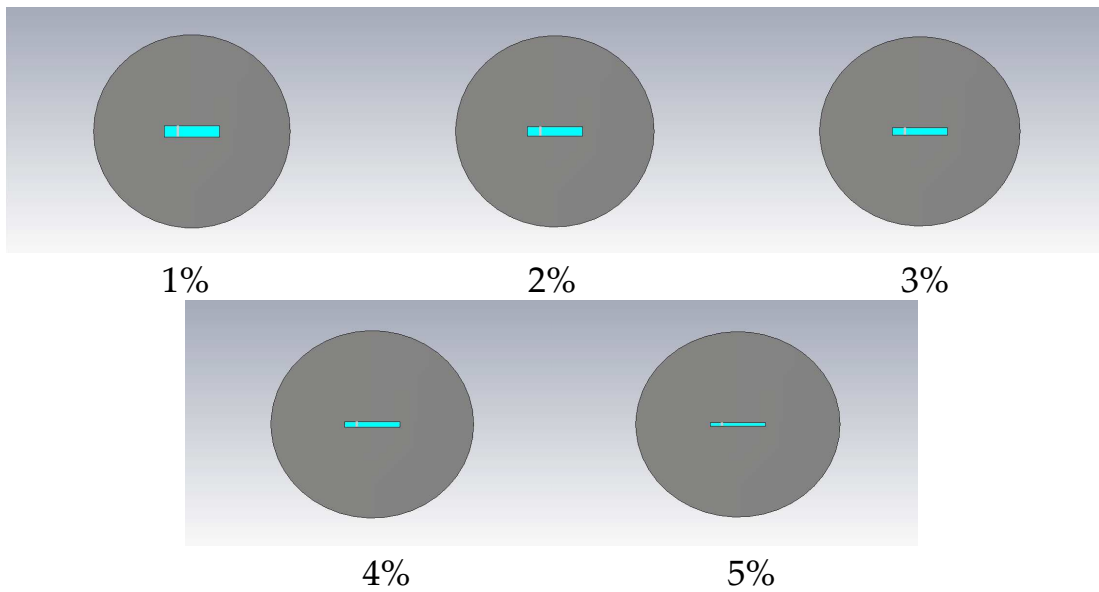


Figure 5.4:  $x$ -axis stretching effect on the structure.

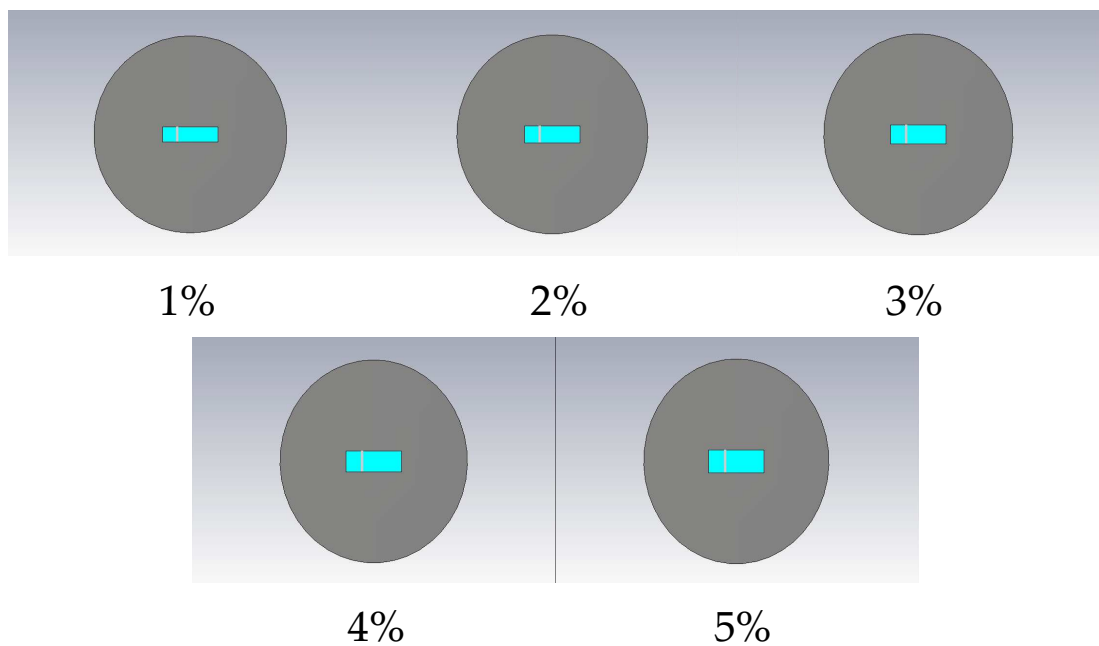


Figure 5.5:  $y$ -axis stretching effect on the structure.

As shown in Figure 5.7, 5.8 and 5.9, stretch on the  $x$ -axis converts the shape into a horizontally aligned elliptical structure and makes the horizontal slot longer and narrower. Simultaneously, the vertical slot distorts oppositely, becoming shorter and wider.

Stretch on the  $y$ -axis, converts the shape into a vertical elliptical structure

making the horizontal slot shorter and wider, while the vertical slot gets longer and narrower.

Strains applied at some intermediate angle between the  $x$  and  $y$ -axes will convert the shape into an elliptical structure with the major axis along the direction of the strain and making both the horizontal and the vertical slots longer and narrower.

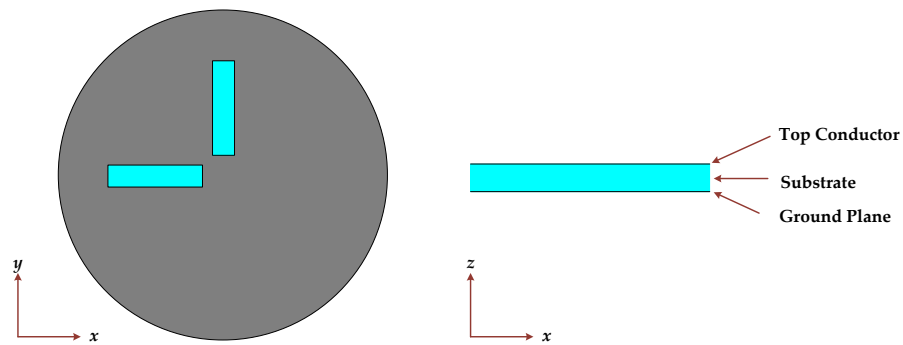


Figure 5.6: Geometry of the two slot stretchable antenna.

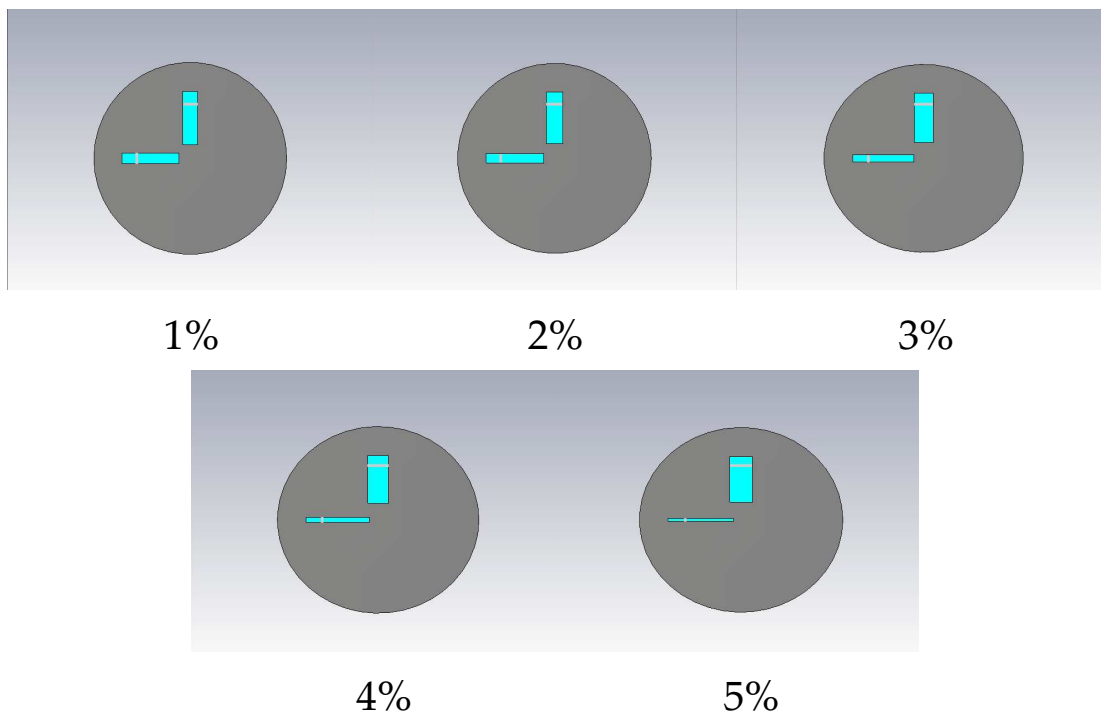


Figure 5.7:  $x$ -axis stretching effect on the two port structure.

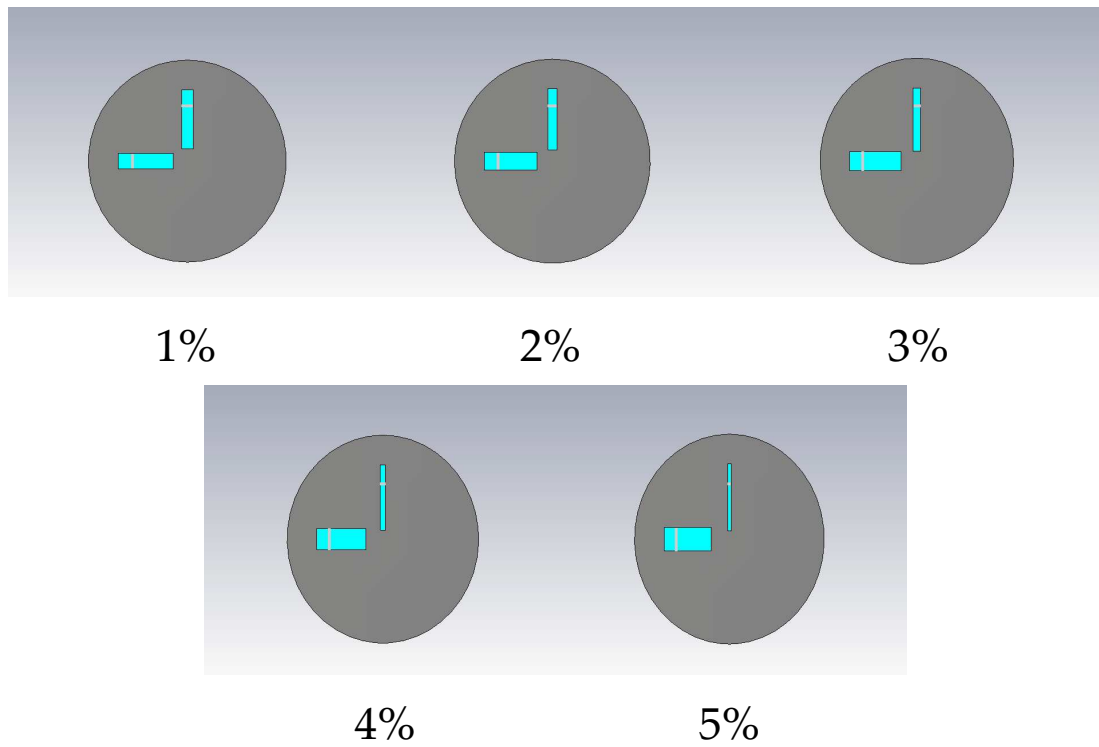


Figure 5.8:  $y$ -axis stretching effect on the two port structure.

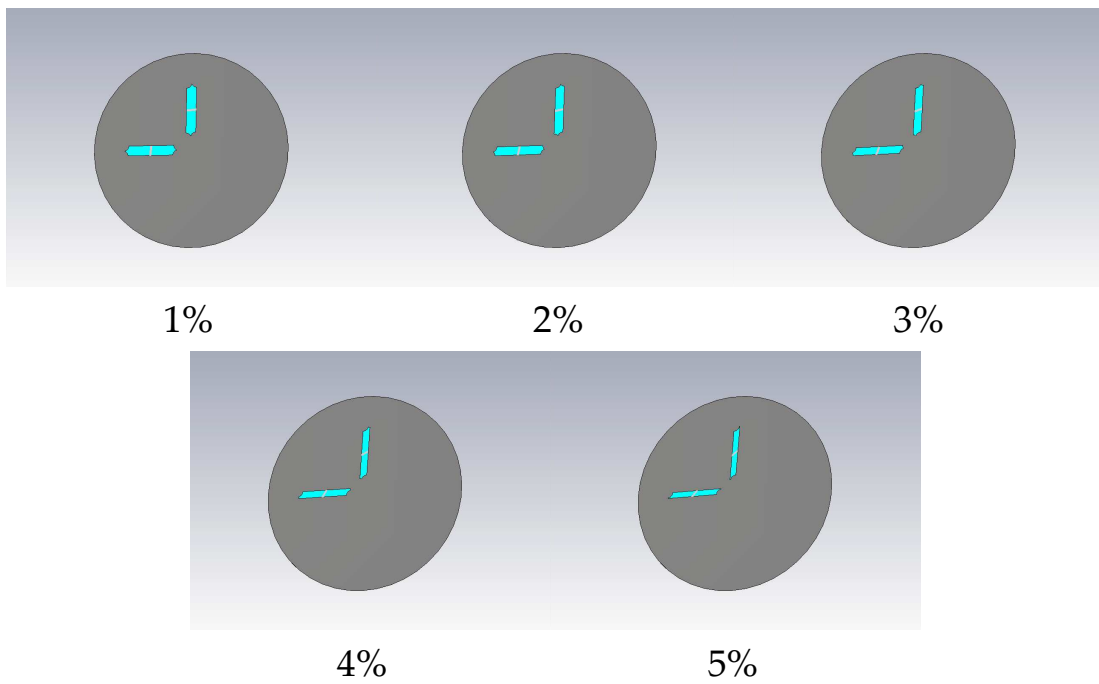


Figure 5.9: Simultaneous  $x$  and  $y$ -axis stretching effect on the two port structure.

### 5.2.1.3 Simulation Results

Both single slot and two slot stretchable sensor structures have been simulated, resonant frequency and  $S_{11}$  amplitudes are presented and discussed.

The operating frequency of a resonant slot antenna is directly proportional to slot length which is half a wavelength. Depending on the stretch direction, the slot gets either longer or shorter and therefore the resonant frequency changes in proportion to stretch factor. A change in the width of the slot affects the impedance match quality. Figure 5.10(a) and 5.10(b) present the resonant frequency behaviour and the impedance match quality with the amount of stretch.

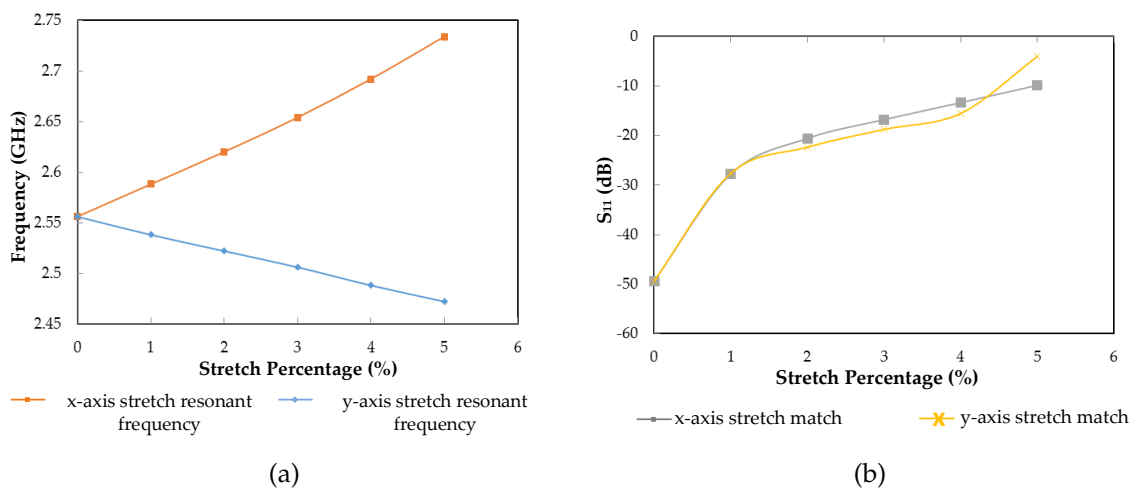


Figure 5.10: Single port slot structure simulation results (a) Resonant frequency vs. Stretch factor and (b)  $S_{11}$  vs. Stretch factor.

According to Figure 5.10(b), the  $S_{11}$  magnitude curves are very similar for both  $x$  and  $y$  axis stretching. This is due to alterations in  $S_{11}$  according to frequency detuning as the slot length changes and also to an additional mismatch as the slot width changes. Therefore, the parameter  $\Psi$  is defined which is directly related to antenna impedance and can be regarded as the sensor transfer response [12]. The  $\Psi$  calculation is defined later in this chapter.

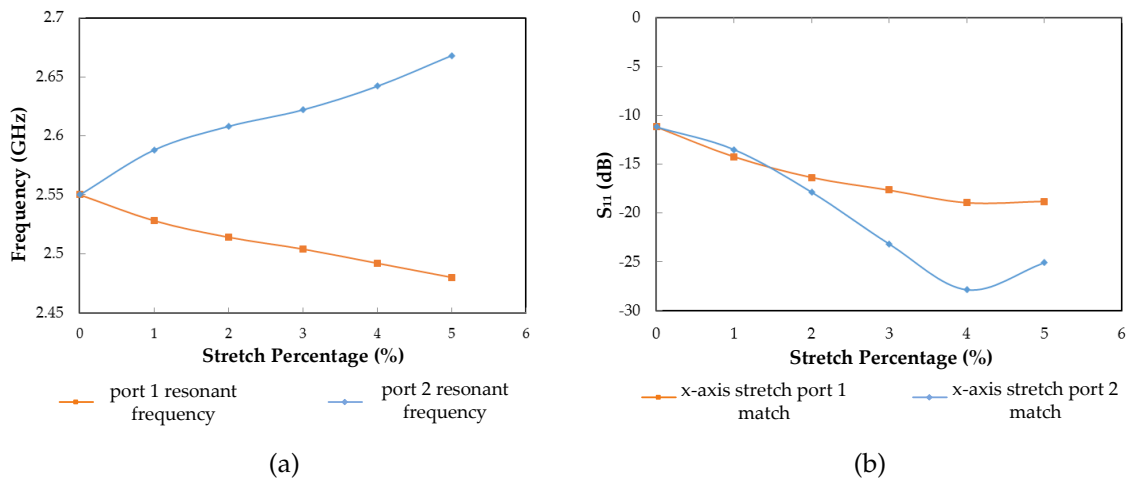


Figure 5.11: Two port slot structure  $x$  - axis stretch simulation results. (a) resonant frequency vs. stretch factor comparison of ports and (b)  $S_{11}$  vs. stretch factor comparison of ports.

The two slots are close and their impedance match is affected by mutual coupling as indicated by the S-parameters in Figure 5.12. In this case, in the instance of zero stretch, the slots do not match perfectly due to the coupling. As shown in Figure 5.11(b) and Figure 5.13(b), when the geometry of the structure changes due to stretching, the mutual coupling decreases and both slots start to match better.

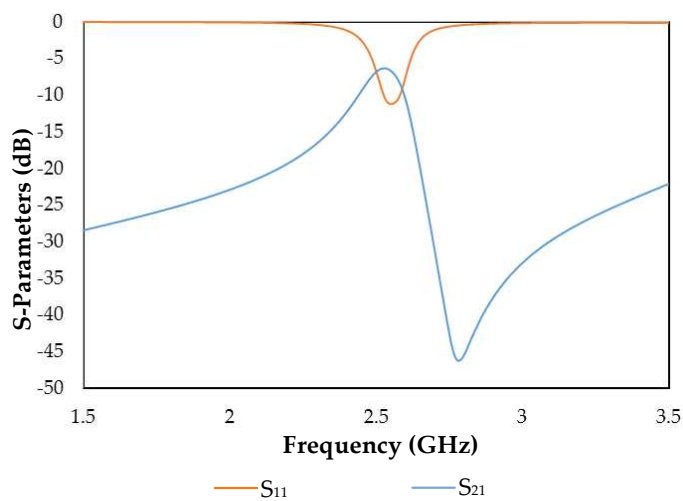


Figure 5.12: Two slots zero stretch  $S_{11}$  and  $S_{21}$  plots.



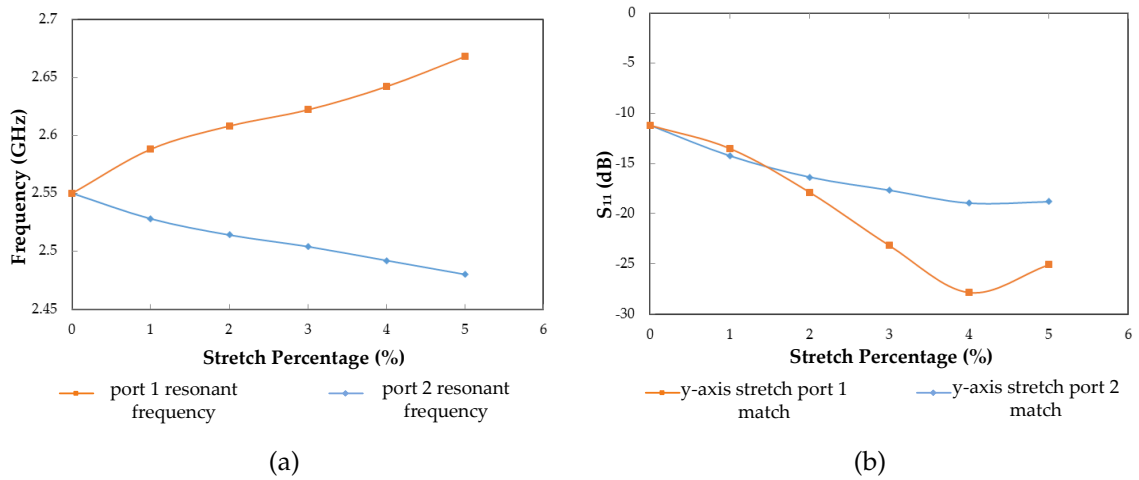


Figure 5.13: Two port slot structure  $y$  - axis stretch simulation results (a) resonant frequency vs. stretch factor comparison of ports and (b)  $S_{11}$  vs. stretch factor comparison of ports.

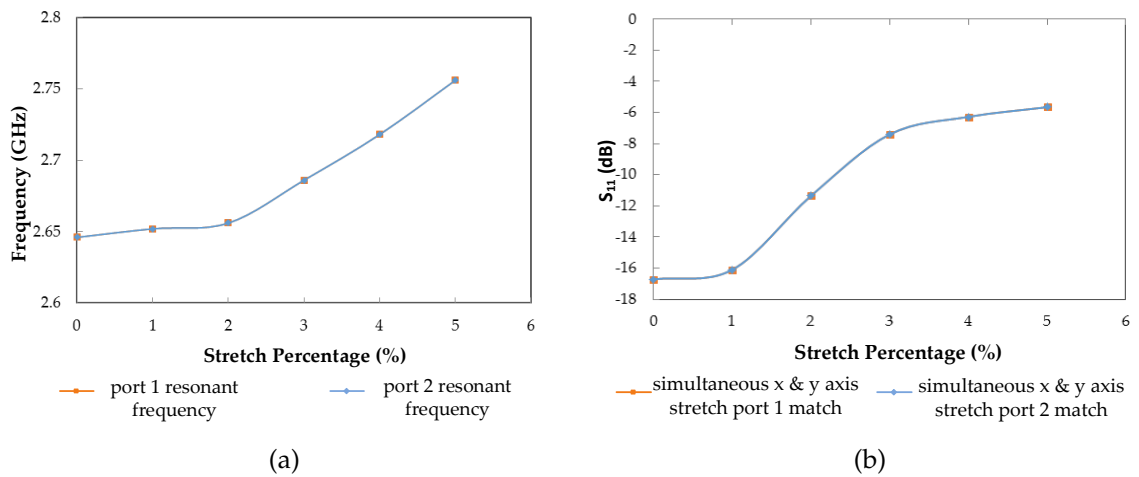


Figure 5.14: Simultaneous two port  $x$  and  $y$ - axis stretch simulation results (a) resonant frequency vs. stretch factor comparison of ports and (b)  $S_{11}$  vs. Stretch factor comparison of ports

When the strain is on the  $x$  and  $y$  axis at the same time, change in terms of slots will be symmetrical, thus the matching quality and the resonant frequency behaviours will be identical for each port as shown in Figure 5.14(a) and also in 5.14(b).

The extent of the mismatch for each slot can be detected at the reader and the resultant direction and magnitude of the straining force can be deduced. As

stated above, calculating  $\Psi$  would allow the reader to distinguish strain between  $x$  and  $y$  axis.  $\Psi$  can be explained as the indication factor of any physical or geometrical feature of the target that is subjected to change in the phenomenon monitored by the RFID platform.

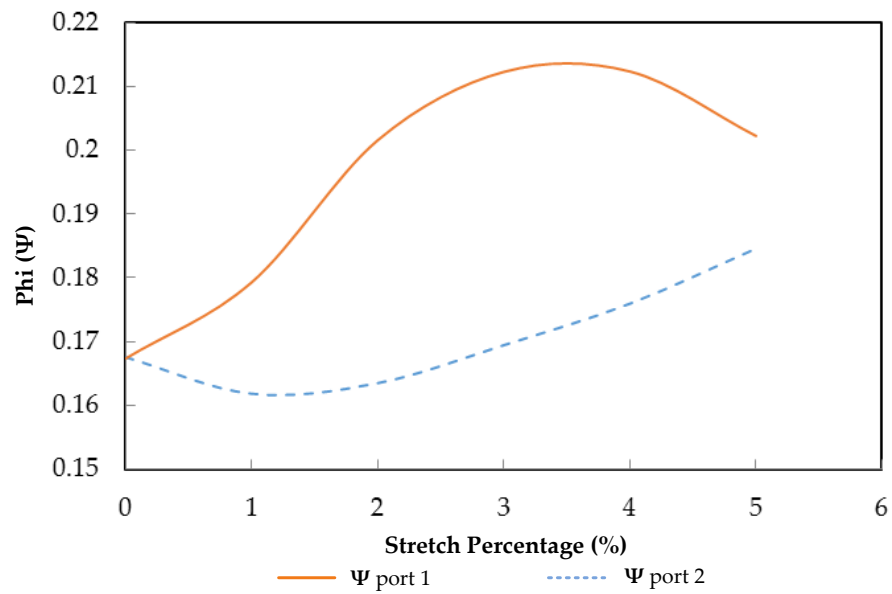
If the RFID antenna is connected to an RFID chip, as shown in Equation 5.1,  $\Psi$  depends only on the antenna's terminal impedance and the RFID transponder chip impedance. Both real and imaginary parts of the impedance values must be matched. The analogue identifier is a function of the  $\Psi$  parameter and is defined in [13] as:

$$AID[\Psi] = \frac{R_C}{|Z_A[\Psi] + Z_C|} \quad (5.1)$$

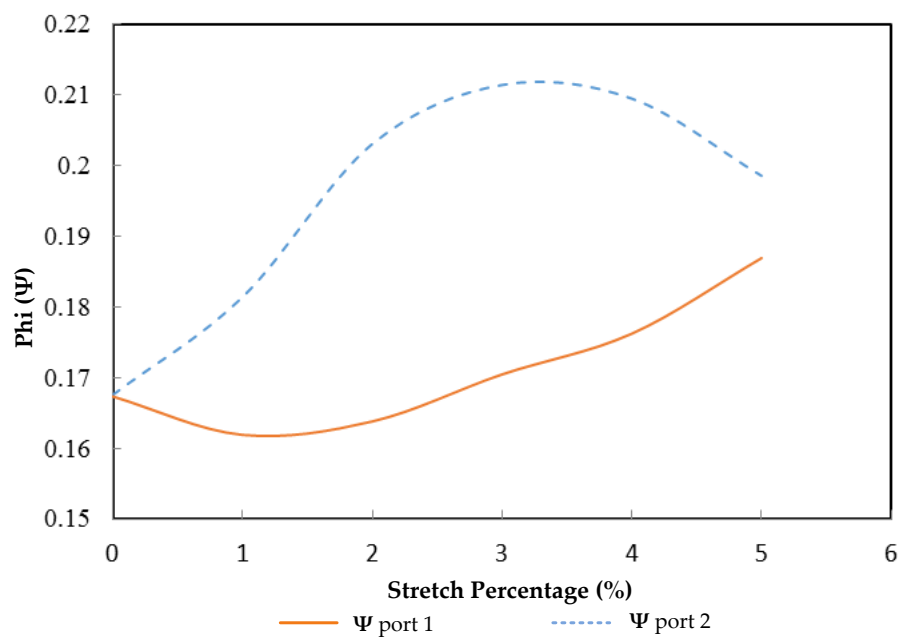
where  $Z_A = R_A + jX_A$  and  $Z_C = R_C + jX_C$  are the input impedance of the tag antenna and microchip where,  $Z_C = 20 - j125 \Omega$ .

In Figures 5.15 (a) and (b),  $\Psi$  is plotted for both slots on the  $x$  and  $y$  axes. The slots' resonances are different from each other with the stretching effect, and their  $\Psi$  curves are dissimilar allowing the responses to be differentiated for  $x$  and  $y$  axes applied strains.

When the slots are placed orthogonal to each other without modifying the single slot dimensions, there is mutually coupling at the "unstretched" state as shown in Figure 5.12. It is noted that the best match occurs at 3.5% strain and there is a turning point, though the slot dimensions could be modified to find best dimensions to reduce coupling. When stretched, the individual slot impedances of port 1 and port 2 differ from each because of the slot geometry deformations orthogonal to each other. Therefore, as the slot impedances change, each slot will have a unique  $\Psi$  value and they will be able to be uniquely identified by their different RFID chips.



(a)



(b)

Figure 5.15: Two port slot structure (a) x-Axis Phi, (b) y-Axis Phi calculation results.

## 5.2.2 Elastic PDMS Substrate Formation

To create a suitable elastic substrate, PDMS elastomers were formed using viscous linear PDMS, liquid cross-linker and a catalyst. Mechanical properties, such as elasticity are easily modulated by varying the cross-linker density i.e. the molecular weight of the linear PDMS and cross-linker concentration. BaTiO<sub>3</sub> is a ferroelectric ceramic powder, with high relative permittivity values up to 4000 at room temperature [14]. As well as frequency, the permittivity of BaTiO<sub>3</sub> is dependent on its crystalline phase, temperature, dopants and importantly, the synthesis method which includes purity, density and grain size [9].

The substrates were fabricated by mixing BaTiO<sub>3</sub> and PDMS before cross-linking occurred using tetraethyl orthosilicate (TEOS) via a Sn (II) catalysed condensation reaction. The permittivity value of the substrates was controlled by varying the weight percentage of BaTiO<sub>3</sub> as shown in Figure 5.16. Substrates with 40 wt% BaTiO<sub>3</sub> loading showed the desired relative permittivity value,  $\epsilon_r = 3.43$ . As mentioned earlier on Section 5.2.1.1, the preliminary simulations were based on a silicone substrate with a dielectric constant of 3.2. The aim was to set the barium loaded PDMS dielectric constant close to this value.

Hence, substrates were synthesised from PDMS with 40 wt% BaTiO<sub>3</sub>. Silanol-terminated polydimethylsiloxane cSt 18000 (DMS-S42) (M.W. 77,000, Fluorochem Ltd.), tin (II) 2-ethylhexanoate (95%, Sigma Aldrich), toluene (analytical reagent grade, Fisher Chemicals) barium titanate ( $< 2\mu\text{m}$  99.9% trace metal basis, Sigma Aldrich) and tetraethyl orthosilicate (99%, Sigma Aldrich) were used as received. Homogenous mixing of elastomer components was achieved using a RCT basic IKA labortechnik speed-mixer.

Silanol-terminated PDMS (12g, 0.156 mmol), BaTiO<sub>3</sub> (4.8g, 20.5 mmol), tetraethyl orthosilicate (0.070 cm<sup>3</sup>, 0.336 mmol) and toluene (3.47 cm<sup>3</sup>, 35.6 mmol) were added to a glass beaker and speed-mixed for 30 minutes. Tin (II) 2-ethylhexanoate

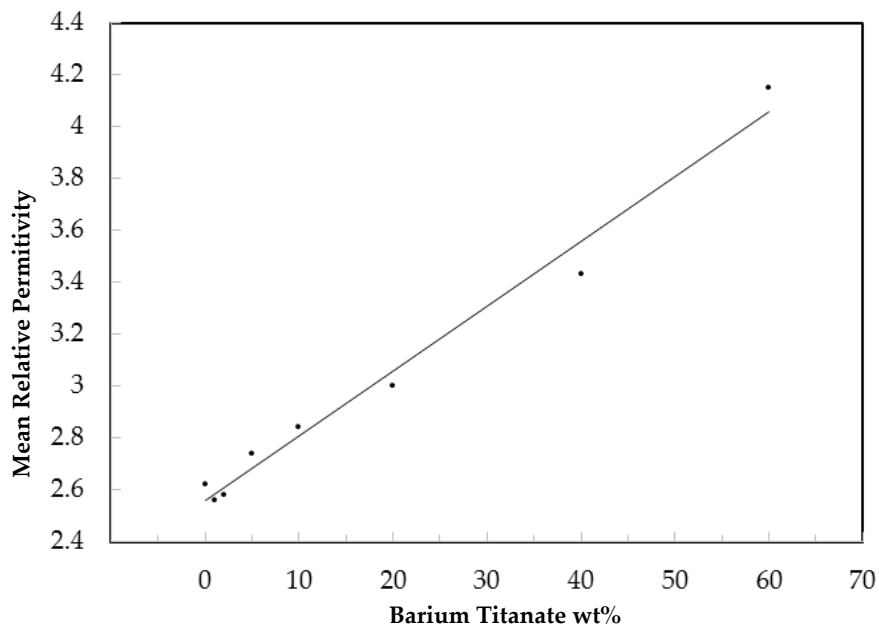


Figure 5.16: Measured relative permittivity of Barium Titanate-PDMS composites (3GHz) in a waveguide.

dissolved in toluene ( $0.074 \text{ cm}^3$ ,  $0.148 \text{ mmol}$ ) was then added to the mixture and speed-mixed for 60 seconds before being poured into the circular mold. A flexible filling knife was drawn down over a PTFE circular mold (diameter = 80 mm, height = 1 mm) to ensure a uniform height elastomer. The elastomer was allowed to cure at room temperature for 2 hours and was placed into an oven at  $60^\circ\text{C}$  for 72 hours. The resulting substrates were stretchable, soft, flexible and water resistant.

Convenient epidermal mounting facilitating low-profile tag with geometry with dimensions is shown in Figure 5.17 with the principal dimensions listed in Table 5.2. The tag conductor was simulated in CST Microwave Studio on a polymer sheet ( $\epsilon_r = 3$ ) attached to the loaded PDMS substrate with  $\epsilon_r = 3.43$ . To represent human tissue, a stratified rectangular phantom was used with  $154 \times 160 \text{ mm}^2$  upper surface area and comprising a 26 mm top layer of combined skin and fat and an underlying 20 mm thick muscle layer. These values were validated by measurements. The skin/fat layer was modelled with

$\epsilon_r$  of 14.5 and conductivity  $\sigma$  of 0.25 S/m, and the second layer with  $\epsilon_r$  of 55.1 and  $\sigma$  of 0.93 S/m as suggested in [7].

The permittivity of the loaded PDMS substrate was determined experimentally by the waveguide transmission method described in [15]. The material was supported by expanded polystyrene foam and placed in a rectangular waveguide. Comparison of the scattering parameters with and without the PDMS sample present determined the dielectric constant of the loaded substrate to be 3.4 as discussed in Chapter 4. To verify this result, a physical prototype of the tag was fabricated by etching the design of Figure 5.17 onto a copper clad thin Mylar sheet. Cooper clad laminated DuPont polyimide film with copper foil on one side was used to laminate the metal side with a UV sensitive photoresist. To achieve the desired metal part, only certain portions of the photoresist are exposed to ultraviolet light, allowing the unexposed portions to be dissolved away. By the aid of chemicals unexposed portions were removed and the image of the RFID tag antenna as a cooper clad is left. Measurement using a Voyantic Tagformance Lite system indicated the read range to be unchanged when the tag was placed either on the loaded PDMS substrate or on Perspex which also has a permittivity value of 3.4.

### 5.2.3 Strain RFID Sensor

The strain RFID sensor design arose from a passive UHF RFID tag in the form of a transfer patch similar to a temporary tattoo that mounted directly onto the skin surface. The transfer tag is suitable for monitoring people over time in mission critical and secure environments [7]. The strain sensor design dimensions were retuned for the new stretchable substrate, PDMS. The geometry and dimensions of the tag are shown in Figure 5.17 and Table 5.2.

Simulation with CST Microwave Studio using a substrate with  $\epsilon_r$  of 3.4, Figure 5.18, indicated the radiation efficiency to be -12.5dB. In order to establish

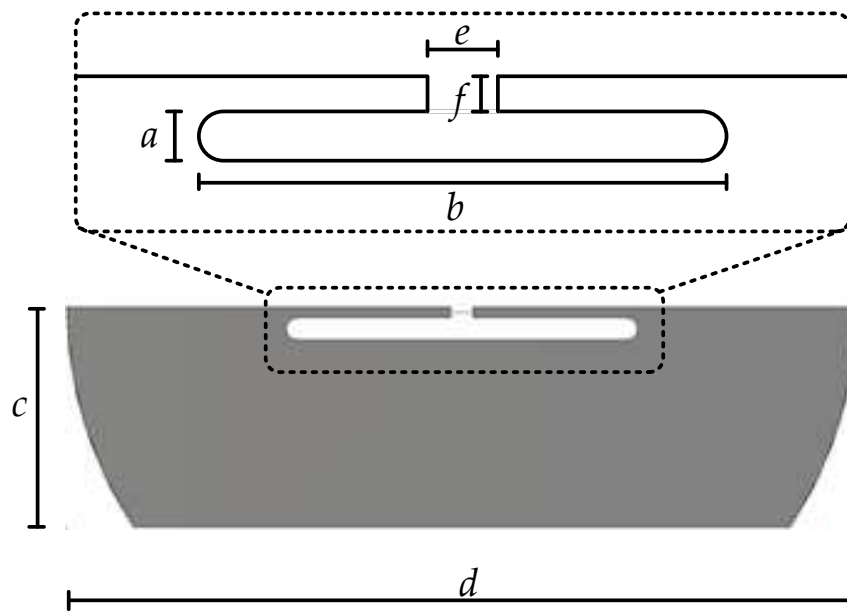


Figure 5.17: Geometry of the RFID Strain Sensor.

Table 5.2: Strain RFID sensor dimensions.

Parameters	Symbol	Length
Slot Width	$a$	1.5
Slot Length	$b$	20
Tag Width	$c$	20
Tag Length	$d$	50
Chip Length	$e$	2
Feed Line Thickness	$f$	1

the accuracy of the body phantom and the PDMS material values, a full tag prototype was assembled using an NXP UHF RFID chip with -15 dBm sensitivity and the loaded PDMS sample. The entire structure was placed on the skin of a volunteer's forearm using adhesive tape. The backscattered power was measured by the Voyantic system and a predicted maximum read range of 1.6 m at 865 MHz was obtained as shown in Figure 5.19. This corresponded well with the simulated  $S_{11}$  null as shown in Figure 5.20.

There are various methods to deposit conducting materials directly onto

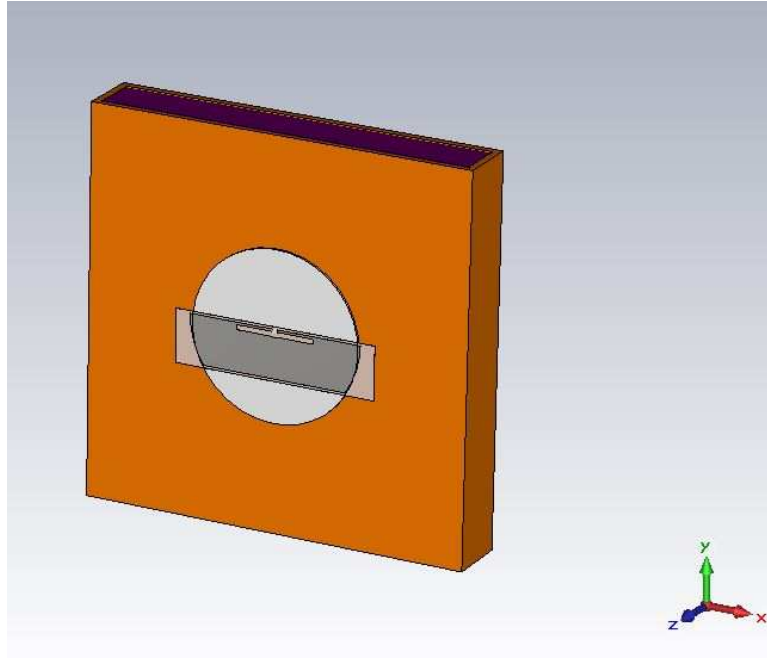


Figure 5.18: CST simulation of stretchable PDMS strain sensor on arm.

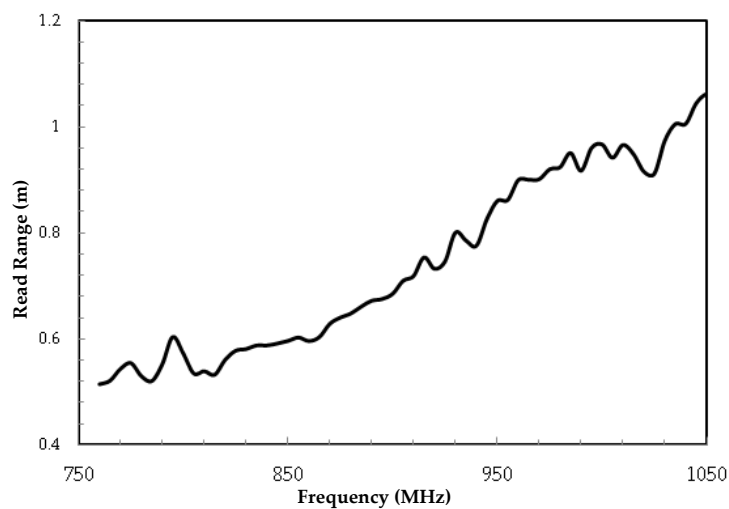


Figure 5.19: Measured read range of a stretchable PDMS strain sensor mounted on an arm.

polymer substrates such as printing or sputtering. However, owing to micro-cracking with applied strain, the resulting antennas suffer from poor efficiency and reduced gain. Additionally, the stretched structures may not cycle well and do not regain their original performance after being relaxed [16, 17].

In this application, rather than attempting to deposit or print conducting layers, a stretchable conducting Lycra<sup>®</sup> fabric containing silver threads was



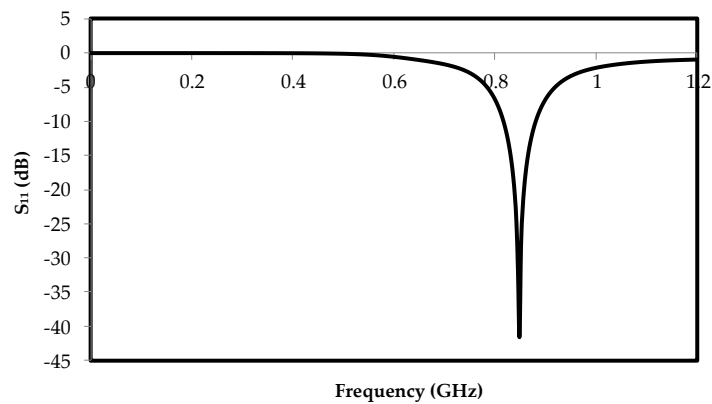


Figure 5.20:  $S_{11}$  simulations of on arm stretchable PDMS strain sensor.

used [18]. This material is formed from highly elastic polyether/polyuria fibres embedded with silver nanoparticles. Chemical etching does not suit porous substrates so laser cutting was used. The original slot was rectangular, however the feed lines were compromised by over-burn at the slot ends as shown in Figure 5.21. This problem was remedied by rounding the slot design as shown in Figure 5.22(b).

### *Deformation during laser cut*

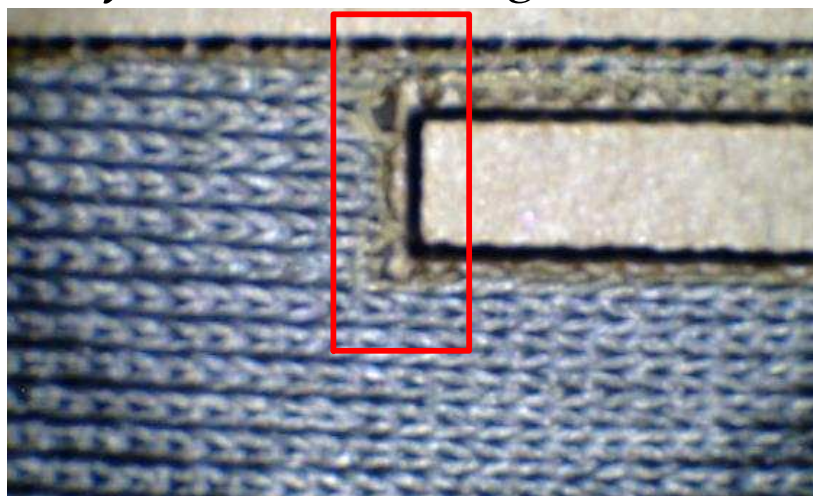


Figure 5.21: Deformation of conductive Lycra during laser cut.

The silver Lycra antenna was attached to the PDMS during the curing process so no adhesive was required. Preliminary studies showed premature placing of the Lycra caused a loss in conductivity, as the semi-cured composite penetrated the fabric and coated the silver fibres. The coating insulated the parallel conducting strands in the fabric and increased the bulk resistivity. As the feed line width  $f$  of the slot design was only 1 mm the feeds were particularly susceptible to conductivity degradation from the composite seeping through before it dried. To remedy this, the main body of the antenna was placed onto the composite at 75 minutes into curing while the feed lines were placed at 95 minutes. The composite was then left to cure at room temperature for a further 25 minutes before being placed in the oven for 72 hours. The resulting tag showed excellent Lycra antenna adhesion, with no visible PDMS seepage. Finally, after the sample was cured, the stretchable conductive fabric was firmly stuck to the substrate surface and the similarity of Young's Moduli between the two meant they could be strained with no visible wrinkling around the conductor edges causing differential stretch. The circular PDMS substrate was 40 mm in diameter and 1 mm in thickness.

The assembled tag with the conducting stretchable fabric was tested attached to skin and found to have a lower read range than the etched prototype. This was to be expected and is due to the conducting Lycra's lower electric conductivity than bulk copper. The Lycra conductivity was measured as 800 S/m with a four probe ohmmeter. The peak read range for both occurred at 868MHz. Low conductivity Lycra functions as a skin tag as tissue losses are also very high. The read range is compromised though.

In order to assess the tag performance under strain, read measurements for various percentage strains were obtained using a PTFE jig. To examine the stretch effect in the  $x$  and  $y$  axis directions, the tag was clamped in the jig on the substrate right and left edges ( $x$ -axis), and the top and bottom edges ( $y$ -axis) respectively.

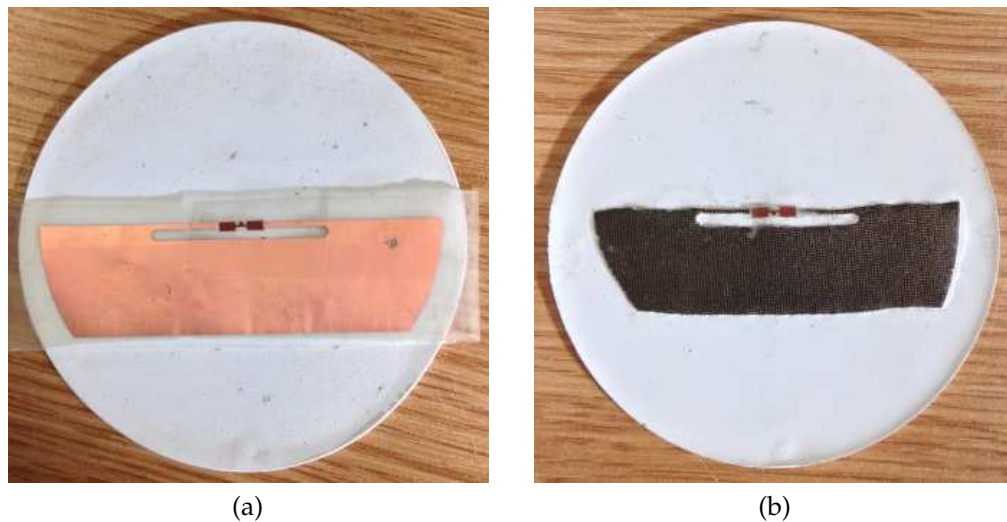


Figure 5.22: PDMS structure (a) with Mylar, (b) with stretchable conductive fabric.

Stretch on the  $x$ -axis distorts the substrate into a horizontally aligned elliptical structure and makes the slot longer and narrower ( $a$  decreases,  $b$  increases). Conversely,  $y$ -axis stretch causes the slot to become shorter and wider ( $a$  increases,  $b$  decreases). Strain is expressed as a percentage change in  $a$ , (positive for  $x$  stretch and negative for  $y$ ). Figure 5.23(a) and Figure 5.23(b) illustrate the unstrained and  $x$ -axis strain conditions respectively.

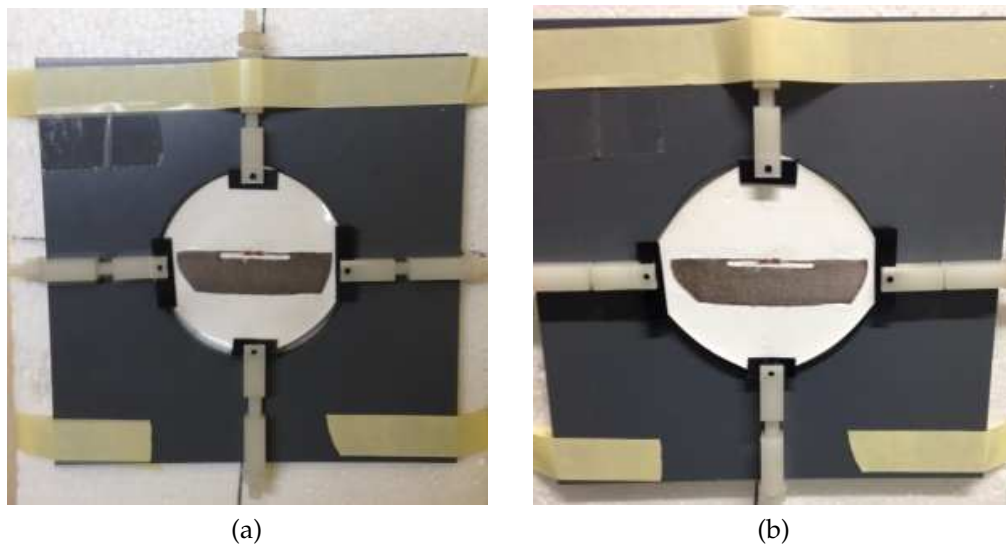


Figure 5.23: Strain measurements on jig (a) unstrained, (b)  $x$ -axis 10% stretched tag.

#### 5.2.4 Results and Discussion

The tag was optimized to work on skin, and therefore, the read range was somewhat compromised by the jig mounting. Fixing the prototype to skin with a suitable adhesive was a problem. However, while read range will change stretch effect should not be determined on/off skin. Successful operation on skin is indicated by simulation and some measurement taken on the VoyanticLite system.

The principal of sensing is similar to that proposed in [19] where a sensed parameter detunes the tag and the magnitude of the change is detected as an alteration in measured backscattered power for a given transmitted signal. The tag backscattered power changes in this case due to a physical distortion and consequent change in the tag input transmission coefficient,  $\tau$ .

Each measurement was repeated five times to remove fluctuations due to narrow band fading, and the average is presented. The results for the stretched and unstretched tag are presented in Figure 5.24 and it can be seen that the

read range is rather poor due to detuning in the unstretched state, requiring about 26 dBm transmit power which is so close to maximum available power to activate the chip. For  $x$ -axis stretching, where the slot became longer and narrower, the impedance match improved and the required reader transmit power reduced.

To assess the performance over time, the tag remained on the jig in the 10% stretched state for one week, after which the measurements were repeated. As shown in Figure 5.24, at the operating frequency (868 MHz), the difference between the new and original measurements was about 0.2 dBm which is in an acceptable range.

Figure 5.25 shows the strain gauge transfer response relating strain to required reader power. Positive strains correspond to  $x$ -axis stretch where  $a$  increases and  $b$  decreases, while negative strains indicate  $y$ -axis strain where  $a$  and  $b$  have the opposite trends. Approximating the response to a linear trend indicates a sensitivity of 1 mW/percent strain. In this case, the most significant error between measurement and trend is 2.4%. In order to prevent any inaccuracies brought by the calibration, the calibration settings were kept the same for after one week results in maximum errors of 1.8% and 0.8% for  $x$ - and  $y$ -axis strains respectively. The reason for the apparent improvement in calibration with time is due to the fact that the measurements taken after a week offer a slightly better fit to a linear trend than the originals. Even though the slope of the second measurement trend line is 0.277, as opposed to 0.252, most of the second data points lie quite close to the original trend and there is no significant outlier. Although this particular effect would not be expected in practice, nevertheless, it can be concluded that the strain gauge remains well calibrated after being stretched over significant periods of time.

The tag was left in the jig under maximum strain for one week and the measurements were repeated to assess performance over time. The measured

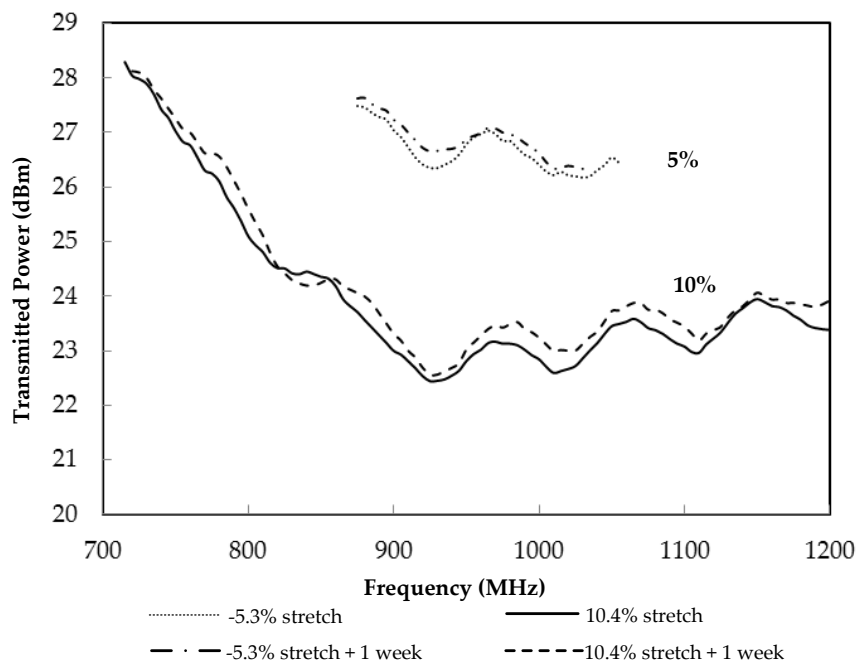


Figure 5.24: Measured transmitted power vs. frequency graph with  $x$ -axis stretch.

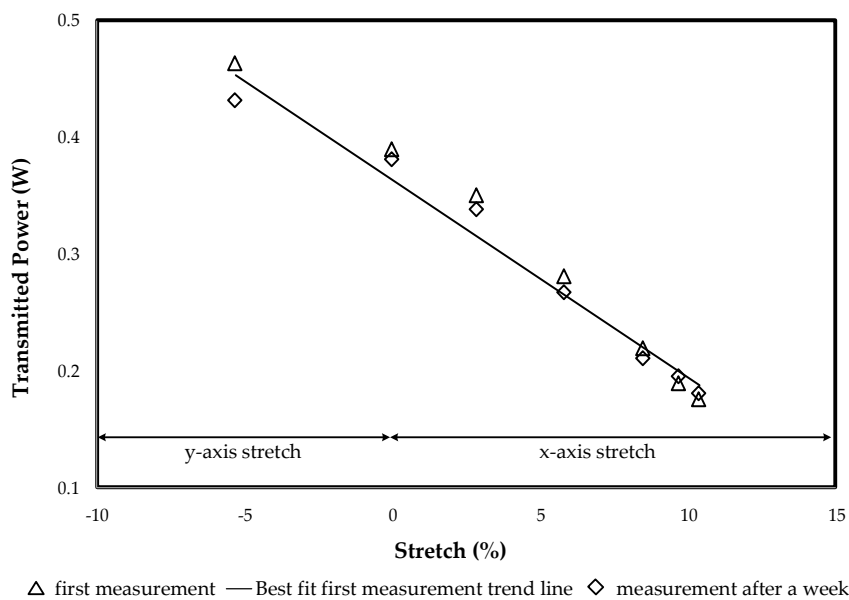


Figure 5.25: Measured transmitted power to activate the chip vs stretch graph.

power values for the two measurements are extracted from Figure 5.25 and presented in Table 5.3 where positive stretch corresponds to  $x$ -axis strain and negative stretch to  $y$ -axis elongation. While it is evident that the tag response

has remained stable over the intervening period, a further investigation into the results was carried out to assess the likely errors. Table 5.4 presents the values of linear trend line fitted to the Week 0 measurements as well as a first order polynomial curve. In both cases error values are given for each strain.

Table 5.3: Comparison of measured transmitted power achieved on week 0 and week 1.

Strain Direction	Transmitted power (dBm)		
	Slot Length (mm)	Week 0	Week 1
<i>y</i> -axis	-5.3	26.4	27.1
-	0	25.8	25.7
<i>x</i> -axis	2.9	25.4	24.9
<i>x</i> -axis	5.8	24.3	24.0
<i>x</i> -axis	8.5	23.4	23.3
<i>x</i> -axis	9.7	23.1	23.0
<i>x</i> -axis	10.4	22.9	22.8

Table 5.4: Curve fitting to week 0 strain results.

Slot Length (mm)	Linear trend line	Week 0 linear trend error	1 <sup>st</sup> order polynomial fit	Week 0 Polynomial fit error
	Week 0 P <sub>tx</sub> (dBm)	%	Week 0 P <sub>tx</sub> (dBm)	%
-5.3	26.9	-2.0	26.4	0.0
0	25.5	1.1	25.9	-0.2
2.9	24.8	2.4	25.3	0.6
5.8	24.1	0.8	24.4	-0.6
8.5	23.4	0.0	23.4	0.0
9.7	23.1	-0.9	22.9	0.1
10.4	22.9	-1.6	22.6	0.0
Error RMS		3.9		0.9
Error Mean		-0.03		0.00

Table 5.5: Week 0 curve fitting to week 1 strain results.

Slot Length (mm)	Measured power drift (week 0 to week 1) (dBm)	Error using week 0 linear trend with week 1 measurement %	Error using week 0 polynomial fit with week 1 measurement %
-5.3	1.2	-0.8	1.2
0	0.3	1.4	0.1
2.9	-0.6	1.9	0.0
5.8	0.9	1.7	0.3
8.5	-0.8	-0.7	-0.7
9.7	-0.6	-1.5	-0.5
10.4	-0.5	-2.1	-0.5
Error RMS	2.0	4.0	1.6
Error Mean	-0.02	-0.02	-0.02

The results of curve fitting the week 0 data given in Table 5.4 indicate that although fitting a linear trend line to the transmit power data results in almost 4% RMS error, the data is evenly balanced above and below the line, giving a mean error magnitude of just 0.03%. The first order polynomial fit gives an RMS error of 0.9% and zero mean.

Table 5.5 demonstrates the low level of drift in the tag response over one week of continuous strain. The change in measured response has an RMS error of just 2%. The RMS error using the original trend line after one week remains at 4%, while the mean error falls very slightly to a magnitude of 0.02%. The polynomial curve offered a close fit to the week 0 data and is therefore slightly compromised when applied after 1 week. However, it still gives RMS and mean errors of only 1.6% and 0.02% respectively after one week. The single biggest observed error after 1 week is -2.1% corresponding to the linear trend line for a 10.4 mm strain. The highest observed error occurs in the week 0 data, being 2.4% for 2.9 mm strain, however, this is not a statistically significant effect as



the overall RMS and mean errors are almost unchanged for the trend line over the week.

### 5.3 Conclusion

The principle of a passive epidermal strain sensor enabled by a UHF RFID tag on a flexible PDMS substrate has been demonstrated. The increase in permittivity associated with the Barium Titanate loading in the substrate allowed the effect of tag detuning to be emphasized as a function of stretch, and additionally, the substrate material parameters allow an 1 m read range which is an acceptable performance when mounted directly onto skin. Strains of up to 10% have been tested leading to read transmit power differences of about 4dB which should be easily detectable after averaging over multiple reads to remove fast fade fluctuations. The error analysis is also studied to assess the repeatability of the sensor behaviour in a time being.

To act as a practical and highly conformal transfer mounted sensor, the substrate will be investigated for performance as a thin film significantly less than 1 mm in height.

For future development, to offer a control interface for severely incapacitated wheelchair users with limited or no movement in their arms, fingers and hands, a mouth mounted UHF RFID tag acting as a tongue touch controlled switch has been proposed to offer joystick or mouse control on a powered wheelchair [20]. For use in a muscle tweak sensor for a joystick or mouse application, the associated reader system would be integrated into a powered wheelchair and calibration would be required to account for variability in the distance between tag and read antenna. Using a separation of less than 1 m between the reader and the tag would lower the required reader transmit power and reduce the effect of multipath. Finally, the unique ID code embedded into each

tag transponder would allow for multiplexing in 4 vector control systems as required by joysticks or computer mice.

## References

- [1] C. Occhiuzzi, S. Cippitelli, and G. Marrocco, "Modeling, design and experimentation of wearable RFID sensor tag," *Antennas and Propagation, IEEE Transactions on*, vol. 58, no. 8, pp. 2490–2498, Aug 2010.
- [2] G. Marrocco, L. Mattioni, and C. Calabrese, "Multiport sensor RFIDs for wireless passive sensing of objects - basic theory and early results," *Antennas and Propagation, IEEE Transactions on*, vol. 56, no. 8, pp. 2691–2702, Aug 2008.
- [3] G. Marrocco and F. Amato, "Self-sensing passive RFID: From theory to tag design and experimentation." in *Science, Progress and Quality at Radiofrequencies, Conference Proceedings - 39th European Microwave Conference, EuMC 2009*, 2009, pp. 1–4.
- [4] S. Milici, S. Amendola, A. Bianco, and G. Marrocco, "Epidermal RFID passive sensor for body temperature measurements," in *RFID Technology and Applications Conference (RFID-TA), 2014 IEEE*, Sept 2014, pp. 140–144.
- [5] M. Gillham, B. McElroy, G. Howells, S. Kelly, S. Spurgeon, and M. Pepper, "Weightless neural system employing simple sensor data for efficient real-time round-corner, junction and doorway detection for autonomous system path planning in smart robotic assisted healthcare wheelchairs," in *Emerging Security Technologies (EST), 2012 Third International Conference on*, Sept 2012, pp. 161–164.
- [6] M. Ziai and J. Batchelor, "A prototype passive UHF RFID transfer tattoo tag," in *Antennas and Propagation (EUCAP), Proceedings of the 5th European Conference on*, April 2011, pp. 3811–3814.
- [7] ———, "Temporary on-skin passive UHF RFID transfer tag," *Antennas and Propagation, IEEE Transactions on*, vol. 59, no. 10, pp. 3565–3571, Oct 2011.

- [8] V. Sanchez-Romaguera, M. A. Ziai, D. Oyeka, S. Barbosa, J. S. R. Wheeler, J. C. Batchelor, E. A. Parker, and S. G. Yeates, "Towards inkjet-printed low cost passive UHF RFID skin mounted tattoo paper tags based on silver nanoparticle inks," *J. Mater. Chem. C*, vol. 1, pp. 6395–6402, 2013.
- [9] E. Cherney, "Silicone rubber dielectrics modified by inorganic fillers for outdoor high voltage insulation applications," in *Electrical Insulation and Dielectric Phenomena, 2005. CEIDP '05. 2005 Annual Report Conference on*, Oct 2005, pp. 1–9.
- [10] A. Babar, T. Bjorninen, V. Bhagavati, L. Sydanheimo, P. Kallio, and L. Ukkonen, "Small and flexible metal mountable passive UHF RFID tag on high-dielectric polymer-ceramic composite substrate," *Antennas and Wireless Propagation Letters, IEEE*, vol. 11, pp. 1319–1322, 2012.
- [11] L. K. Namitha and M. T. Sebastian, "Microwave dielectric properties of flexible silicone rubber - Ba(Zn<sub>1/3</sub>Ta<sub>2/3</sub>)O<sub>3</sub> composite substrates," *Materials Research Bulletin*, vol. 48, pp. 4911–4916, 2013.
- [12] G. Marrocco, "Pervasive electromagnetics: Sensing paradigms by passive RFID technology." *IEEE Wireless Communications*, vol. 17, pp. 10–17, 2010.
- [13] —, "The art of UHF RFID antenna design: impedance-matching and size-reduction techniques," *Antennas and Propagation Magazine, IEEE*, vol. 50, no. 1, pp. 66–79, Feb 2008.
- [14] L. Guo, H. Luo, J. Gao, L. Guo, and J. Yang, "Microwave hydrothermal synthesis of barium titanate powders," *Materials Letters*, vol. 60, no. 24, pp. 3011 – 3014, 2006. [Online]. Available: <http://www.sciencedirect.com/science/article/pii/S0167577X06002096>
- [15] B. Sanz-Izquierdo, J. Batchelor, and M. Sobhy, "Button antenna on textiles for wireless local area network on body applications," *Microwaves, Antennas Propagation, IET*, vol. 4, no. 11, pp. 1980–1987, November 2010.

- 
- [16] Q. Liu, K. Ford, R. Langley, A. Robinson, and S. Lacour, "Stretchable antennas," in *Antennas and Propagation (EUCAP), 2012 6th European Conference on*, March 2012, pp. 168–171.
- [17] A. Arriola, J. Sancho, S. Brebels, M. Gonzalez, and W. De Raedt, "Stretchable dipole antenna for body area networks at 2.45 GHz," *Microwaves, Antennas Propagation, IET*, vol. 5, no. 7, pp. 852–859, May 2011.
- [18] [Online]. Available: <http://www.lessemf.com/321.pdf>
- [19] S. Merilampi, T. Bjorninen, L. Ukkonen, P. Ruuskanen, and L. Sydanheimo, "Embedded wireless strain sensors based on printed RFID tag," *Sensor Review*, vol. 31, no. 1, pp. 32–40, 2011.
- [20] O. Rakibet, D. Oyeka, and J. Batchelor, "Passive RFID switches for assistive technologies," in *Antennas and Propagation (EuCAP), 2013 7th European Conference on*, April 2013, pp. 1917–1920.

# CHAPTER 6

## PASSIVE RFID TONGUE PROXIMITY SENSOR

\* \* \*

A passive RFID mouth tag for assistive technologies is presented in this chapter. The tag is intended to fit directly on the hard palate and detect tongue position in the mouth to provide a tongue controlled interface for a joystick or computer mouse for paraplegics who have fine motor control capability of their tongues. The tag is demonstrated to have definite on/off switched states as well as a range of resolvable intermediate values. An assessment is made on different users to demonstrate the training period required to be able to hit defined targets with accuracy.

## 6.1 Introduction

Powered wheelchairs give mobility to people who would otherwise be unable to move around independently. A real-time response in navigation and steering systems to facilitate collision avoidance is an important factor in semi-autonomous powered wheelchair design.

The SYSIASS project was explained in Chapter 5 as a project to develop autonomous wheelchairs. The input devices for the wheelchair control need to provide a human-computer interface which is convenient, hygienic and preserves dignity by being unobtrusive. Also, in rehabilitation scenarios assistance should not be over-supportive and must be dynamically altered to suit the current needs of a patient with an improving, or degenerating condition. When administered correctly, the rehabilitation procedure should provide the correct level of support to encourage patients to gain increased independence as they learn to manage a condition [1] and control an assistive technology such as a powered wheelchair.

The standard means of controlling a powered wheelchair is by the use of a hand joystick; but many severely disabled people, including tetraplegics, have either no, or inadequate, hand control to use a standard joystick. For these users, a range of alternative human input devices (HIDs) is available, including chin joysticks, head switches and sip-puff devices. This client group also has difficulty, both in communicating, and also controlling a computer mouse. Again, there are several alternatives to hand controlled computer HIDs, including switch interfaces and eye scanning systems such as "Eyegaze". However, a natural, mouse-like input device is highly desirable [2–7].

While allowing severely disabled individuals to use a powered wheelchair, many alternative HIDs provide only limited or slow control, which often makes driving a frustrating experience. However, a large proportion of this population

retain normal, or almost normal, use of the tongue which is an extremely dextrous organ, making it suited to operate a HID.

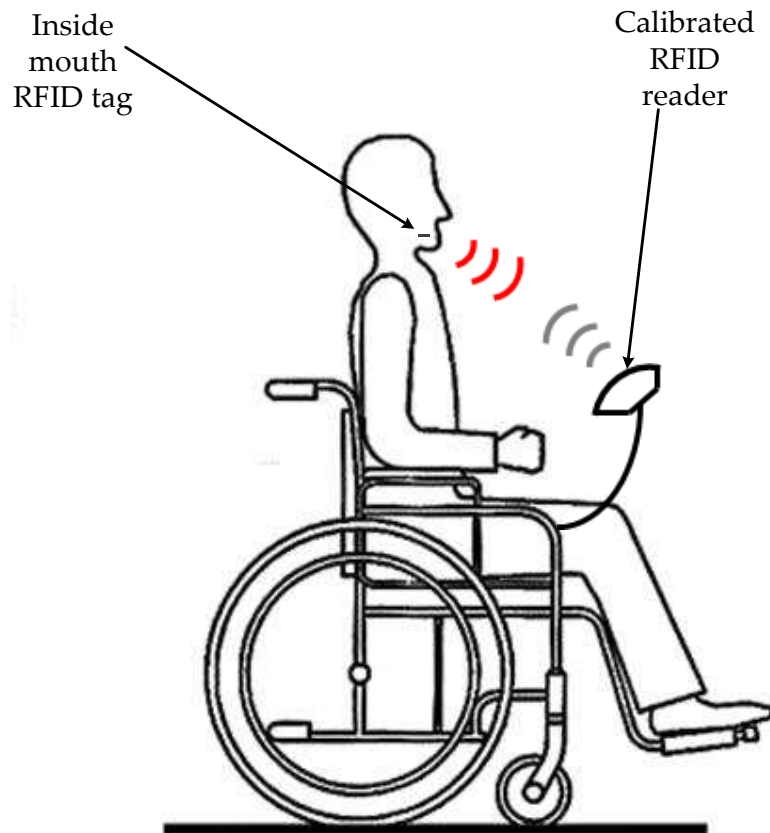


Figure 6.1: Reader antenna concept.

An epidermal strain gauge attached above the eyebrows or on the neck could act as a muscle tweak sensor for joystick or mouse control on a powered wheelchair for a severely incapacitated user having little or no movement in their arms, fingers or hands [8, 9]. The epidermal strain gauge described in is battery-free (passive) and communicates wirelessly to an external reader using RFID technology was described in Chapter 5. However, in this chapter, a UHF RFID tongue proximity sensor to facilitate tongue control of a wheelchair or computer mouse is proposed again offering human input device functionality. Additionally, the training process for the system is described. A conformal tag can be attached to the hard palate in the mouth and the effective capacitance due to the tongue proximity will detune the tag. This detuning affects the



transmission coefficient at the tag terminals, changing the realized tag gain and therefore altering the backscattered and required reader transmit powers when the tongue moves with respect to the tag. When combined with a proximal read antenna, placed in front of the mouth at about 30 cm distance (Figure 6.1), there is an opportunity to monitor the tongue proximity and therefore control a wheelchair.

## 6.2 In Mouth RFID Tag

In this section, the initial tag design and preliminary measurement results, together with modifications to increase the ease of wear are presented. The measurement and simulation results are also provided with simple and more detailed mouth models. Once the tag design is finalized in terms of best performance and best conformity, the training period to use the in-mouth RFID tag sensor is also studied.

A simple mouth model was developed as two main parts, a rectangular block with a semi hemisphere cavity representing the upper part of the mouth and a thinner rectangular block representing the tongue, Figure 6.16.

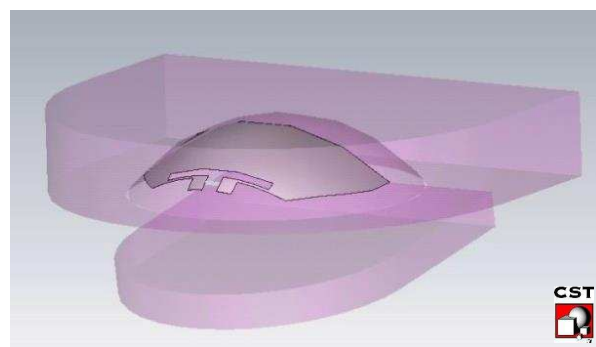


Figure 6.2: Homogeneous simple CST mouth model for UHF RFID tag simulations.

As presented in Chapter 3, a detailed mouth model was developed for accurate simulations where all mouth tissues were included such as upper mouth, upper mouth cavity, tongue and teeth as shown in Figure 6.3. After preliminary measurements, tissue characteristics in simulations are modified and revalidated with further measurements which are explained in detail later in this chapter.

In both mouth models, lower jaw and the tongue are pivoted to perform the simultaneous tongue and lower mouth movements.

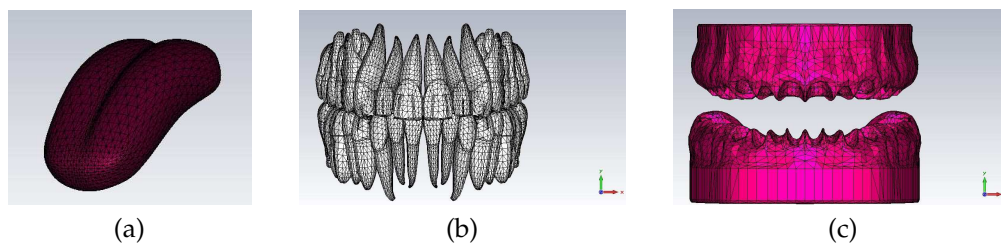


Figure 6.3: Mouth model components (a) tongue, (b) teeth and (c) gums.

### 6.2.1 Initial In Mouth Tag Design

The tag is derived from a design by the Antennas Group at University of Kent [10, 11]. The tag was initially attached to the hard palate to observe its functionality in the mouth with different tongue positions.

The tag structure is presented in Figure 6.4 with its dimensions listed in Table 6.1. In order to save metal or ink during the tag fabrication process, the conduction regions observed to support negligible simulated surface current were removed from the design. As shown in Figure 6.5, when the tag which is etched onto a Mylar clad, as explained in Chapter 5, is simulated on the body tissue, the surface current at 1000 MHz is concentrated around the slot. The detailed tag design arising from the transfer tattoo tag design was discussed in Chapter 3.

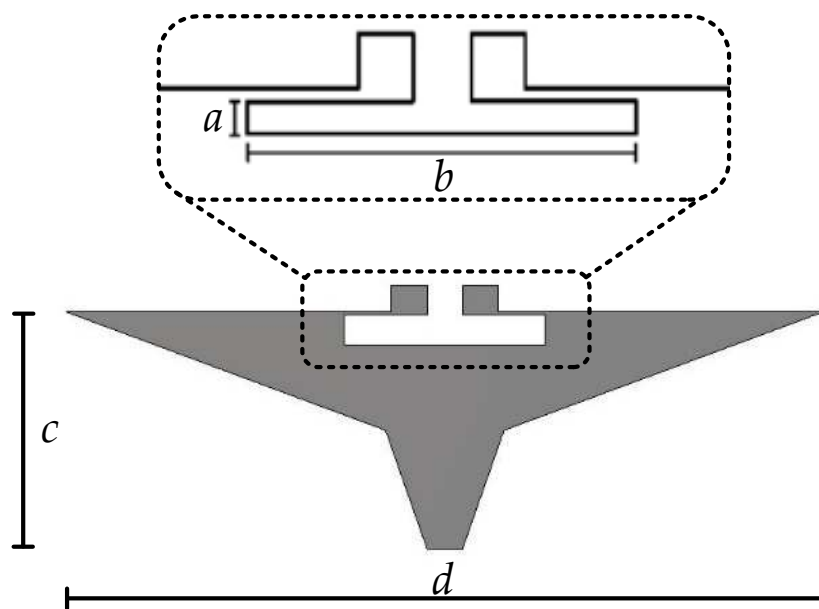


Figure 6.4: Geometry of the initial in mouth RFID tag on Mylar substrate.

Table 6.1: Dimensions of the initial in mouth RFID tag.

Slot Width	Slot Length	Tag Width	Tag Length
$a$	$b$	$c$	$d$
2 mm	16 mm	20 mm	64 mm

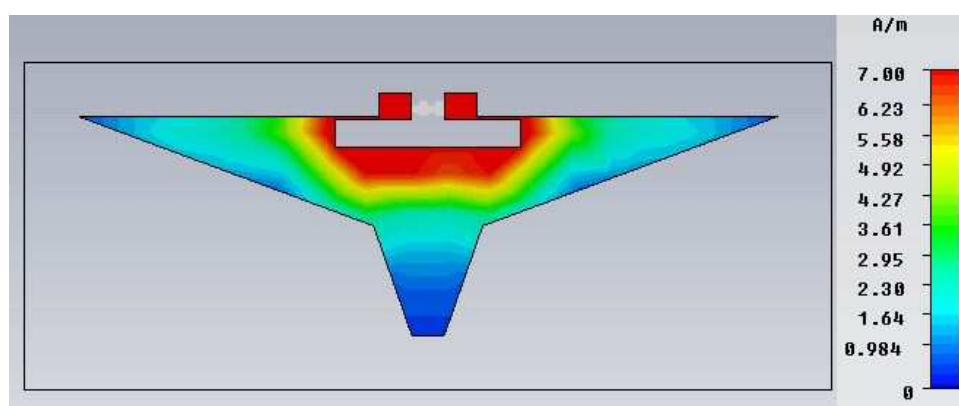


Figure 6.5: Simulated surface current at 1000MHz of the initial tag on arm.

### 6.2.1.1 In Mouth Tag Measurement Setup

In this application, as the reader antenna will be fixed in front of the user about 30 cm from the mouth, read ranges of about 1m will ensure reliable communication. The measurement configuration in Figure 6.9 was used. The peak read range for the tag on the hard palate was measured to be 1.1m and occurred at 1000 MHz and which corresponded well with the simulated  $S_{11}$  null frequency shown in Figures 6.6 and 6.7. A commercial dental adhesive was used to affix the Mylar tag substrate to the hard palate, Figure 6.10.

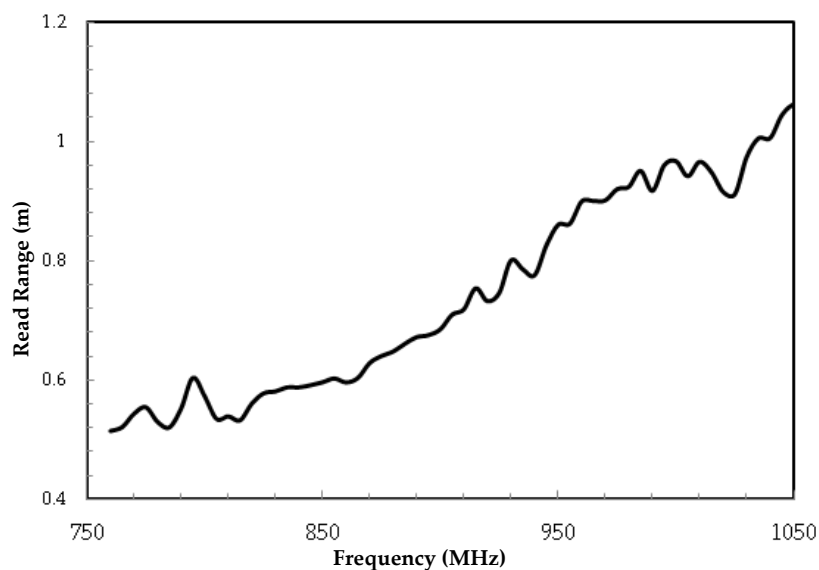


Figure 6.6: Measured read range of mouth tag on hard palate.

A set of expanded polystyrene foam spacers (relative permittivity approximately that of air) with known thicknesses were used to set the distance between the tag and the tongue in order to be able to assess the tag operation as a function of tongue proximity as shown in Figure 6.8. In order to remove the variations introduced by narrow band fading and human movement, each measurement data set was repeated five times and the average is presented.

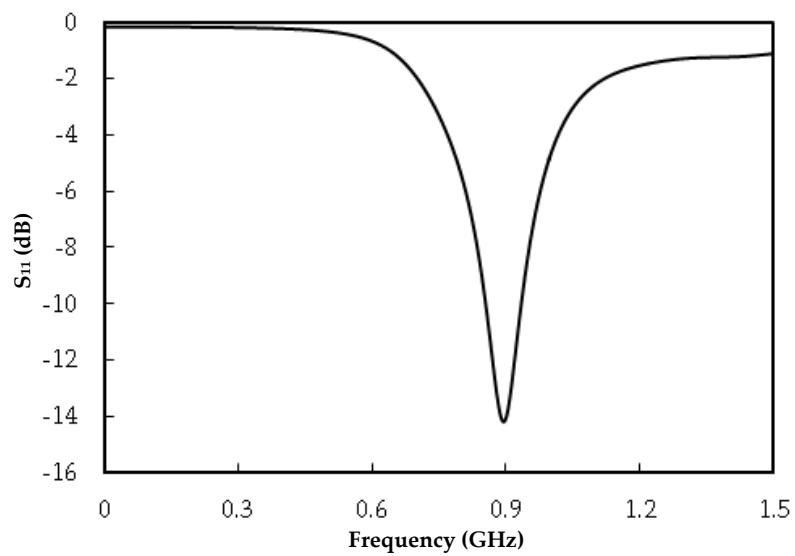


Figure 6.7: Simulated  $S_{11}$  parameters on arm.

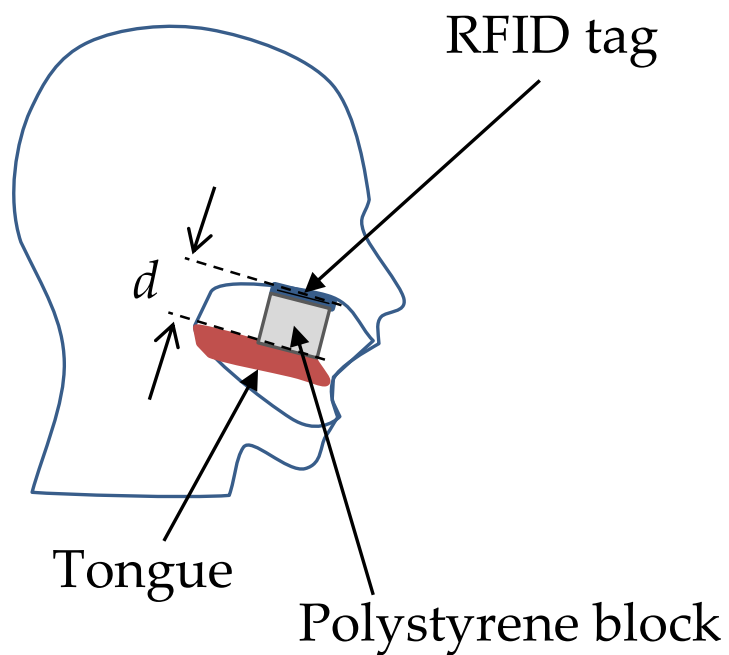


Figure 6.8: In mouth polystyrene blocks to separate tongue and tag.

Voyantic Tagformance Lite equipment was used for the measurements. This system ramps the transmit power and records the value when tag communication is established. Transmitted and corresponding backscattered power values

were obtained for each tongue-tag separation distance.

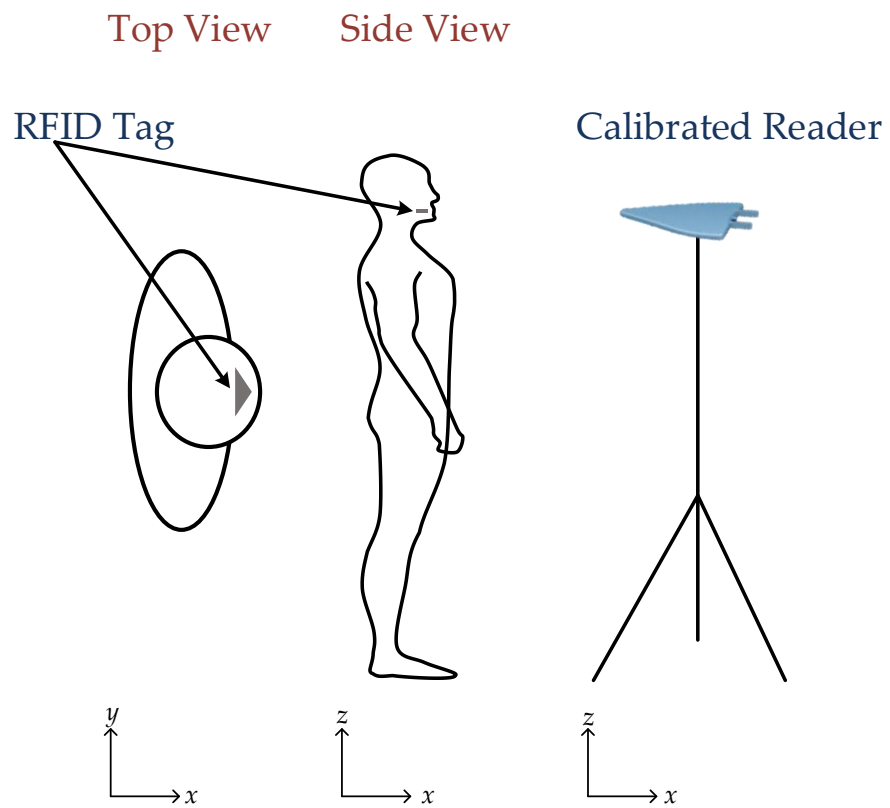


Figure 6.9: Measurement Setup.



Figure 6.10: Applying dental adhesive to the RFID tag.

### 6.2.1.2 Results

In order to observe the effect of the tongue on the behaviour of the RFID tag, the results are compared while the tongue is touching, and when the tongue is separated from the tag by a fixed distance as shown in Figure 6.11. The read range, which is the usual parameter for assessing tag reponsivity, is extrapolated from the measured backscattered power together with the calibrated transmit EIRP.

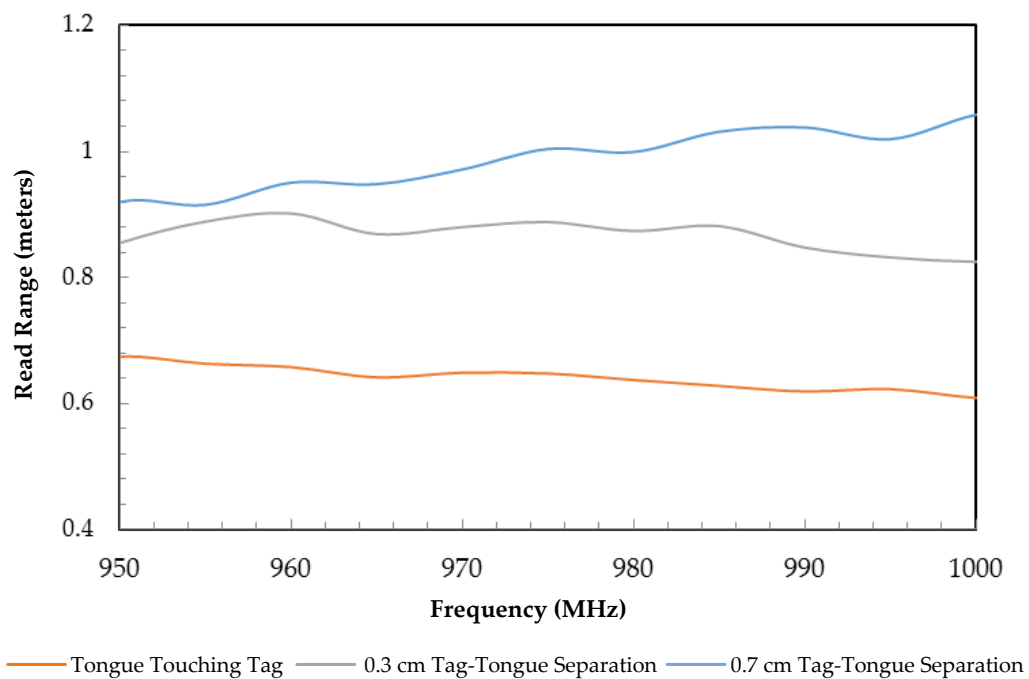


Figure 6.11: Measured read ranges with different tongue-tag separations by initial RFID tag.

By calculating the numerical difference between the measured read range values for different tongue-tag separations, it is possible to observe the differential effect of the tongue on the tag as a function of distance. The difference between read range while the tongue is touching and when the tongue is separated from the tag by 0.3cm and 0.7cm have been assessed by subtracting the measurement datasets from the case where the tongue was touching the tag. As a result of capacitive loading of the tongue as it moves near the tag, the read is affected

and decreased. As shown in Table 6.2, the differential effect can be seen to decrease as the tongue moves further from the tag. This is expected as the capacitive loading effect diminishes for a distant tongue.

Table 6.2: Measured read ranges differences with different tongue - tag separations by the initial RFID tag at 1000MHz.

	0.7 cm - Touching	0.3 cm - Touching	0.7 cm - 0.3 cm
Read Range Difference (m)	0.28	0.18	0.07

With appropriate calibration, by setting the threshold read range value between the on/off states, it is anticipated that a proximity detector could be implemented as well as a simple binary switch.

### 6.2.2 Modified In-Mouth Tag

It became clear when taking the initial measurements, that the tag was too large for a comfortable fit in the mouth as it overlapped the teeth. By examining the surface current in Figure 6.4, it was decided to remove additional conductor and reduce the dimensions to those shown in Figure 6.12 and Table 6.3. The tag-teeth overlap issue was resolved by trimming the sides of the tag where the tag dimensions were reduced by 3%. The simulated surface current was low on the removed locations and it did not affect the tag performance significantly. Figure 6.13 shows the surface current distribution of the tag after modification. It is clearly seen that the higher current is still concentrated around the slot and the current distribution is essentially unchanged.



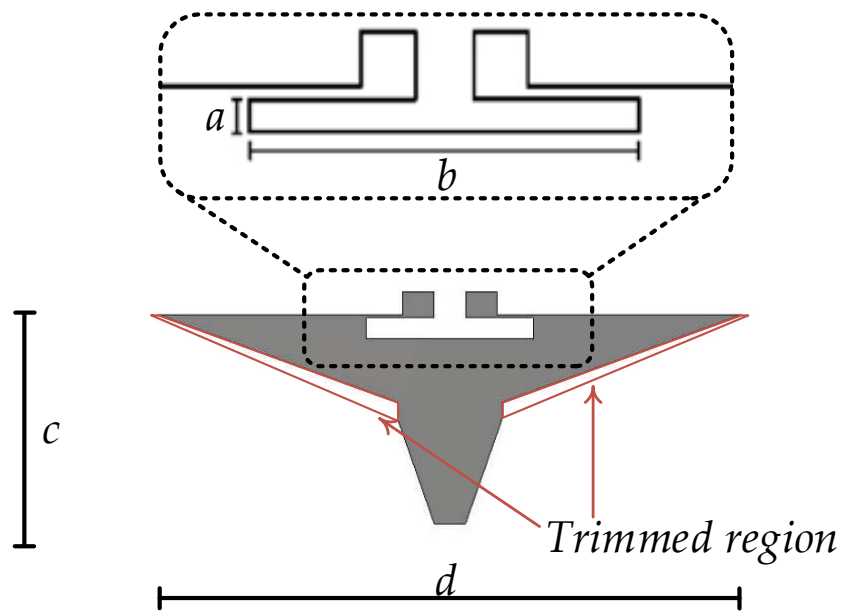


Figure 6.12: Geometry of the modified in mouth RFID tag.

Table 6.3: Dimensions of the modified in mouth RFID tag.

Slot Width	Slot Length	Tag Width	Tag Length
$a$	$b$	$c$	$d$
1.5 mm	20 mm	16 mm	56 mm

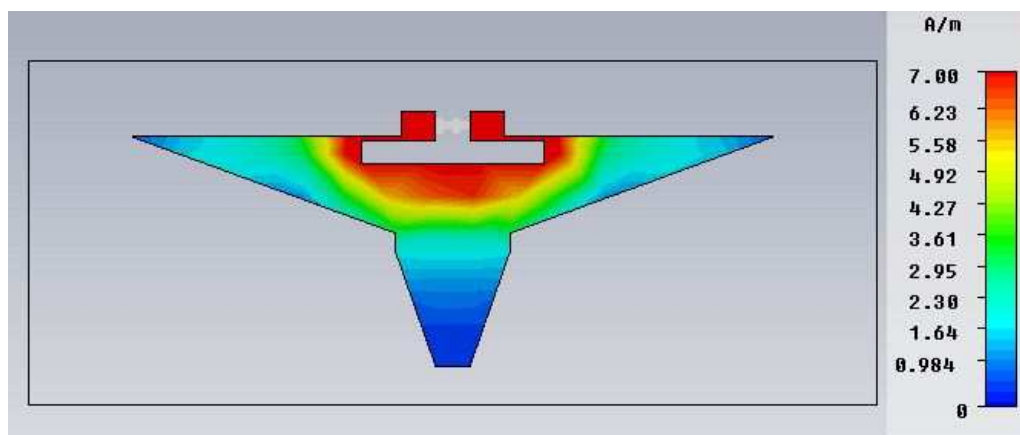


Figure 6.13: Simulated surface current of the modified tag.

### 6.2.2.1 Results

The modified tag performance was measured in-mouth using the procedure described in Section 6.2.1.2.

The read ranges are shown in Figure 6.14 and differential read ranges are given in Table 6.4. Again the differential read range decreased as the tongue moved further from the tag, though the sensitivity is reduced because of the decreased tag size. The smaller tag surface area reduces the realized gain which therefore reduces read range.

The data in Table 6.4, again indicates that with correct calibration and processing, it should be possible to create a degree of proximity sensing of the tongue to the tag on the hard palate within the mouth.

Modifying the tag and making it smaller, slightly reduced the read range, but these results are still acceptable for functionality.

Table 6.4: Measured read ranges differences with different tongue - tag separations for the modified RFID tag.

	2.4 cm Touching	1.2 cm - Touching	0.6 cm - Touching	2.4 cm - 0.6 cm	2.4 cm - 1.2 cm	1.2 cm - 0.6 cm
Read Range Diff. (m)	0.24	0.14	0.04	0.21	0.10	0.11

Diff. stands for Difference.

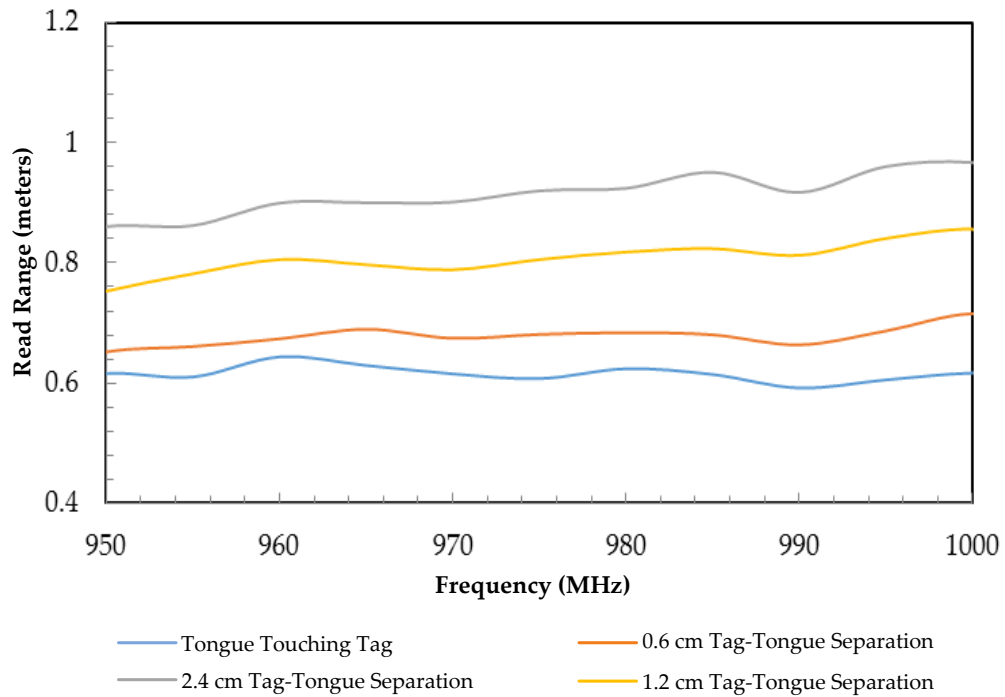


Figure 6.14: Measured read ranges with different tongue-tag separations for the modified RFID.

### 6.2.3 Final Conformal Tongue Touch RFID Tag

A final reduced size version of the tag was developed with surface dimensions small enough to fit comfortably onto the hard palate and is shown in Figure 6.15 with dimensions listed in Table 6.5. To aid the fit into the mouth, two corners were rounded and a prototype was created on a copper clad 0.043 mm Mylar sheet with a etching process explained in Chapter 5.

Table 6.5: Dimensions of the conformal tongue touch RFID tag.

Slot Width	Slot Length	Tag Width	Tag Length
$a$	$b$	$c$	$d$
1.5 mm	20 mm	20 mm	50 mm

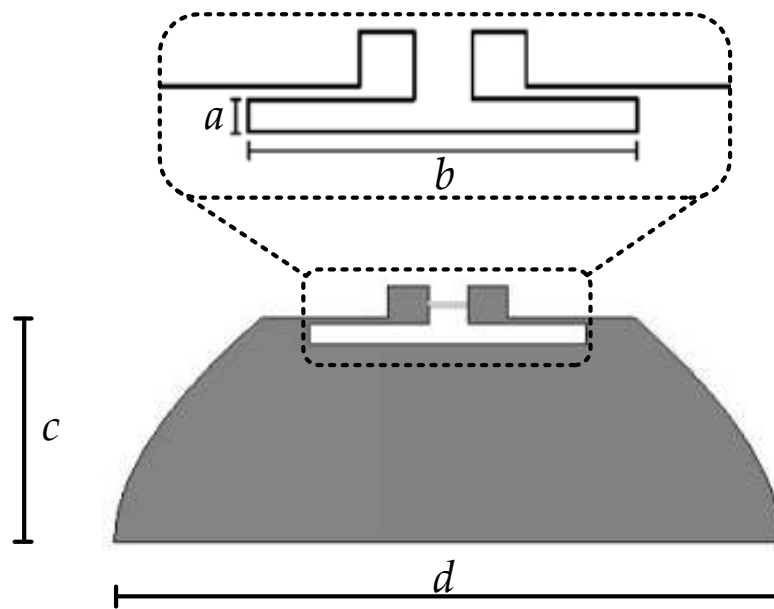


Figure 6.15: Geometry of the conformal tongue touch RFID tag.

#### 6.2.4 Simple Mouth Model

In order to represent the signal propagation in the mouth, a very simple homogeneous flesh model was created in CST Microwave Studio as shown in Figure 6.11. The hard palate and tongue are comprised of a material with  $\epsilon_r = 55$  and conductivity  $\tan \delta = 0.94S/m$  which are appropriate for 900 MHz.

Simulations were taken for comparison with measurement at the same tongue-tag separations and the impedance matching coefficient  $\tau$  was derived from the simulated reflection coefficient in each case. The tag gain was also obtained for each simulated tongue position. As already discussed, the tag was designed such that the increased capacitive loading associated with an approaching tongue would progressively detune the tag. A commercial dental adhesive was used to affix the Mylar tag substrate to the hard palate, Figure 6.18.

In passive systems, the transponder IC is activated with the power collected by the tag antenna and modulated backscattered power is returned to the reader.

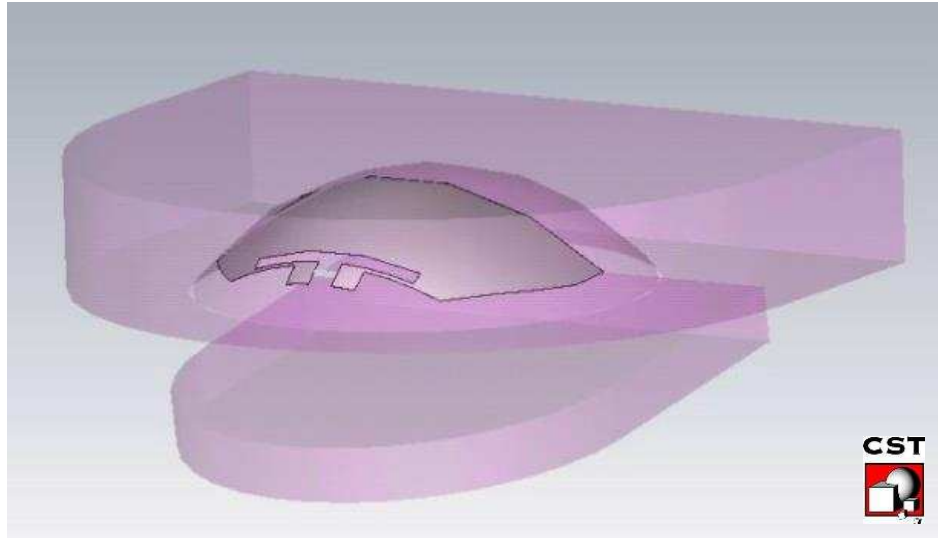


Figure 6.16: Homogeneous simple CST mouth model for UHF RFID tag simulations.

The achievable read distance,  $R$ , is calculated by the following equation as shown earlier in Chapter 3:

$$R \leq \frac{\lambda}{4\pi} \sqrt{\frac{EIRP_{reader} \times G_{tag} \times \eta \times \tau \times \rho}{P_{th}}} \quad (6.1)$$

If read ranges more than a few cm are to be achieved, it is important to obtain a strong impedance matching coefficient as the very low profile skin-mounted tags suffer from low radiation efficiency. The power transmission coefficient is calculated by [12, 13]:

$$\tau = 1 - |\Gamma|^2 = \frac{4R_a R_{IC}}{(R_a + R_{IC})^2 + (X_a + X_{IC})^2} \quad (6.2)$$

where:

$$0 \leq \tau \leq 1 \quad \text{and} \quad \Gamma = \frac{Z_{IC} - Z_a^*}{Z_{IC} + Z_a}, \quad 0 < |\Gamma| < 1. \quad (6.3)$$

A conjugate match ( $Z_{IC} = Z_a^*$ ) is required to establish the maximum power transfer from the tag antenna to the chip. Therefore, the  $\Gamma$  value plays a significant role on achievable read range as it represents the match quality and must be kept close to 0 for better read range. A tag where the power transmission coefficient  $\tau$  is a function of some external parameter allows the tag to function as a sensor where the reader is able to determine a corresponding change in backscattered power. This can be achieved by mismatching the tag transponder chip.

Simulations were taken for the same tongue-tag separations as measurement. The impedance matching coefficient  $\tau$  was derived from the simulated reflection coefficient, Figure 6.17. The trend with tongue separation predicts the required change in tag match with a degradation as the tongue approaches the tag. The tag gain was also calculated for each simulated tongue position. As shown in Figure 6.17, the dominant factor which effects the read range is the transmission coefficient while the realized gain is a function of transmission coefficient. Other parameters such as efficiency and gain remain relatively constant when compared to transmission coefficient. For this reason, simulations have focused onto transmission coefficient calculations.

In order to access the tag's performance in the forward and reverse links, the transmitted power by the reader antenna and the backscattered power by the tag, are presented in Table 6.6. The data illustrates how good quality transponder matches (corresponding to large tongue-tag separations) require lower reader transmit power to activate the transponder and result in higher backscattered power.

However, as shown in Figure 6.19 when the tongue is at larger distances from the tag (more than 20 mm), the agreement with simulation is lost. The reason arises from the simplified model of the mouth used in CST. There are no cheeks, lips, teeth or bone included and all tissue is modelled as a single homogenous

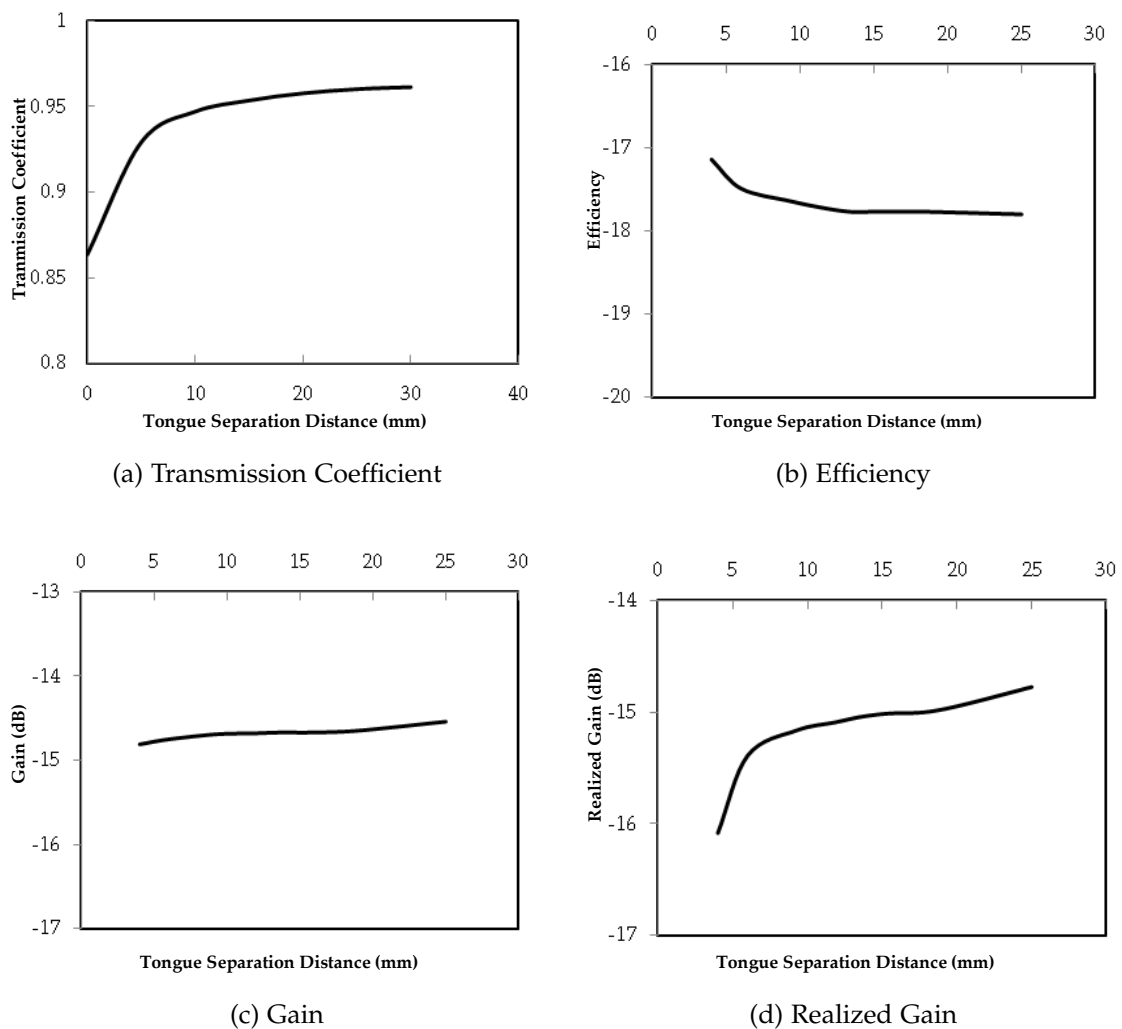


Figure 6.17: Simulated performance parameters of mouth model with different tongue-tag separations.

material. Therefore, at larger tongue separations, the wider mouth environment can be expected to be significant in tag performance. As the tongue moves closer, its significance increases and the simple homogenous tissue model is sufficient until the tag becomes very close (less than 5mm). A better validated tissue representation is required as small experimental error in tongue position becomes important.

Also, the simulated model assumed that tongue movement did not affect tag polarization as the upper hard palate should not change position. However, in measurements, head tilt might affect read range through tag radiation pattern.



Figure 6.18: Denture adhesive applied to attach the tag to the upper palate.

Table 6.6: In-mouth measurement results.

Polystyrene Thickness (mm)	Transmitted Power (dBm)	Backscattered Power (dBm)
30	22	-52.8
20	23.5	-54.5
15	24	-55
10	26.5	-55.4
6	27	-57.4
4	X	X
2	X	X
0	X	X

X denotes as tag is not detected.

Users tried to keep still, but some movement may have occurred. In final application, severely disabled users would use a head strap to keep their heads still.

### 6.2.5 Accurate Mouth Model

In order to better represent the signal propagation, a mouth model, consisting of teeth, hard palate and tongue available from [14] was imported into CST Microwave Studio as shown in Figure 6.20(a) and (b). At 800 MHz the hard palate and tongue are comprised of a material with  $\epsilon_r = 55$  and conductivity



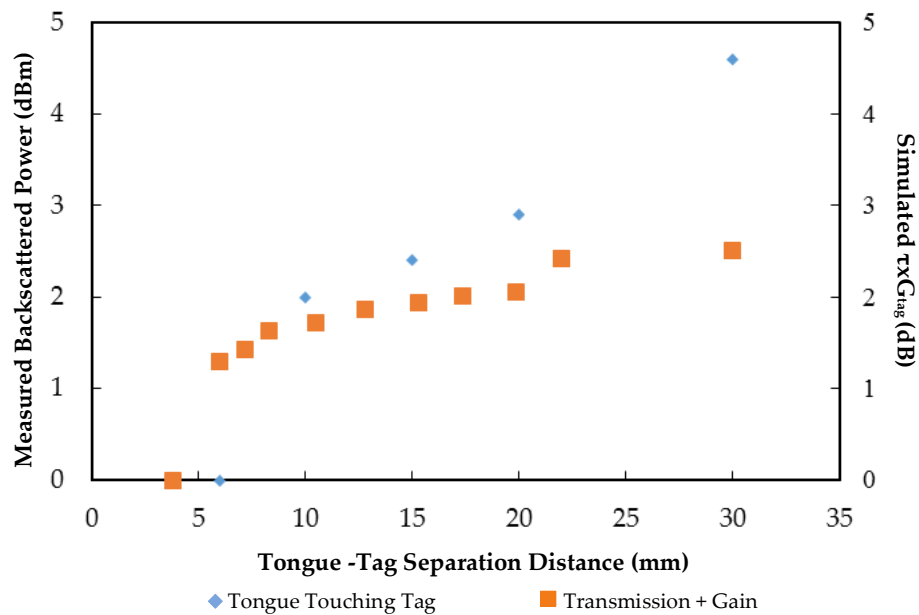


Figure 6.19: Normalised measured backscattered power (blue diamond) and simulated product of impedance match coefficient and tag gain (red square) as a function of tongue-tag separation

$\delta = 0.9S/m$  and the teeth with  $\epsilon_r = 12.5$  and conductivity  $\delta = 0.14S/m$  as published by the Italian Research Council [15]. To obtain good agreement with measurements, it was necessary to adjust the hard palate to an  $\epsilon_r$  30% higher than cartilage. The tag was curved with the CST bending function and positioned precisely in the mouth as shown in Figure 6.20 and Figure 6.21.

The accurate mouth model was simulated with various tongue-tag separations starting from "tongue touching" to 30 mm tongue separation as shown in Figure 6.22. The simulated S-parameters, in Figure 6.23, clearly show an increasing match quality with the increasing tag-tongue separation.

Transmission coefficient values were also extracted from the simulated S-parameter values as shown in Figure 6.24(a) and 6.24(b) by Equations 6.2 and 6.3.

The comparison of two mouth models simulated transmission coefficient

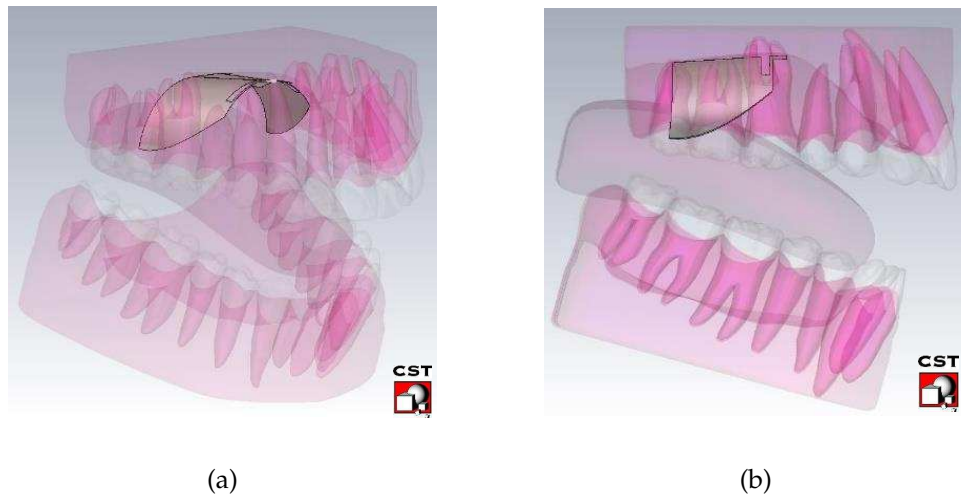


Figure 6.20: Tag positions in simulated mouth (a) Perspective view, (b) Side view.



Figure 6.21: Tag positions in (a) simulated and (b) real mouth.

results are shown in Figure 6.24 with the measured backscattered power. Transmission coefficient results are extracted from the simulated S-parameters for both simple and detailed mouth models where the latter results shown in Figure 6.24 indicate a better trend fit with the measurement results especially on the middle tongue-tag separation region as shown in 6.24(a).

The measurements used the same method as explained in Section 6.2.2.1. The peak read range, 1.1 m was recorded at 800 MHz after mounting on the hard palate and corresponded well to the simulated  $S_{11}$  null where 1m read range is achieved by the measurements to ensure reliable communication.

In order see the effect of lower jaw and lower teeth on the tag performance, the



Figure 6.22: Simulated mouth model with different tongue-tag separations

measurements are compared with different lower jaw and lower teeth positions. Results shown in Figure 6.25 indicate the tag performance is dominated by the tongue capacitive loading effect.

As mentioned, the critical point for the tongue separation is found to be at 4 mm, and smaller distances mean the tag does not read which corresponds to an "off" state. Further, for separations greater than 4 mm, increasing tongue-tag separations led to increasing backscattered powers and this could offer a proximity sensor with an analogue scale for finer control.

As the power transfer coefficient and the tag gain are the two parameters most affected by tongue proximity, the other parameters in Equation 6.1 may be considered constant and the chip sensitivity is a function of only of the ASIC design, meaning that backscattered power depends on just the  $\tau \cdot G_{tag}$  product [16]. This product is compared to measured backscattered power in Figures 6.27, 6.28, 6.29, 6.30 for each tongue-tag separation for three different users, who all

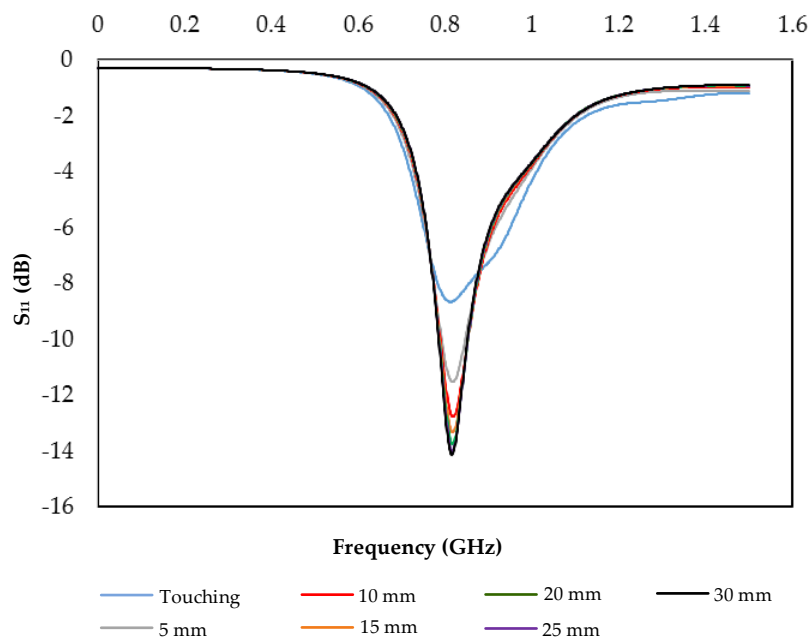
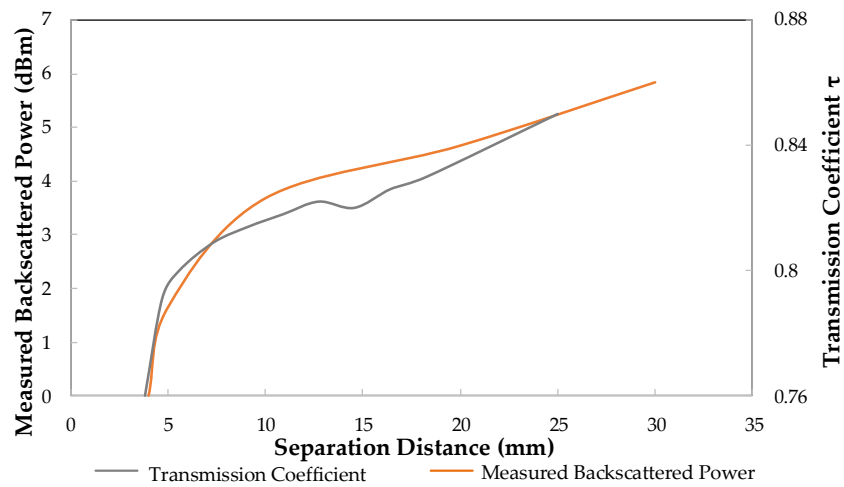


Figure 6.23: Simulated S-Parameters using the accurate mouth model.

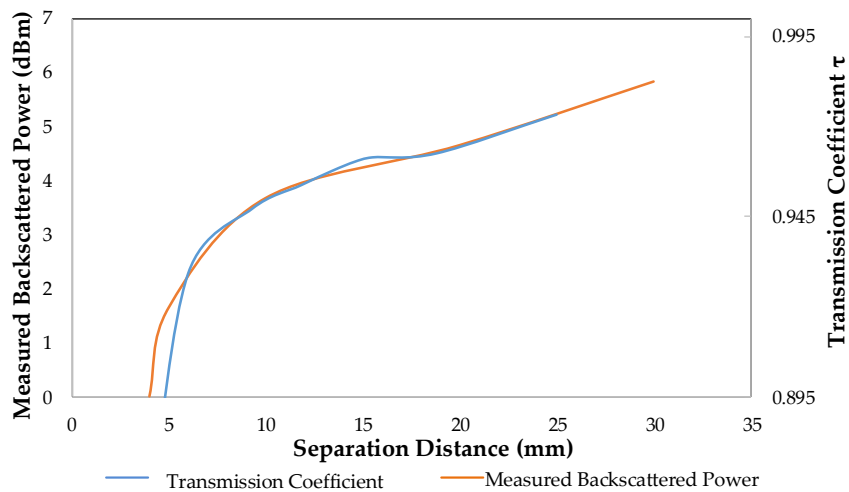
followed the same measurement pattern. To reduce uncertainty, measurements were recorded for each tongue-tag separation in five independent sets and the average taken. Error bars are included in the graphs representing the users' recorded data range.

There is close agreement in trend between the measurement and simulation for all users though the magnitude of received power was different for each person. The simulated model assumed that tongue movement did not affect tag polarization as the hard palate should not change position. However, in measurements, moving the tongue large distances from the hard palate did cause some volunteers to move slightly, and this may have an effect on backscattered power that was not accounted for in the model for each user. Figure 6.26 shows the user during a measurement, the head position kept stable and at the same distance to the reader antenna in all measurements while the tongue and lower jaw are the moving parts of the head.

However, the results in Figures 6.27, 6.28, 6.29 and 6.30 clearly show a repeatable trend between users and the error bars indicate the sensed parameter (in



(a)

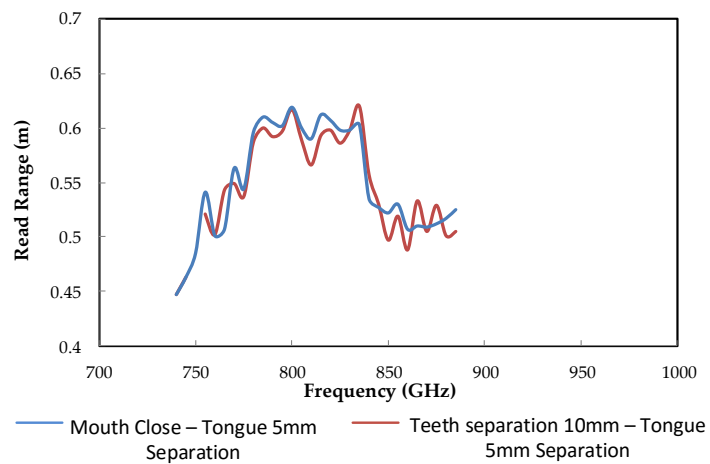


(b)

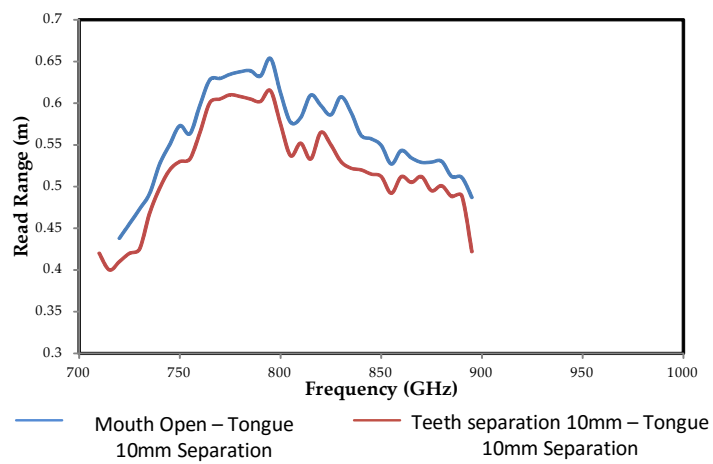
Figure 6.24: Transmission coefficient vs backscattered measurement results. (a) Simple mouth model. (b) Detailed mouth model.

this case backscattered power) can be resolvable between sufficiently spaced tongue proximities.

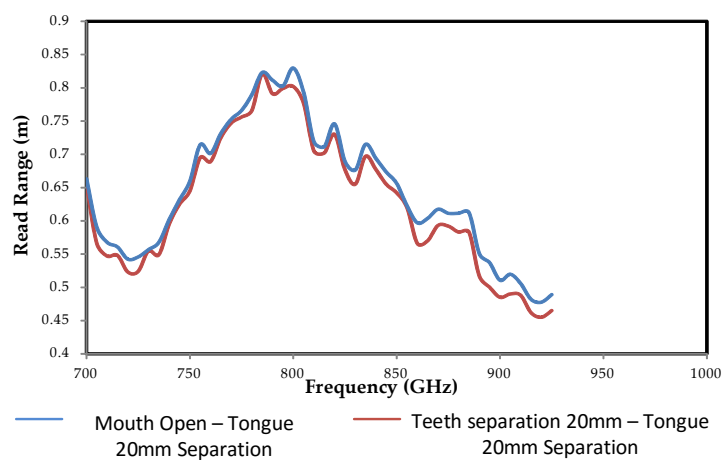
Figure 6.30 shows the average of all three users' measurements compared to simulation, and indicates that for this small population each user was observed to match the simulation well, meaning an average could be taken as a representative response.



(a)



(b)



(c)

Figure 6.25: Simulated mouth model with different tongue-tag separations

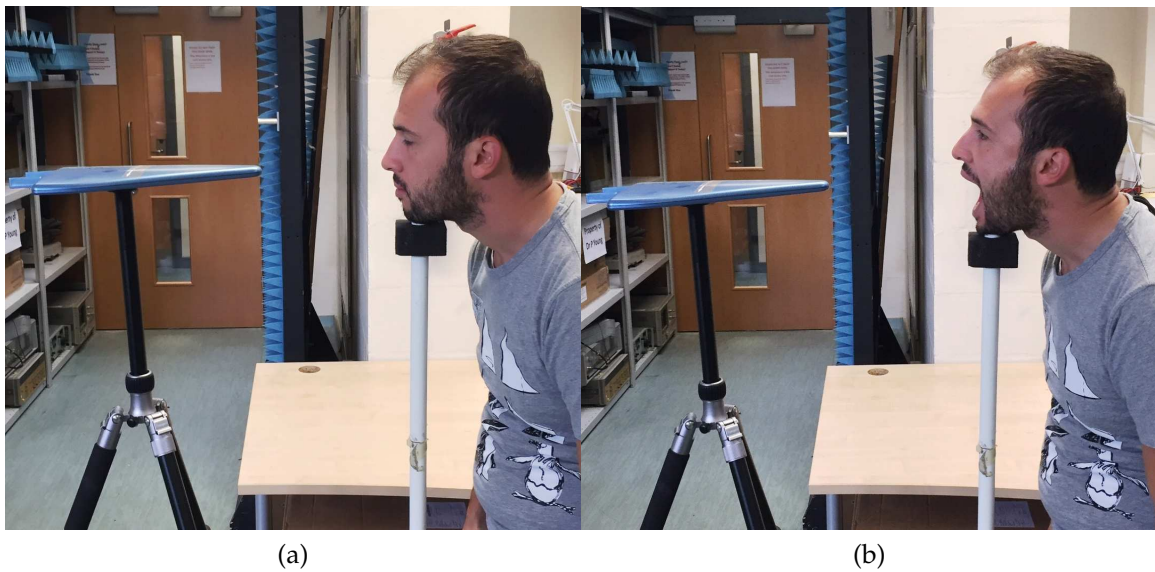


Figure 6.26: User postures (a) Mouth close, (b) Mouth open in measurements.

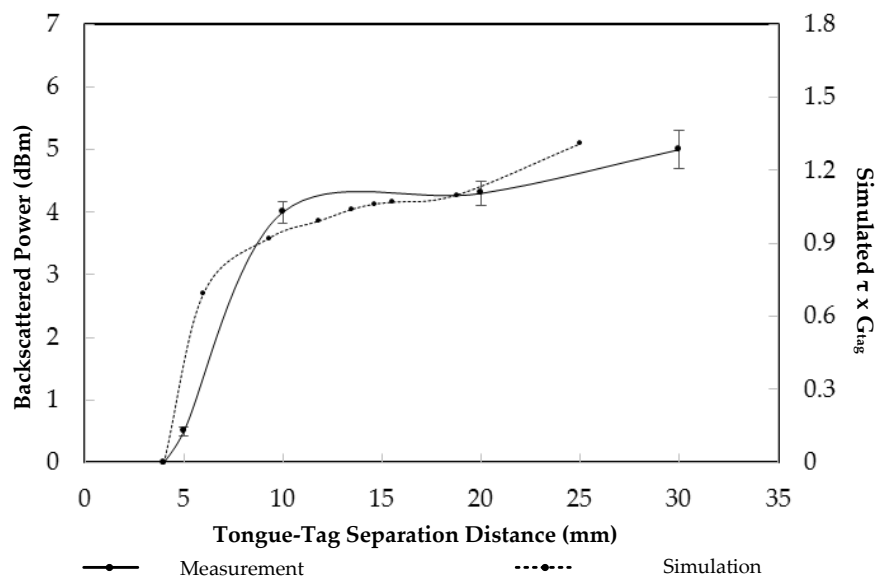


Figure 6.27: User 1 Simulated  $\tau \times G_{tag}$  product vs measured backscattered power.

### 6.3 User Training Process

Having established a good agreement between the CST model and measurement for tag response to tongue distance for three different users, the volunteers were trained to use the system to hit defined read range targets. The read range

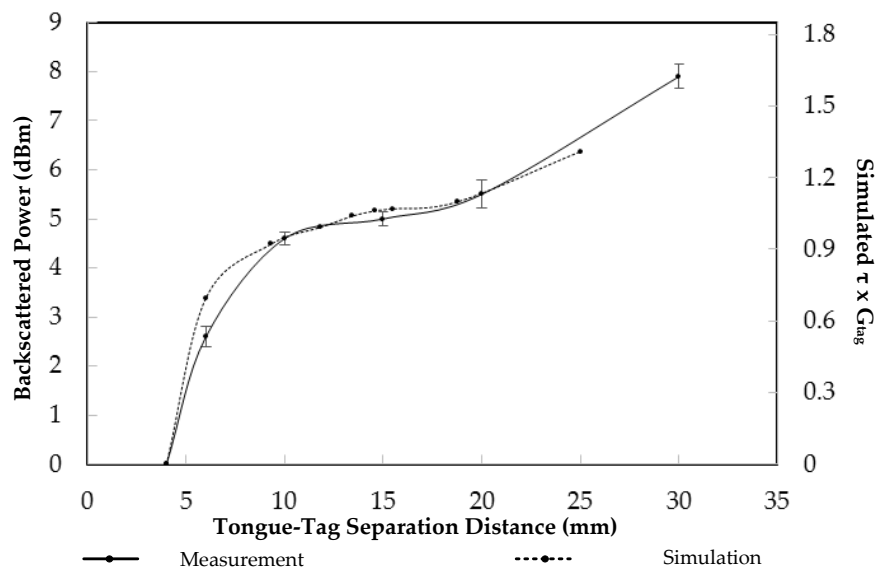


Figure 6.28: User 2 Simulated  $\tau \times G_{tag}$  product vs measured backscattered power.

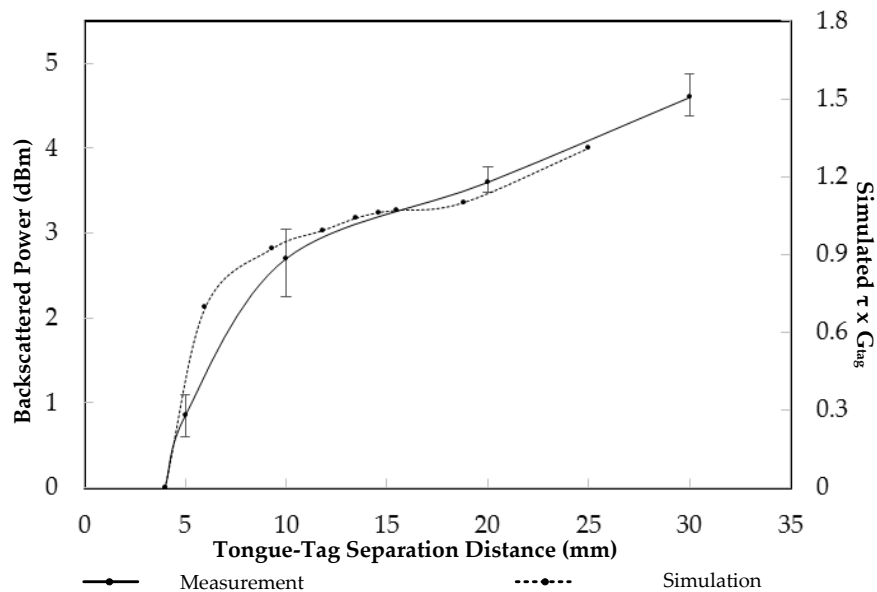


Figure 6.29: User 3 Simulated  $\tau \times G_{tag}$  product vs measured backscattered power.

is automatically extrapolated from the measured reader power and is readily available for display on the Voyantic System. A number of studies were carried out to assess the user accuracy and repeatability in hitting required targets with increasing training time.



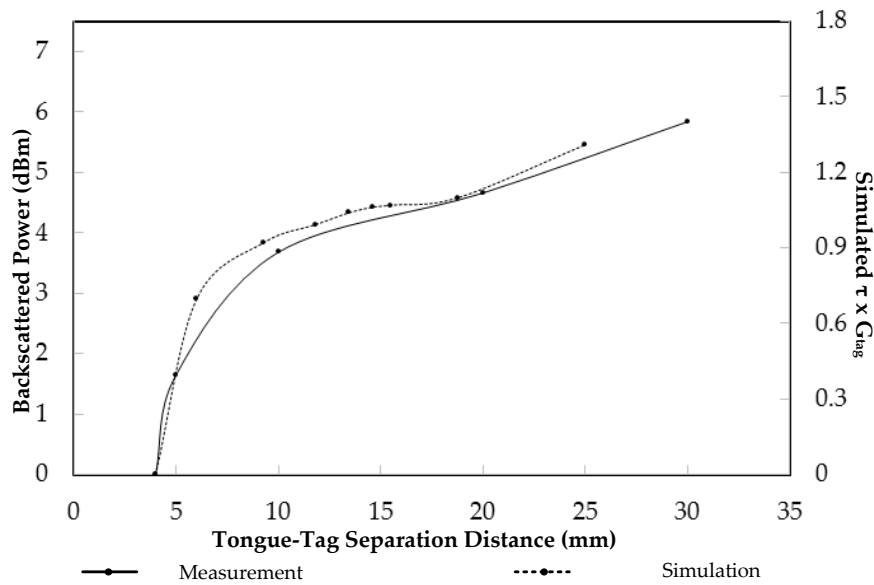


Figure 6.30: Averaged Simulated  $\tau \times G_{tag}$  product vs measured backscattered power.

The first study required the users to locate the easiest target, (0.9 m), where the tongue was moved an almost maximum distance from the tag. This was done seven times for each user to establish how consistently they could find the target with increased practice. The entire process was then repeated seven times for target distances of 0.8 m, 0.7 m, 0.6 m and 0.5 m and in all cases the users had two seconds between being told the target and to find the optimum tongue position. The minimum target distance was set at 0.5m because ranges of 0.4 m or less resulted in no read which was trivial to achieve and required no accuracy.

Error magnitudes in each target distance were averaged over the three users for the seven attempts. The error magnitude  $|E|$  was calculated by:

$$|E| = \left[ \frac{R_m - R_e}{R_e} \right] \times 100\% \quad (6.4)$$

where,  $R_m$  and  $R_e$  are the measured and expected read ranges respectively.

In Figure 6.31, it can clearly be seen that the average user accuracy increased markedly over the sequential attempts for all target distances and errors were no more than 2% for the final try.

The highest errors were usually associated with the 0.5m target owing to its proximity to the tag turn off point at about 0.4m where there was a corresponding high response sensitivity to tongue position as indicated in Figures 6.27, 6.28, 6.29 and 6.30. Conversely, as mentioned, achieving the 0.9m target was more straightforward, usually only requiring the users to move their tongues to the maximum position from the tag and meaning the response was in a region of comparatively low sensitivity to exact tongue separation. Average errors for the 0.9m target were no more than 3.7% for the first attempt, falling to 0.4% for the final try.

The rate at which the test population learnt with subsequent attempts is illustrated in Figure 6.32 where the mean errors of all three users' attempts at each target are presented against each subsequent try. On average, the error magnitude for all targets roughly halved after four attempts and all fell to less than half after five tries. Therefore, it is clear that the users can learn the tongue positions to locate targets with reasonable accuracy after four or five attempts. This was the case for all tongue separation distance measurements where the initial higher error magnitudes reduced and converged on values of a few percent for attempt seven, as evidenced by the clear downward trend in Figure 6.32.

To appreciate the range of accuracy for each target distance, the data for every attempt by all users are plotted on a single graph in Figure 6.33(a). Twenty one data points are presented for each target point corresponding to all three users who have repeated the measurements seven times. It is clear from Figure 6.33(a), that when all seven trials are included, the error spread at each target can be

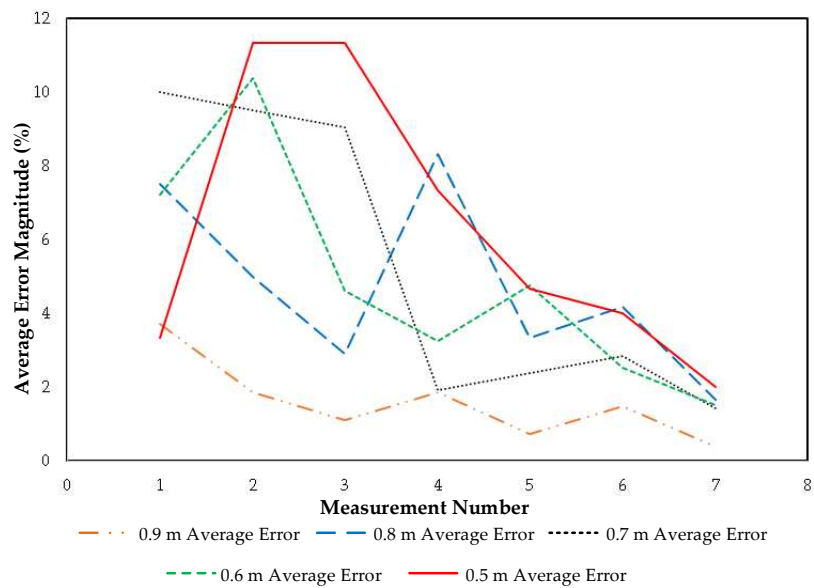


Figure 6.31: Average error of specific target point for each measurement number.

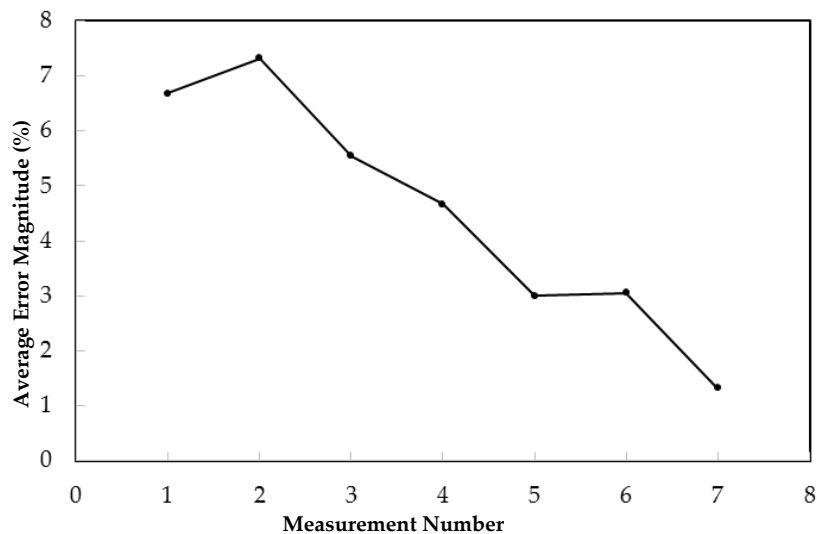
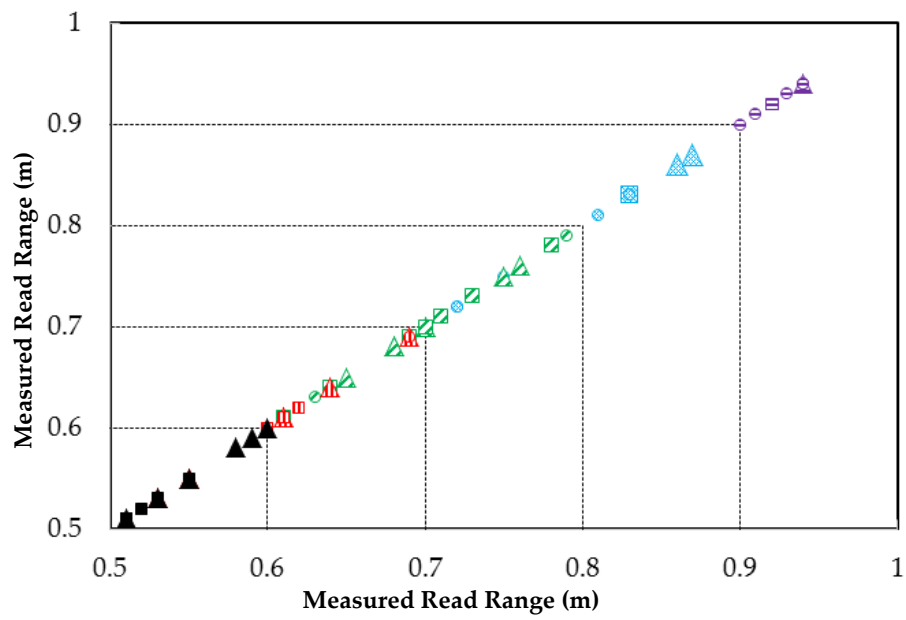


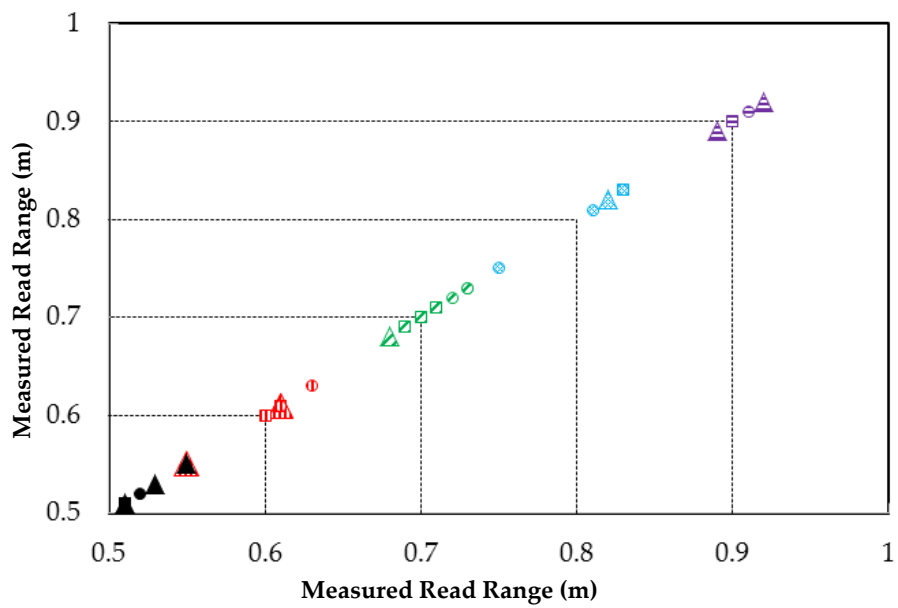
Figure 6.32: Average of all measured errors on each measurement number.

large enough to prevent adjacent targets from being resolved with overlap occurring between all targets except 0.9 m.

In order to appreciate the improvement in target accuracy over the course of the training session, Figure 6.33(b) shows the data for just the final three attempts. A marked reduction in the error spread is noted, meaning that



(a)



(b)

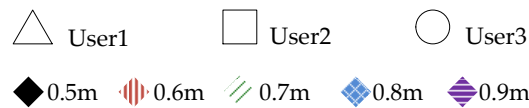


Figure 6.33: Read Range vs Target Read Range (a) All 7 measurement for each user (b) Last 3 measurement for each user.

individual targets are better resolved after training. Neglecting single outliers at 0.6 m and 0.8 m, the data clusters tightly around the target and it is possible to resolve each case.

To prevent the users obtaining deceptively accurate results because they were presented with sequentially reducing target distances, the final part of the training required them to hit the 0.5 m to 0.9 m target distances in a defined sequence of twenty five attempts: 0.9m, 0.9m, 0.7m, 0.8m, 0.6m, 0.6m, 0.8m, 0.9m, 0.8m, 0.8m, 0.8m, 0.7m, 0.6m, 0.9m, 0.5m, 0.9m, 0.7m, 0.7m, 0.8m, 0.8m, 0.9m, 0.9m, 0.8m, 0.5m and 0.6m . As before, the users had two seconds to find each target.

Figure 6.34 shows the error magnitude data for all three users, with each following the same twenty five target sequence. It can be seen that while the error trend reduces even though the targets are not in order, some targets are clearly more difficult for certain users than for others. Tables 6.7(a) and 6.7(b) show the mean error and spread for each user attempting each target, for entire 25 target hit attempts, and just the final 13 attempts respectively. It is clear that all error means and ranges reduce significantly for the final 13 tries with the exception of the 0.5m target which only occurred in the last 13 attempts of the sequence. For the final 13 attempts, the 0.5m target has the highest mean error for Users 1 and 2, while the 0.7m target is most difficult for User 3.

The target error ranges define the limit in target resolution, so the measured data plots for all 25 attempts and just the final 13 are given in Figure 6.35(a) and (b). Figure 6.35(a) shows the 0.5m target is well resolved, even without practice while all other targets have at least one user attempt overlapping their resolvable gaps where the hit target falls to adjacent target point. User 3 produces five overlap errors, while User 1 has four and User 2 has just one instance.

When considering just the final 13 attempts, Figure 6.35(b) the measurement range for each target reduces significantly giving clear gaps between all targets

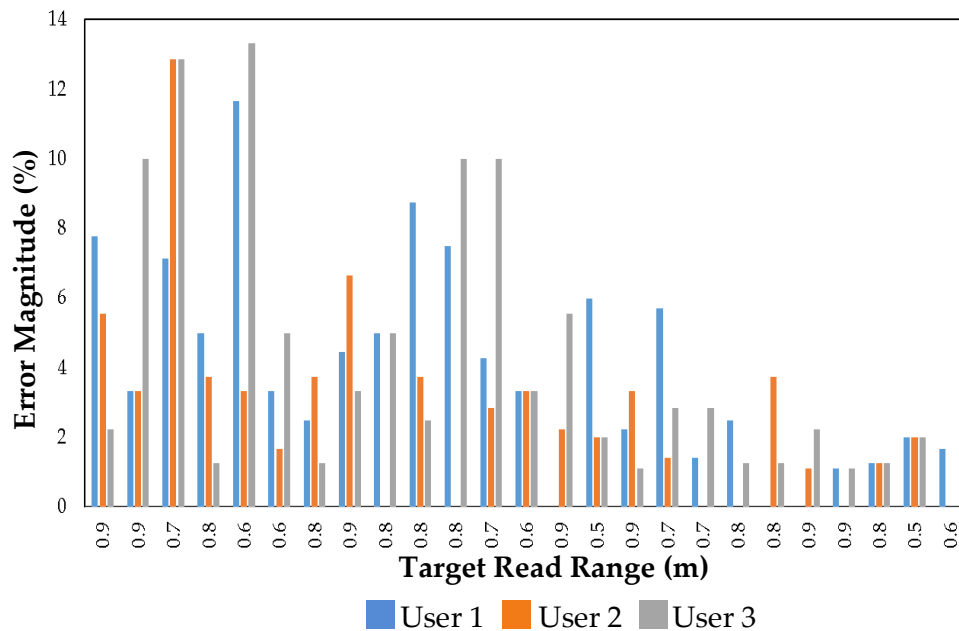
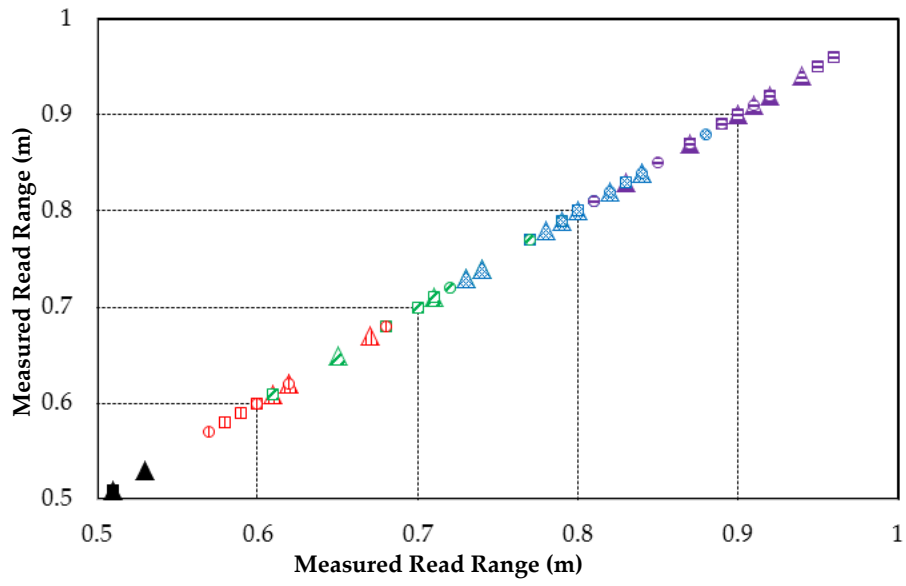


Figure 6.34: Error Magnitude comparison on user performances for 25 target hit performance.

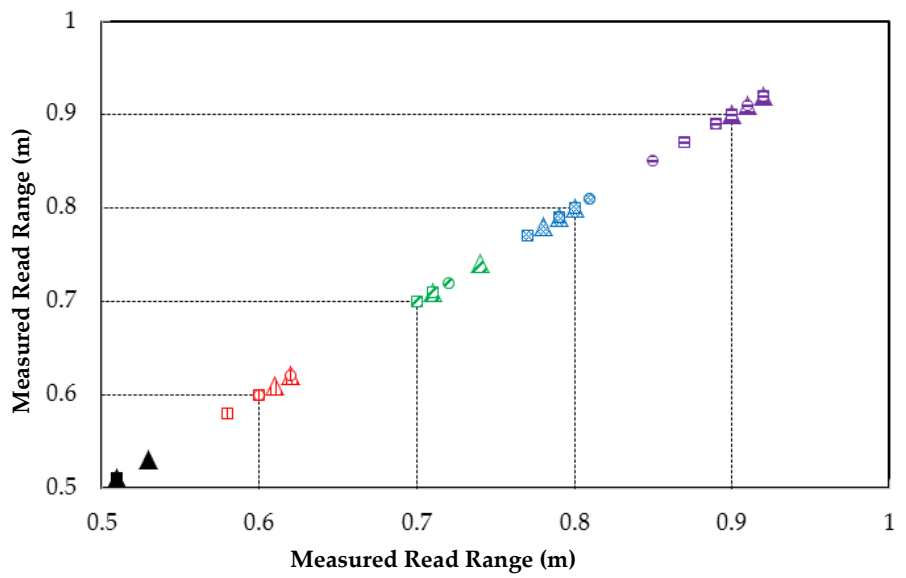
and no occurrences of target errors for any user.

When the users' performance is assessed using the data in Table 6.7(a) and (b), User 2 is the most accurate in terms of mean error and spread, where spread represents the range of minimum and maximum error, followed by User 1 for the entire 25 attempts. User 2 remains most accurate for the final 13 tries, but User 3 becomes the second most accurate, demonstrating they have benefitted more from practice than User 1.

To appreciate the range of accuracy for each target distance, the data for every attempt by all users are presented in confusion matrices relating the probability of hitting a target to the intended aim. Table 6.8 shows the confusion matrices for the 3 individuals and a final average respectively. A target was deemed to be hit if the user landed within the mid-points between each target. Each user attempted to hit each of the 5 targets in a sequence decreasing from 0.9m to 0.5m. They repeated this 7 times. It is clear from the confusion matrix relating



(a)



(b)

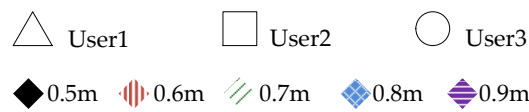


Figure 6.35: Target accuracies for 3 users over a random sequence of (a) entire 25 attempts (b) last 13 attempts.

Table 6.7: Comparison of entire measurements to last 13 measurements.

(a) Entire 25 Measurement Data.

Target (m)	USER 1		USER 2		USER 3	
	Mean Error %	Error Spread %	Mean Error %	Error Spread %	Mean Error %	Error Spread %
0.5	4	4	2	0	2	0
0.6	5	10	-2	3.3	2.9	18.3
0.7	1	12.9	-3.6	14.3	7.1	10
0.8	-0.9	13.8	-1	7.5	2.7	11.3
0.9	-0.5	12.2	1	10	-2	12.2

(b) Measurement data corresponding to measurements 13 to 25.

Target (m)	USER 1		USER 2		USER 3	
	Mean Error %	Error Spread %	Mean Error %	Error Spread %	Mean Error %	Error Spread %
0.5	4	4	2	0	2	0
0.6	2.5	1.7	-1.7	3.2	1.7	3.5
0.7	3.6	4.3	0.7	1.4	2.9	0
0.8	-1.3	2.5	-1.4	3.75	0.4	2.5
0.9	0.8	2.2	-0.6	5.6	-0.8	7.8

to the overall average, that when all seven trials are included, the total errors at each target are 20% or more for all targets except 0.9m.

In order to appreciate the improvement in target accuracy over the course of the training session Table 6.9 shows the confusion matrix for the overall average of just the final 3 sequences for each user. A marked reduction in the error spread is noted, meaning that, neglecting an 11% error at 0.5m, all individual targets are resolved without error after a short training experience.

To prevent the users obtaining deceptively accurate results because they were presented with sequentially reducing target distances, the final part of the training required them to hit the 0.5m to 0.9m target distances in a defined, but random, sequence of twenty five. As before, the users had two seconds to find each target.



Tables 6.10 and 6.11 show the mean error and spread for each user attempting each target, for all 25, and just the final 13 attempts, respectively. All error means and ranges reduce significantly for the final 13 tries with the exception of the 0.5m target which only occurred in the final half of the sequence. For the final 13 attempts the 0.5m target has the highest mean error for Users 1 and 2, while the 0.7m target is most difficult for User 3.

When the users' performance is assessed for the data in Tables 4 and 5 for the entire 25 attempts, User 2 is the most accurate in terms of mean error and spread, followed by User 1. User 2 remains most accurate for the final 13 tries, but User 3 becomes the second most accurate, demonstrating they have benefitted more from practice than User 1.

Table 6.8: Confusion matrices of 3 users and average hit rates for an ordered entire 7 sequence of targets.

		Measured Hit				
		0.9m	0.8m	0.7m	0.6m	0.5m
Target	0.9m	1.00				
	0.8m		1.00			
	0.7m		0.14	0.57	0.29	
	0.6m				1.00	
	0.5m				0.14	0.86

User 1

		Measured Hit				
		0.9m	0.8m	0.7m	0.6m	0.5m
Target	0.9m	1.00				
	0.8m		0.71	0.29		
	0.7m			0.86	0.14	
	0.6m			0.29	0.71	
	0.5m					1.00

User 2

Using the data from the random sequence of 25, the measured hit rate for each target is presented in Table 6 as a confusion matrix for each user and for the overall average. It can be seen that the accuracy for all targets is high, with User

		Measured Hit				
		0.9m	0.8m	0.7m	0.6m	0.5m
Target	0.9m	1.00				
	0.8m	0.43	0.57			
	0.7m		0.29	0.71		
	0.6m			0.14	0.72	0.14
	0.5m				0.57	0.43

User 3

		Measured Hit				
		0.9m	0.8m	0.7m	0.6m	0.5m
Target	0.9m	1.00				
	0.8m	0.14	0.76	0.10		
	0.7m		0.14	0.71	0.14	
	0.6m			0.14	0.81	0.05
	0.5m				0.24	0.76

Average

Table 6.9: Confusion matrices of 3 users and average hit rates for an ordered sequence of targets from 5 to 7.

		Measured Hit				
		0.9m	0.8m	0.7m	0.6m	0.5m
Target	0.9m	1.00				
	0.8m		1.00			
	0.7m			1.00		
	0.6m				1.00	
	0.5m				0.11	0.89

Average

3 alone experiencing just 50% success for only one target (0.7m). Excepting this, all users manage at least 75% hit rate for all targets. Considering the average values, all targets except 0.7m experience more than 80% hit rate when their initial attempts are included. Table 6 shows the confusion matrix considering only the second half of the 25 target sequence, i.e. when the users had become accustomed to the interface. In this case, zero error is observed for all targets.

Table 6.10: Confusion matrices of 3 users and average hit rates of entire 25 random targets.

		Measured Hit				
		0.9m	0.8m	0.7m	0.6m	0.5m
Target	0.9m	0.86	0.14			
	0.8m		0.75	0.25		
	0.7m			1.00		
	0.6m			0.25	0.75	
	0.5m					1.00

User 1

		Measured Hit				
		0.9m	0.8m	0.7m	0.6m	0.5m
Target	0.9m	1.00				
	0.8m		1.00			
	0.7m			0.75	0.25	
	0.6m				1.00	
	0.5m					1.00

User 2

		Measured Hit				
		0.9m	0.8m	0.7m	0.6m	0.5m
Target	0.9m	0.86	0.14			
	0.8m	0.13	0.87			
	0.7m		0.50	0.50		
	0.6m			0.25	0.75	
	0.5m					1.00

User 3

		Measured Hit				
		0.9m	0.8m	0.7m	0.6m	0.5m
Target	0.9m	0.91	0.09			
	0.8m	0.04	0.87	0.08		
	0.7m		0.17	0.75	0.08	
	0.6m			0.17	0.83	
	0.5m					1.00

Average

Table 6.11: Confusion matrices of 3 users and average hit rates of random targets from 13 to 25.

		Measured Hit				
		0.9m	0.8m	0.7m	0.6m	0.5m
Target	0.9m	1.00				
	0.8m		1.00			
	0.7m			1.00		
	0.6m				1.00	
	0.5m					1.00

Average

## 6.4 Conclusion and Future Work

An innovative wireless passive tongue switching assistive technology using RFID tags has been presented with an application for wheel chair control for patients with severe movement impairment. The preliminary simulation and measurement results indicate that multi-chip RFID tags for mouth mounting could form a 4 point joystick controlled by the tongue. When mounted on the hard palate, the tag offered read ranges of more than 1m, which is appropriate for a system where the read antenna would be mounted on the wheelchair about 30 cm in front of the operator. The tag would ultimately be integrated into a dental plate to provide a straight forward and hygienic method of mounting. Reader power consistent with licensed RFID systems would be supplied from the chair and the significant processing capability of the chair navigation system would be available to calibrate and train the system for the patient.

A threshold exists between the on-and off-states for a tongue-tag separation of about 4 mm. Therefore, in use, the tongue touching the tag would represent a definite off condition.

Simulation using a more detailed mouth model improved the correspondence with measurement where the tag has been assessed on three different users.

Following practice, a significant improvement in accuracy was observed for all users. Future development resulting in much smaller sensors could have application in tongue position monitoring in speech therapy where current technologies require a loom of many wires to pass out of the patient's mouth during monitoring. The removal of these wires would create a much more natural condition for speech.

## References

- [1] M. Gillham, B. McElroy, G. Howells, S. Kelly, S. Spurgeon, and M. Pepper, "Weightless neural system employing simple sensor data for efficient real-time round-corner, junction and doorway detection for autonomous system path planning in smart robotic assisted healthcare wheelchairs," in *Emerging Security Technologies (EST), 2012 Third International Conference on*, Sept 2012, pp. 161–164.
- [2] J. Douglas, B. Reeson, and M. Ryan, "Computer microtechnology for a severely disabled preschool child." *Child: care, health and development*, vol. 14, no. 2, pp. 93–104, 1988.
- [3] R. Bates, "A computer input device selection methodology for users with high-level spinal cord," *Proc. of the 1st Cambridge Workshop on Universal Access and Assistive Technology (CWUAAT)*, pp. 1–4, 2002.
- [4] T. Rofer, C. Mandel, and T. Laue, "Controlling an automated wheelchair via joystick/head-joystick supported by smart driving assistance," in *Rehabilitation Robotics, 2009. ICORR 2009. IEEE International Conference on*, June 2009, pp. 743–748.
- [5] D. Evans, R. Drew, and P. Blenkhorn, "Controlling mouse pointer position using an infrared head-operated joystick," *Rehabilitation Engineering, IEEE Transactions on*, vol. 8, no. 1, pp. 107–117, Mar 2000.
- [6] S. Guo, R. Cooper, M. Boninger, A. Kwarciak, and B. Ammer, "Development of power wheelchair chin-operated force-sensing joystick," in *Engineering in Medicine and Biology, 2002. 24th Annual Conference and the Annual Fall Meeting of the Biomedical Engineering Society EMBS/BMES Conference, 2002. Proceedings of the Second Joint*, vol. 3, Oct 2002, pp. 2373–2374.

- [7] LC Technologies, Inc. , “Eyegaze,” 2014, Accessed: 15.06.2014. [Online]. Available: <http://www.eyegaze.com/>
- [8] O. Rakibet, D. Oyeka, and J. Batchelor, “Passive RFID switches for assistive technologies,” in *Antennas and Propagation (EuCAP), 2013 7th European Conference on*, April 2013, pp. 1917–1920.
- [9] O. Rakibet, J. Batchelor, and S. Kelly, “Passive stretchable RFID tag,” in *Antennas and Propagation Conference (LAPC), 2012 Loughborough*, Nov 2012, pp. 1–4.
- [10] M. Ziai and J. Batchelor, “A prototype passive UHF RFID transfer tattoo tag,” in *Antennas and Propagation (EUCAP), Proceedings of the 5th European Conference on*, April 2011, pp. 3811–3814.
- [11] —, “Temporary On-Skin Passive UHF RFID Transfer Tag,” *Antennas and Propagation, IEEE Transactions on*, vol. 59, no. 10, pp. 3565–3571, Oct 2011.
- [12] C. Occhiuzzi, S. Cippitelli, and G. Marrocco, “Modeling, Design and Experimentation of Wearable RFID Sensor Tag,” *Antennas and Propagation, IEEE Transactions on*, vol. 58, no. 8, pp. 2490–2498, Aug 2010.
- [13] G. Marrocco, “The art of UHF RFID antenna design: Impedance-matching and size-reduction techniques,” *Antennas and Propagation Magazine, IEEE*, vol. 50, no. 1, pp. 66–79, Feb 2008.
- [14] 3D CAD Browser , “Teeth, Roots and Gums,” 2014, Accessed: 24.03.2014. [Online]. Available: <http://www.3dcadbrowser.com/>
- [15] Italian National Research Council , “Dielectric Properties of Body Tissues,” 2012, Accessed: 01.02.2012. [Online]. Available: <http://niremf.ifac.cnr.it/tissprop/htmlclie/htmlclie.php>
- [16] D. M. Dobkin, “Chapter 3 - Radio Basics for UHF RFID,” in *The RF in RFID*, D. M. Dobkin, Ed. Burlington: Newnes, 2008, pp. 51 – 101.

# CHAPTER 7

## SUMMARY, KEY-POINTS AND FUTURE WORK

\* \* \*

Extensive research on the body-worn applications has opened a new perspective for tracking and sensing applications along with a comfortable fit to the body features in the last decade. Many challenges have arisen in antenna impedance matching due to close body vicinity. Thus, this issue has brought more interest in the body tissue and dielectric material electrical properties investigation for simulating and estimating the proposed application behaviours very accurately to achieve a perfect functionality.

The research presented in this thesis includes an investigation on the application and assessment of high permittivity  $\text{TiO}_2$  powder to body worn electromagnetic structures for communication. A comprehensive study has been



undertaken on passive UHF RFID sensor tags for assisted living applications. The design and function of two skin mounted human computer interfacing (HCI) tags have been presented, one acting as a strain sensor and the other as a tongue proximity switch.

This chapter provides a summary of the work and concludes the thesis. Recommendations for enhancements are discussed in the final section.

Chapter 2 summarises the the theory behind the antenna design and communications is reviewed and the design philosophy which is common for all antennas and RFID tags based on an understanding of electromagnetic operation in respect to RFID technology covering Friis Equations have been described.

Chapter 3 covers the general RFID tag design and prototyping to be used as sensors. The performance indicating factors, methodology behind the sensing and derivation of external agents in order to extract the amount of change on the tag performance which is directly related to transponder chip impedance matching have been developed and outlined. Impedance matching methods, transponder chip types and environmental effects on the tag performance and the measurement set up have also been covered along with the sensor tag simulations in CST Microwave Studio including body tissue and stretch effect modelling and the optimisation techniques for an increased simulation accuracy.

In Chapter 4, Mushroom-like EBG structures have been investigated along with the individual components such as patch length, width, patch separation and also their effects on the capacitance and inductance which determine the resonant frequency. The effect of dielectric constant is investigated on the capacitance, therefore on the thickness of an EBG structure. Dielectric constant of TiO<sub>2</sub> powder is quoted as 95 when compressed and turned into a solid block. The effect of TiO<sub>2</sub> on thickness reduction in the EBG structures simulated at 400

MHz to be used in the bands bands those used by the police and emergency services.

The theory and measurement set up of the waveguide method to analyse electrical characteristics have also been presented in this chapter. In order to check the reliability of the achieved results, preliminary measurements were taken from PTFE and wax where their electrical properties, of dielectric constant and loss tangent, are well known and the expected results were achieved. The dielectric constant of stretchable and flexible BaTiO<sub>3</sub> loaded PDMS structures have also been measured.

A special compressing process was necessary to produce solid TiO<sub>2</sub> samples by applying tonnes of pressure to it, the sample were not measured under its optimum state to reflect the expected dielectric properties. Therefore, the key points for this chapter can be listed as:

- Making solid blocks by using powder state materials may result in losing its electrical properties, where the air particles accommodate in the substrate, if the enough amount of pressure is not applied.
- Sintering may be necessary after making a solid block by using a powder material.
- Using waveguide method to measure high permittivity substrates, the length of the substrate which is measured must be selected carefully to prevent phase wrap issues.
- Measurement results have indicated that BaTiO<sub>3</sub> loaded PDMS structures could be applied to tag sensors.
- As a future remark, designing EBG structures with the stretchable and flexible substrate BaTiO<sub>3</sub> loaded PDMS structures can be attached to body with a better conformal fit. As the electrical properties of BaTiO<sub>3</sub> loaded

PDMS substrates investigated, that simulating and prototyping the EBG structure with this substrate will bring an opportunity to observe the effect of stretch and flex on the EBG resonant frequency in the future.

As a part of SYSIASS project, in order to supply an input mechanism to control and drive a wheelchair by detecting skin stretch on the neck or on top of the eyebrows an strain gauge RFID sensor was presented in Chapter 5.

A single slot antenna operating at 2.45 GHz has been modelled on a silicone substrate and the  $x$  and  $y$  axis stretch have also been simulated to observe the stretch effect on the resonant frequency and the matching quality.

In order to distinguish the stretch direction, two slot structure has been modelled where the slots have been placed perpendicular to each other. The  $x$  axis ,  $y$  axis and the simultaneous  $x$  and  $y$  axis stretch effects have been simulated along with the resonant frequency and matching quality behaviours.

After the slot antenna simulations, the single slot antenna design converted into an RFID tag. The UHF RFID tag was simulated on a BaTiO<sub>3</sub> loaded PDMS substrate which is a stretchable and flexible substrate and the effect of BaTiO<sub>3</sub> loading on the dielectric constant was investigated. The RFID strain gauge sensor structure was simulated on a rectangular arm model assigned with the body tissue dielectric properties as the strain gauge sensor was proposed for skin attachment purposes.

After the simulation and the fabrication of the strain gauge tag, the stretching measurements took place by using a controlled jig. The key points for this chapter can be listed as:

- Stretchable conductive fabric used as a conductor antenna successfully.
- BaTiO<sub>3</sub> loaded PDMS, a nonhazardous and harmless to skin substrate, used as an epidermal stretchable substrate.

- The adhesion of Lycra and PDMS structure successfully achieved without using an additional adhesive. This has been done by finding the best time to place the fabric on top of the PDMS sample at its curing stage.
- Use of stretchable conductive epoxy glue to attach the RFID transponder chip to the RFID sensor tag did not limit the stretching amount of the RDID sensor.
- Using laser cutter to cut the Lycra fabric where it was impossible to etch it chemically.
- The simulated arm model matched the measurement results well. Therefore, the arm model validated by the measurements.
- The measured electrical properties of BaTiO<sub>3</sub> loaded PDMS samples with the waveguide method matched the simulated results.
- The measurements on jig have successfully shown the effect of stretch on the tag performance.
- As a future remark, the effect of locating an additional perpendicular RFID slot to the current design for a better precision in detecting strain direction could be investigated. In addition to this, for more accurate skin stretch effect investigation, the structure could be attached to the skin and the strain effect on the performance indicating factors could be measured. Skin adhesion methods and the efficiency of the re-usability after detaching from the skin could also be investigated.

Tongue position detection in the mouth to be used for wheelchair or computer mouse control applications was presented as also a part of SYSIASS project. The mounted conformal tag on the hard palette of the mouth used to detect tongue position and demonstrated to act as a tongue controlled switch.

At the initial state transfer tattoo tag was used to observe the functionality of a tag in the mouth. As it was not designed to be placed into the mouth, the dimensions were too big for a conformal fit onto the hard palate. After making the tag smaller to eliminate the overlap with the teeth, the measurements were repeated. The preliminary results have indicated a promising results for detecting the tag proximity in the mouth.

For a perfect fit onto the hard palate, the tag has been redesigned, tag corners were rounded while keeping the slot dimensions same. After designing the tag, it was simulated with a homogenous mouth model excluding teeth. The measurements and simulations have shown an agreement up to an extent. Therefore, a detailed mouth was modelled to accomplish more accurate simulations.

Tongue-tag separation of about 4 mm resulted in a threshold between the *on*-and *off*-states and therefore, in use, touching the tag with the tongue would represent a definite *off* condition.

After designing, simulating the tag with the accurate mouth model and measuring the actual performance of the tag in the mouth successfully, the tag performance was tested by 3 different users and the tag performance was estimated.

In order to estimate the necessary training time and scheme, a number of tasks were carried out. Initial user performances were compared with the final performances on using the system accurately and target finding. The key points for this chapter can be listed as:

- The functionality of an RFID tag in the mouth is tested first time ever in this study.
- Simple mouth model created for the conformal RFID tag sensor simulations.

- Accurate mouth model with precise mouth dimensions, including teeth, gums and tongue tissues are created for the conformal RFID tag sensor simulations.
- Accurate mouth model simulations have shown a good agreement with the measurements.
- The RFID sensor tag tested on 3 different users to test its functionality in different mouths and the measurement results have indicated a success.
- Successful training process for estimating the efficient training time to use the tags.
- As future remarks,
  - In order to add more control opportunities to the system, tag RFID sensors could be designed with multiple inputs. To make the tag hygienic and simple to apply, it may be ultimately integrated into a conventional dental plate.
  - Further reduction of the sensor size could allow for a matrix to be applied to the hard palette for high resolution sensing of tongue position. This could be of benefit for speech therapy as current monitoring systems require a loom of wires to be passed through the patient's mouth and disrupt the normal conditions of speech. A wireless solution based on the passive technology demonstrated here would overcome this issue.